Dispersion and Mixing of Plumes in Wall-Bounded and Isotropic Turbulent Flows

by

Shahin NasseriOskouie

A thesis submitted to
The Faculty of Graduate Studies of
The University of Manitoba
in partial fulfillment of the requirements
of the degree of

Doctor of Philosophy

Department of Mechanical Engineering
The University of Manitoba
Winnipeg, Manitoba, Canada
April 2016

Abstract

The dispersion and mixing of passive scalars released from two concentrated sources into open-channel and homogeneous isotropic turbulent flows are studied using direct numerical simulation (DNS). The simulations are conducted using two fully-parallelized in-house codes developed using the FORTRAN 90/95 programming language. A comparative study has been conducted to investigate the effects of the source separation distance, Reynolds number, relative length scales of the plume and turbulent flow, and source elevation on the dispersion and mixing of two plumes. For both flow configurations, four distinct stages in the downwind development of the cross correlation between the fluctuating concentration fields have been identified which feature zero, destructive and constructive interferences and a complete mixing state. Differences between the exceedance probability of concentrations for the single and total plumes are highlighted and analyzed, and the effects of destructive and constructive interference on the exceedance probabilities for the total plume are used to explain these differences. It is found that the relationship between the third- and fourth-order concentration moments and the second-order concentration moment can be well predicted using a clipped-gamma model. This leads to an interesting conclusion that all the higher-order (third-order and above) moments of the total concentration can be inferred from a knowledge of only the first- and second-order concentration moments of each single plume and of the cross correlation coefficient. From a spectral analysis, it is observed that there exists a range of ‘leading scales’ at which the rate of turbulent mixing of the two plumes becomes the most efficient and the coherency spectrum of the plumes approaches the asymptotic value of unity quicker than at any other scales.

Contents

Abstract ii
Table of Contents vi
List of Figures vii
List of Tables xvii
Acknowledgments xviii
Nomenclature xix

1 Introduction 1

1.1 Motivation 1
1.2 Previous Work 2
  1.2.1 Single plume dispersion 2
  1.2.2 Multiple plume dispersion and mixing 4
1.3 Objectives 8
1.4 Outline 10

2 Numerical Method 11

2.1 Governing Equations 11
2.2 Solution Algorithm and Discretization Scheme 12
  2.2.1 Open-channel Flow 12
  2.2.2 Homogeneous Isotropic Turbulent Flow 13
2.3 High-Performance Computing 13

3 Dispersion and Mixing of Ground-Level Plumes 15
3.1 Introduction 15
3.2 Problem Description 16
3.3 Result Analysis 17
  3.3.1 Velocity Statistics 17
  3.3.2 Mean Concentration 20
  3.3.3 Variance of Concentration Fluctuations 27
  3.3.4 Cross Correlation Coefficient 35
  3.3.5 Concentration Co-spectrum and Coherency Spectrum 41
3.4 Chapter Summary 46

4 Effect of Source Elevation on the Dispersion and Mixing of Plumes 49
4.1 Introduction 49
4.2 Problem Description 50
4.3 Results and Discussion 51
  4.3.1 Mean Concentration Field 51
    4.3.1.1 Mean concentration of a single plume 51
    4.3.1.2 Mean concentration of the total plume 57
  4.3.2 Concentration Fluctuations 58
    4.3.2.1 Single plume fluctuations 59
    4.3.2.2 Total plume fluctuations 61
  4.3.3 Correlation Functions 65
  4.3.4 Concentration Co-spectrum and Coherency Spectrum 71
  4.3.5 Concentration PDF and EDF 73
    4.3.5.1 Concentration PDF of a single plume 73
    4.3.5.2 Interference effect on concentration EDF of the total plume 75
  4.3.6 Higher-Order Concentration Moments 80

4.4 Chapter Summary 83

5 Dispersion and Mixing of Plumes in Isotropic Turbulence 86

5.1 Introduction 86
5.2 Problem Description 87
5.3 Result Analysis 88
  5.3.1 Velocity Statistics 89
  5.3.2 Mean Concentration 89
    5.3.2.1 Single Source 90
    5.3.2.2 Two Sources 91
  5.3.3 Variance of Concentration Fluctuations 92
    5.3.3.1 Single Source 92
    5.3.3.2 Two Sources 93
  5.3.4 Cross Correlation Coefficient 95
  5.3.5 Concentration Co-spectrum and Coherency Spectrum 98
  5.3.6 Concentration PDF and EDF 100
    5.3.6.1 Concentration PDF of the single plume 101
    5.3.6.2 Cross correlation effect on concentration EDF of the total plume 102
  5.3.7 Higher-Order Concentration Moments 106
5.4 Chapter Summary 108

6 Conclusions and Future Work 110

6.1 Conclusions 110
  6.1.1 Computer Codes 110
  6.1.2 Testing Parameters and Numerical Simulations 112
  6.1.3 Single Plume Dispersion Characteristics 113
  6.1.4 Dual Plume Dispersion and Mixing 114
6.2 Future Work 117

A Discretization Scheme used in Open-Channel Code 119

A.1 Continuity and Momentum Equations 119

A.1.1 Compact Form 120

A.1.2 Expanded Form 122

A.1.3 Advection-Diffusion Equation 127

A.1.4 Compact Form 129

A.1.5 Expanded Form 129

A.2 Grid Resolution 132

B Discretization Scheme Used in Isotropic Turbulence Code 134

B.1 Continuity and Momentum Equations 134

B.2 Advection-Diffusion Equation 137

B.3 Grid Resolution 137

Bibliography 144

List of Figures

3.1 Schematic of the computational domain of the open-channel flow. Two point sources A and B are separated in the spanwise direction by a distance d and are each positioned at a distance y_s above the lower (solid) channel wall. 17

3.2 Comparison of present DNS predictions of the velocity statistics of an open-channel flow against reported DNS data of Handler et al. (1999) for an open-channel flow and those of Moser et al. (1999) for a plane-channel flow. All flow statistics are non-dimensionalized using the wall friction velocity u_τ. 19

3.3 The relative width of the instantaneous plume at different regimes of plume development. 21

3.4 Spanwise velocity fluctuations spectra and pre-multiplied spanwise velocity fluctuations spectra at $y_s^+ = 5$. 23

3.5 Schematic of the plume scales. 25

3.6 Streamwise variation of the non-dimensionalized lateral mean plume dispersion (σ_z/δ) and meandering ratio $(M = \sigma_c^2/\sigma_r^2)$ at source height. The dashed and dash-dot-dotted vertical lines show the locations where the width of the instantaneous plume first reaches the size of the most energetic turbulent eddies for $Re_\tau = 180$ and 395, respectively. 26

3.7 Lateral profiles of the mean concentration for the source at A (■), for the source at B (○), and for both sources (solid line) at three streamwise locations. 28

3.8 Lateral profiles of the total mean concentration for different y^+ values at $x/\delta = 6$. The arrow points to the increasing direction of y^+. 29

3.9 Lateral profiles of the variance of concentration fluctuations at $x/\delta = 4$. 30

3.10 Lateral profiles of the total mean concentration C_T (■) and the variance of concentration fluctuations of the total plume $\overline{c_T'^2}$ (○). Straight vertical dashed and dash-dot-dotted lines indicate the locations of the local maxima of the absolute total mean concentration gradient and the locations of the local extrema of the mean concentration profile, respectively. Symbol ϕ represents either C_T or $\overline{c_T'^2}$. 31

3.11 Lateral profiles of the variance of concentration fluctuations for different y^+ values at $x/\delta = 6$. Recall again that the source is located at $y^+ = 5$. The arrow points to the increasing direction of y^+. 34

3.12 Streamwise variation of the cross correlation $\rho^{[1|1]}$ in the midplane along the spanwise direction between the plumes at source height. Cases 1 (□), 2 (○), 3 (△), 4 (◇), 5 (■), 6 (●), 7 (▲), and 8 (◆). 37

3.13 Lateral profiles of the cross correlation $\rho^{[1|1]}$ at source height. Cases 1 (□), 2 (○), 3 (△), 4 (◇), 5 (■), 6 (●), 7 (▲), and 8 (◆). 40

3.14 The pre-multiplied co-spectrum of two plumes for cases 1 and 5 obtained at the midpoint between the two plumes and at source height, for $x/\delta = 0.5$ (solid line), 1 (thin dashed line), 3 (dash-dotted line), 6 (dotted line) and 12 (thick dashed line). 43

3.15 The coherency spectrum $\rho_f^{[1|1]}$ of two plumes for cases 1 and 5 obtained at the midpoint between the two plumes and at source height, for $x/\delta = 0.5$ (thin solid line), 1 (dashed line), 3 (dash-dotted line), 6 (dotted line) and 12 (thick dashed line). The straight vertical dashed line shows the frequency corresponding to the Kolmogorov scale. The long dashed curve shows the pre-multiplied energy spectrum $f^* E_{w'w'}$ of velocity fluctuations in the spanwise direction. The pre-multiplied energy spectrum $f^* E_{w'w'}$ is used here for identifying the frequency corresponding to the most energetic eddies (through its peak location), and its magnitude has been re-scaled arbitrarily in order to fit in the figure panel. 44

4.1 Streamwise development of a single plume. (a) The lateral mean (or absolute) plume dispersion σ_z scaled by the boundary-layer height δ and (b) the ratio of the lateral relative plume dispersion σ_r to the mean plume dispersion σ_z (for the ground-level and elevated sources) as a function of the non-dimensional downstream distance x/δ. The beginning of the turbulent diffusive range for the elevated source is demarcated using the vertical dot-dash line. 53

4.2 (a) Spanwise velocity spectrum plotted against the spanwise wavenumber and (b) pre-multiplied spanwise velocity spectrum plotted against the spanwise wavelength at $y^+ = 40$ (height of the elevated source). The full width of the instantaneous plume ($2\Sigma_r$) at the beginning of the turbulent diffusive range for the elevated source is indicated by the dashed vertical line. 54

4.3 Streamwise variation of the vertical mean plume dispersion along the mean plume centerline for a ground-level and an elevated source. . . . 56

4.4 The vertical profiles of the mean concentration along the plume centerline for (a) a ground-level and (b) an elevated source at non-dimensionalized downwind fetches of $x/\delta = 1$ (solid line), 2 (dashed line), 4 (dotted line) and 6 (dash-dot line). 56

4.5 The lateral profiles of the total mean concentration for cases 1 (solid line); 2 (dashed line); 3 (dotted line); and, 4 (dash-dot line) at normalized downwind fetches of (a) $x/\delta = 1$, (b) 2, (c) 4, and (d) 6 for the ground-level sources. These profiles are obtained at the source height $y^+ = 5$. 58

4.6 The lateral profiles of the total mean concentration for cases 5 (solid line); 6 (dashed line); 7 (dotted line); and, 8 (dash-dot line) at normalized downwind fetches of (a) $x/\delta = 1$, (b) 2, (c) 4, and (d) 6 for the elevated sources. These profiles are obtained at the source height $y^+ = 40$. 59

4.7 Comparison of the lateral profiles of $\hat{c}$ for a single ground-level (solid line) and a single elevated (dashed line) plume at source height and at four downwind fetches of (a) $x/\delta = 1$, (b) 2, (c) 4, and (d) 6 from the source. The vertical solid and dashed lines demarcate the spanwise positions located at $\pm\sigma_z$ from the mean plume centerline for the ground-level and elevated source, respectively. 60

4.8 Lateral profiles of RMS concentration $\hat{c}_T$ of the total plume at source height corresponding to cases 1 (solid line), 2 (dashed line), 3 (dotted line) and 4 (dash-dot line) at four downwind fetches of (a) $x/\delta = 1$, (b) 2, (c) 4, and (d) 6 for two near ground-level sources. 62

4.9 Lateral profiles of RMS concentration $\hat{c}_T$ of the total plume at source height corresponding to cases 5 (solid line), 6 (dashed line), 7 (dotted line) and 8 (dash-dot line) at four downwind fetches of (a) $x/\delta = 1$, (b) 2, (c) 4, and (d) 6 for two elevated sources. 62

4.10 Lateral profiles of the total mean concentration C_T (solid line) and the total RMS concentration $\hat{c}_T$ (dashed line) at source height corresponding to case 1 (near ground-level sources separated by $d/\delta = 0.049$) at four downwind fetches of (a) $x/\delta = 1$, (b) 2, (c) 4, and (d) 6 from the two sources. Vertical solid lines indicate the locations of inflection points in the lateral profiles of the total mean concentration for case 1. 64

4.11 Lateral profiles of the total mean concentration C_T (solid line) and the total RMS concentration $\hat{c}_T$ (dashed line) at source height corresponding to case 3 (near ground-level sources separated by $d/\delta = 0.279$) at four downwind fetches of (a) $x/\delta = 1$, (b) 2, (c) 4, and (d) 6 from the two sources. Vertical solid lines indicate the locations of inflection points in the lateral profiles of the total mean concentration for case 3. 64

4.12 Lateral profiles of the total mean concentration C_T (solid line) and the total RMS concentration $\hat{c}_T$ (dashed line) at source height corresponding to case 5 (elevated sources separated by $d/\delta = 0.049$) at four downwind fetches of (a) $x/\delta = 1$, (b) 2, (c) 4, and (d) 6 from the two sources. Vertical solid lines indicate the locations of inflection points in the lateral profiles of the total mean concentration for case 5. The downward pointing arrows delineate the spanwise locations of the two sources. 66

4.13 Lateral profiles of the total mean concentration C_T (solid line) and the total RMS concentration $\hat{c}_T$ (dashed line) at source height corresponding to case 7 (elevated sources separated by $d/\delta = 0.279$) at four downwind fetches of (a) $x/\delta = 1$, (b) 2, (c) 4, and (d) 6 from the two sources. Vertical solid lines indicate the locations of inflection points in the lateral profiles of the total mean concentration for case 7. The downward pointing arrows delineate the spanwise locations of the two sources. 66

4.14 Streamwise variation of $\rho^{[1|1]}$ at the midpoint in the spanwise direction between the two plumes at source height. Cases 1 (●), 2 (■), 3 (▼), 4 (♦), 5 (○), 6 (□), 7 (▽), and 8 (◇). 67

4.15 The streamwise evolution of the mean plume width $2\Sigma_z$ (solid symbols) and the relative plume width $2\Sigma_r$ (hollow symbols) for a single ground-level source non-dimensionalized by the source separation distance (d) for cases 1 (● and ○), 2 (■ and □), 3 (▼ and ▽) and 4 (♦ and ◇). The horizontal dotted lines used for dividing the four stages of dual plume interference are conceptual. 68

4.16 The streamwise evolution of the mean plume width $2\Sigma_z$ (solid symbols) and the relative plume width $2\Sigma_r$ (hollow symbols) for a single elevated source non-dimensionalized by the source separation distance (d) for cases 5 (● and ○), 6 (■ and □), 7 (▼ and ▽) and 8 (♦ and ◇). The horizontal dotted lines used for dividing the four stages of dual plume interference are conceptual. 69

4.17 Lateral profiles of $\rho^{[1|1]}$ at source height at four downwind fetches of (a) $x/\delta = 1$, (b) 2, (c) 4, and (d) 6 from the two sources. Ground-level source releases are cases 1 (●), 2 (■), 3 (▼), 4 (♦). Elevated source releases are cases 5 (○), 6 (□), 7 (▽), and 8 (◇). 70

4.18 The pre-multiplied co-spectrum and coherency spectrum of dual plumes for case 5 obtained at the midpoint between the two plumes and at source height, for $x/\delta = 0.5$ (solid line), 1 (thin dashed line), 3 (dash-dotted line), 6 (dotted line) and 12 (thick dashed line). The straight vertical dashed line shows the frequency corresponding to the Kolmogorov scale. Ranges 1 and 2 indicate the leading scales in the turbulent convective and the turbulent diffusive regimes, respectively. . . 72

4.19 Concentration PDF at source height along the mean plume centerline for a single ground-level (□) or elevated (○) source at four downwind fetches of (a) $x/\delta = 0.5$, (b) 1, (c) 3, and (d) 6 from the source. The dashed line shows the best Gaussian fit to the concentration PDF for the ground-level source. 74

4.20 Concentration PDF at source height for a single ground-level (□) or elevated (○) source at the downwind fetch of $x/\delta = 1$ at crosswind locations from the mean-plume centerline of (a) $(z - z_s)/\sigma_z = 0$, (b) 0.8, (c) 1.9 and (d) 3.7. 75

4.21 Concentration EDF of the total plume (solid line) and a single plume (dashed line) for case 1 in the midspan between the plumes at source height at four downwind fetches of (a) $x/\delta = 0.5$, (b) 1, (c) 3, and (d) 6 from the source(s). 77

4.22 RF for cases 1 (○), 2 (□), 5 (▽) and 6 (◇) as a function of concentration level at the midpoint between the two plumes at source height and at four downwind fetches of (a) $x/\delta = 0.5$, (b) 1, (c) 3, and (d) 6 from the sources. 78

4.23 Scatterplots of RF against $\rho^{[1|1]}$ obtained at various downwind locations at the midpoint between the two plumes at source height. 79

4.24 Scatterplots of the non-dimensionalized (a) third-order concentration moment and (b) fourth-order concentration moment, plotted against the non-dimensionalized second-order concentration moment for a large number of locations in the total plume. The prediction of the relationship between these moments provided by the clipped-gamma distribution model (solid line) is superimposed on the scatterplots. 83

5.1 (a) Schematic of the computational domain and (b) a snapshot of the instantaneous concentration field when both sources are active for case 4 at $z = \pi$. The two horizontal line sources positioned at A and B are separated in the y direction by a distance d. 88
5.2 Velocity energy spectra from DNS. 89
5.3 Streamwise development of the mean plume dispersion σ_a, the dispersion of the center of instantaneous plume σ_c, the relative plume dispersion σ_r and the meander ratio ($M = \sigma_c^2/\sigma_r^2$). Here, ϕ represent σ_a, σ_r or σ_c. 91
5.4 Profiles of the total mean concentration at four different downwind locations. Cases 1 (■), 2 (□), 3 (●), 4 (○), and 5 (▲). The arrow points towards increasing values of d. 93
5.5 Concentration variance profile of a single plume at four downwind locations from the source. 95
5.6 Profiles of the concentration variance at four downstream locations for the two source configuration. The arrow points in the direction of increasing downwind location x/l. 95
5.7 Streamwise variation of the cross correlation $\rho^{[1|1]}$ at the midpoint ($y = 0$) between the two sources. Cases 1 (■), 2 (□), 3 (●), 4 (○), and 5 (▲). 96
5.8 Profiles of the cross correlation in the y-direction. Cases 1 (■), 2 (□), 3 (●), 4 (○), and 5 (▲). The arrow points in the direction of increasing values of d. 97
5.9 The pre-multiplied co-spectrum of the concentration of the two plumes for (a) case 1 and (b) case 5 obtained at the midpoint location between the two sources ($y = 0$), for $x/l = 0.15$ (solid line), 0.5 (dashed line), 2 (dash-dotted line), 4 (dotted line) and 5 (dash-dot-dotted line). . . 99

5.10 The coherency spectrum $\rho_{k_z}^{[1|1]}$ of the concentration of the two plumes for (a) case 1 and (b) case 5 obtained at the midpoint between the two sources, for $x/l = 0.15$ (solid line), 0.5 (dashed line), 2 (dash-dotted line), 4 (dotted line) and 5 (dash-dot-dotted line). 100

5.11 Concentration PDF along the mean plume centerline at the normalized downwind fetches from the source for $x/l = 0.5$ (■), 1 (□), 2 (●), 3 (○) and 5 (▲). 102

5.12 Concentration PDF at the downwind fetch of $x/l = 1$ at four vertical locations from the mean plume centerline for $(y - y_s/l) = 0$ (■), 0.06 (□), 0.1 (●) and 0.14 (○). 103

5.13 Concentration EDF of the total plume (solid line) and a single plume (dashed line) for case 5 at the midpoint ($y = 0$) between the two sources at various downwind distances. 104

5.14 RF for cases 1 (■), 2 (□), 3 (●), 4 (○), and 5 (▲) as a function of the non-dimensionalized concentration level χ/C. These results were obtained at $y = 0$ (which for the two source release corresponds to the midpoint between these sources). 105

5.15 Scatterplots of RF against $\rho^{[1|1]}$ obtained at various downstream locations at the midpoint between the two sources. 106

5.16 Scatterplots of the normalized third- and fourth-order concentration moments plotted against the normalized second-order concentration moment for a large number of locations in the plume. The prediction of the relationship between these moments provided by the clipped-gamma distribution model (solid line) is superimposed on the scatterplot. 107

A.1 Schematic of a typical computational cell, its node, faces, indices and neighbors in 2-D and 3-D configurations for the base grid. Note that in a staggered grid arrangement, the grids for storing velocity components (u, v and w) are half-cell shifted in x, y and z directions, respectively. 121

List of Tables

3.1 Summary of test cases. 17

4.1 Summary of test cases. The near ground-level source (GLS) is located at $y_s^+ = 5$ and the elevated source (ES) is located at $y_s^+ = 40$. 50

5.1 Summary of test cases. 88

A.1 Values of the α coefficients for different flow directions 130

A.2 The ratio of gradients for different flow directions and cell faces . . . 131

A.3 Summary of grid resolutions. Nx, Ny and Nz represent the number of grid nodes in the x-, y-, and z-directions, respectively. Δy^+_{min} and Δy^+_{max} are the minimum and maximum grid resolutions in the wall-normal direction. 133

B.1 Key input parameters and output quantities from DNS of homogeneous isotropic turbulence. 138

Acknowledgments

I am using this opportunity to express my deepest appreciation to my advisors Dr. Bing-Chen Wang and Dr. Eugene Yee for the time they dedicated to teach and help me grow as a researcher. I would also like to thank my committee members, Professor David Kuhn, Professor Vladimir Okhmatovski for serving as my committee members.

I thank my friends and fellows in the research group of Professor Wang for the stimulating discussions and for the nice and friendly time I have had during my Ph.D. program.

Last but not the least, I would like to thank my parents, Massoud N. Oskouie and Shaahin Mahooti, for their unconditional love and support.

Nomenclature

English Symbols:

c	instantaneous concentration
C	mean concentration
$Co_{c'_A c'_B}$	co-spectrum of concentration fluctuations
d	source separation distance
$E_{c'c'}$	power spectrum of concentration fluctuations
$E_{w'w'}$	power spectrum of spanwise velocity fluctuations
f	probability density function
f_s	frequency
f^*	non-dimensionalized frequency: $f_s\delta/u_\tau$
F	body force
$\breve{G}_i$	spectral coefficients of the combined convection and body force
ɨ	imaginary unit:$\sqrt{-1}$
k	wavenumber
k_u	turbulence kinetic energy (TKE)
l	integral length scale of turbulence
L	channel length
M	meandering ratio: σ_c^2/σ_r^2
N	number of grid nodes
p	pressure
P_{ij}	projection tensor

Pr	probability
r	local ratio of the upstream to downstream gradient in the concentration field
$R_{w'w'}(\tau)$	autocorrelation function of the spanwise velocity fluctuations at spatial lag τ
Re_F	forcing Reynolds number: $\epsilon_F^{1/3} k_0^{-4/3}/\nu$
Re_λ	Reynolds number based on Taylor microscale: $\hat{u}\lambda/\nu$
Re_τ	Reynolds number based on the wall friction velocity: $u_\tau \delta/\nu$
s	left-shifted clipped-gamma variable
S	concentration source strength
Sc	Schmidt number: ν/α
t	time
t_L	Lagrangian time scale
T_c	temporal interval for channel flow: δ/u_τ
T_h	temporal interval for homogeneous isotropic box: $2\pi/\hat{u}$
u	velocity component in the streamwise direction
u_i	velocity components: $i = 1, 2, 3$
u_τ	wall friction velocity
U	mean velocity in the streamwise direction
v	velocity component in the wall-normal direction
w	velocity component in the spanwise direction
x_i	coordinates: $i = 1, 2, 3$
z_c	instantaneous plume centroid

Greek Symbols:

α	molecular diffusivity of the scalar
β	Pasquill and Smith proportionality constant
γ	the intermittency factor
$\Gamma(x)$	gamma function
δ	channel height
δ_1	the second-order central-difference operator
$\delta(x)$	Dirac delta function
Δ	grid size
Δ_1	TVD operator
ΔT	time step
ϵ	rate of energy dissipation per unit mass
ϵ_F	energy injection rate
ζ	left-shifted clipped-gamma variable
η	Kolmogorov length scale
κ	left-shifted clipped-gamma variable
λ	Taylor micro-scale of turbulence
Λ	size of turbulent eddies
μ	dynamic viscosity
ν	kinematic viscosity
ξ	the spanwise location of the centroid of the plume
$\rho^{[1\|1]}$	cross correlation coefficient between concentration fluctuations or the second-order correlation function
$\rho_f^{[1\|1]}$	coherency spectrum in frequency space
$\rho_{k_z}^{[1\|1]}$	coherency spectrum in wavenumber space
ρ	density
σ_c	instantaneous plume centroid dispersion
σ_r	relative plume dispersion
σ_y	mean plume dispersion in y direction

σ_z	mean plume dispersion in z direction
Σ_r	relative plume half width
Σ_z	mean plume half width in z direction
φ	limiter function
χ	the value that can be assumed by a random variable
ψ	generic variable

Subscripts and Superscripts:

$(\cdot)_A$	value for the plume released from source A
$(\cdot)_B$	value for the plume released from source B
$(\cdot)_e$	value at the east grid node
$(\cdot)_F$	value for artificial body force
$(\cdot)_L$	value in Lagrangian frame
$(\cdot)_m$	maximum value
$(\cdot)_{mid}$	value at the midpoint in the spanwise direction between the two plumes
$(\cdot)_r$	value in the relative frame
$(\cdot)_s$	value at the source
$(\cdot)_T$	value for the total plume
$(\cdot)_w$	value at the west grid node
$(\cdot)_x$	streamwise components
$(\cdot)_y$	wall-normal components
$(\cdot)_z$	spanwise components
$(\bar{\cdot})$	time averaged quantity or mean
$(\cdot)^+$	value in wall coordinates
$(\cdot)^*$	first intermediate component
$(\cdot)^{**}$	second intermediate component
$(\cdot)^\star$	conjugate of a complex number
$(\cdot)'$	fluctuating component
$(\hat{\cdot})$	root-mean-squared quantity
$(\breve{\cdot})$	value in the Fourier space
$\overline{(\cdot)}^{1x}$	the simple averaging
$\overline{(\cdot)}^{1\breve{x}}$	the volume averaging
$(\cdot)^n$	value at the previous time step
$(\cdot)^{n+1}$	value at the current time step
$(\cdot)^m$	mth central moments of the plume concentration fluctuations

Abbreviations:

ADI	Alternative Directional Implicit
DNS	Direct Numerical Simulation
EDF	Exceedance Distribution Function
ES	Elevated Source
GLS	Ground-Level Source
LES	Large-Eddy Simulation
max	Maximum
min	Minimum
MPI	Message Passing Interface
PDF	Probability Density Function
RF	Reduction Factor
RMS	Root-Mean-Square
RSM	Reynolds Stress Model
SMART	Sharp and Monotonic Algorithm for Realistic Transport
TKE	Turbulent Kinetic Energy
TVD	Total Variation Diminishing
WestGrid	Western Canada Research Grid

Chapter 1

Introduction

1.1 Motivation

In engineering and natural sciences, it is frequent to observe physical phenomena that involve transport and mixing of various scalars from multiple sources in a turbulent flow. For example, in studies of combustion, it is important to understand how the rates of competitive-consecutive reactions depend on the rate of turbulent mixing of different scalars released from various sources within a turbulent flow. In nature, the ability to determine precisely the locations of multiple food sources using the olfactory system is critical to the survival of many animals such as dogs, cats and wild hogs. Also, in natural and urban environments, pollutants are often seen to be released from multiple sources that are close to each other in the atmospheric boundary layer. Imagine leakages in tanker cars of a train carrying non-toxic chemical materials. Although individual release of these materials into the atmosphere is not hazardous, but the mixing of them may lead to a chemical reaction which might produces toxic materials. The dosage of the produced toxic materials highly depends on the reaction rate which itself is a function of the rate of turbulent mixing of the reactants. To study these types of phenomena, it is important to develop a thorough physical understanding of the interference associated with the mixing of scalar fields released from the various sources.

Although the mean total concentration (first-order moment) from multiple sources can be determined using the principle of linear superposition based on the mean concentration of single plumes, this is not the case for the higher-order moments of the scalar (e.g., concentration variance, skewness and kurtosis). The study of the dispersion and mixing of multiple plumes is complicated by the discrepancy between the characteristic length scales associated with the velocity and scalar fields. The relative ratio between the scalar and velocity scales results in different physical mechanisms for the stirring and mixing of the scalar in a plume and for the interaction between plumes. In the following context, a brief review of relevant studies of dispersion phenomenology for single and multiple plumes is provided.

1.2 Previous Work

In this section, a concise literature review of the dispersion of a plume released from a single source is provided, followed by a detailed literature survey of the dispersion and mixing of plumes released from multiple sources in different types of turbulent flows.

1.2.1 Single plume dispersion

Since the pioneering work of Taylor (1935) on the mixing of a scalar in a turbulent flow, there have been many theoretical, experimental, and numerical studies related to the dispersion of a single passive scalar. Warhaft (1984) and Stapountzis et al. (1986) investigated the turbulent dispersion of heat from line sources in grid turbulence. In the study of Stapountzis et al. (1986), the Lagrangian stochastic model developed by Sawford and Hunt (1986) was used to interpret the results of the scalar dispersion experiments. Anand and Pope (1985) developed an analytical solution for the mean plume spread using a single particle model for dispersion in decaying homogeneous turbulence. They identified three distinct regimes in the streamwise development of a dispersing plume: namely, the molecular diffusive, turbulent convective, and turbulent diffusive regimes.

Turbulent dispersion of a scalar in a shear flow is of significant practical value in engineering applications, as most of the flows encountered in practice involve wall shear or free shear stresses (e.g., boundary layers, wakes, and jets). Fackrell and Robins (1982) conducted wind-tunnel experiments to investigate the concentration fluctuations and fluxes for passive scalar releases from both elevated and ground-level point sources in a turbulent boundary layer. Their comprehensive study of concentration fluctuations from point sources included the measurement of statistics such as concentration variance, intermittency and concentration probability density function (PDF). They also examined the relative magnitudes of terms in the concentration variance transport equation in order to elucidate the nature of the sources/sinks responsible for the streamwise evolution of concentration fluctuations. Based on their extensive study, Fackrell and Robins (1982) further quantified the influence of source size on the maximum attainable level of concentration fluctuations. Lavertu and Mydlarski (2005) investigated the effect of shear on scalar dispersion by conducting an experimental study of a plume released from an elevated line sources in a fully developed high-aspect-ratio turbulent channel. In contrast to studies of dispersion conducted in homogeneous flows, their experimental results of dispersion in a turbulent channel flow did not show a power-law growth rate for the mean plume width or the reappearance of the off-axis peaks in the concentration variance profiles at locations far downstream of the release.

Sykes and Henn (1992) used large-eddy simulation (LES) to investigate the statistics of the fluctuating concentration field arising from the release of a passive scalar from both elevated and ground-level continuous point sources into a neutrally stratified boundary-layer flow. They found that the concentration statistics near the wall surface for both sources obtained from LES were not in good agreement with the experimental observations of Fackrell and Robins (1982). They attributed the discrepancies to the fact that in the vicinity of the wall boundary, most of the turbulence energy in the flow is modeled rather than explicitly resolved in a LES approach. Discrepancies between LES and experimental results for the concentration statistics near the wall surface have also been observed by Xie et al. (2004) and Boppana et al. (2012). Boppana et al. (2012) related these discrepancies to the lack of near-wall data, wall-probe interference effects, experimental scatter, and the lack of a wall temperature measurement.

On the other hand, direct numerical simulation (DNS) has been proven to be a powerful tool for studying the dispersion of a passive plume in shear flows (Bernard and Rovelstad, 1994; Brethouwer et al., 1999; Orlandi and Leonardi, 2004). In DNS, all scales of flow motions ranging from the smallest Kolmogorov scales to the largest integral scales need to be resolved. Therefore, it produces the most accurate results for the velocity and scalar statistics compared to LES studies. Bernard and Rovelstad (1994) performed DNS of scalar fields released from uniform line sources in a low Reynolds number channel flow, and used the DNS data to further evaluate the predictive accuracy of different turbulence closure models for the scalar transport equation. Brethouwer et al. (1999) investigated the dispersion of a passive plume released from a point source in a fully-developed turbulent pipe flow using DNS. They analyzed results of the mean concentration, scalar fluxes, concentration fluctuations, concentration PDF and higher-order concentration moments. Orlandi and Leonardi (2004) conducted DNS of a passive scalar in a turbulent channel flow. They assigned a normal velocity disturbance on the lower wall in order to reproduce the complex physics of turbulent rough-wall flows without having to deal with the geometric complexity.

1.2.2 Multiple plume dispersion and mixing

In the current literature, studies of passive dispersion in turbulent flows are primarily limited to single plume dispersion problems. There are a few studies on dual plume dispersion in boundary layer flows and homogeneous isotropic turbulence based on experimental and numerical approaches. Warhaft (1981) measured the temperature covariance and cross correlation in decaying grid turbulence between two thermal wakes produced by two parallel ‘mandolines’ (fine heated wires) in a wind tunnel. In this experiment, it was observed that the sum of the thermal variances produced by each mandoline operating separately was significantly less than the total variance produced by the two mandolines operating simultaneously. This deficit was attributed to the temperature covariance term.

Warhaft (1984) used the term ‘interference’ to describe the interaction of the two thermal plumes in direct analogy to the constructive and destructive interferences observed in the famous Young’s double slit experiment in the field of classical physics of light. In Young’s double slit experiment, interferences occur when light waves from two coherent sources superimpose to produce a resultant wave. Constructive and destructive interferences resulting from the linear superposition of two light waves are analogous to the positive and negative values for the cross correlation coefficient between the concentration fluctuations from the two sources, respectively. In contrast to the Young’s double slit experiment, in which the frequency of the two light waves is identical and unique, the mixing of two plumes in turbulence involves a cascade of turbulent eddies of different temporal and spatial frequencies (or wavenumbers), which impose significant challenges to the study of plume interference and make the physical phenomenon less understood. Warhaft (1984) further demonstrated that the nature of the interference in the total temperature variance field depends on the distance between the two line sources, source position from the grid, and downstream location where the measurements were taken.

Sawford et al. (1985) conducted atmospheric tracer dispersion experiments to study the variance, probability distribution, and spectrum of the concentration statistics downwind of a pair of partly overlapping plumes. The two tracers used in their study were phosphorus and sulfur hexafluoride. A key result of their study was that the probability for the instantaneous concentration to exceed the mean concentration level for two sources was generally less than that for a single source, owing to a negative cross correlation between the two plumes. This resulted in a lower intensity of fluctuations and a more nearly Gaussian probability distribution for the total concentration. Stapountzis (1988) conducted a series of wind-tunnel experiments to investigate the mixing of two passive thermal plumes generated from two line sources immersed in grid turbulence and separated in either the spanwise or streamwise directions. He found that there was a strong negative correlation between the temperature fluctuations within the meandering regime of plume development released from two transversely separated line sources, and that the correlation coefficient became positively valued when the two line sources were aligned in the streamwise direction. Tong and Warhaft (1995) investigated the dispersion and mixing of passive scalars produced by two heated fine rings placed axisymmetrically in a turbulent jet. Their results on the coherency spectrum of concentration fluctuations of the two plumes showed that the small scales lag behind the large scales in the mixing of two plumes. Davis et al. (2000) studied the interaction of plumes released from two point sources into the atmospheric boundary layer. Their measurement results on two laterally separated sources showed that the correlation between the concentration fluctuations of the two plumes change from negative to positive as the downwind distance increases for a fixed source separation distance, or as the source separation distance decreases for a fixed downwind location. Costa-Patry and Mydlarski (2008) conducted a wind-tunnel experiment to quantify the interaction of two scalar fields generated by two line sources (separated in the wall-normal direction) in a fully-developed high-aspect-ratio turbulent channel flow. Their results on the co-spectrum and the coherency spectrum revealed that the large scales (occurring at low frequencies) of plume mixing evolve more rapidly than the small scales (occurring at high frequencies).

Besides the experimental efforts reviewed above, there have been a couple of important numerical studies. Kaplan and Dinar (1989) investigated the interference of two scalars diffusing in homogeneous isotropic turbulence using a three-dimensional model based on a Lagrangian statistics approach. Using this model, they calculated the cross correlation coefficient between the concentration fluctuations of the two plumes. They found that the cross correlation coefficient depends on not only the source separation distance scaled by the Eulerian length scale, but also on the geometry and size of the sources. Vrieling and Nieuwstadt (2003) performed DNS to study the interference of two line sources in a plane-channel flow. They placed the sources near the center of the plane channel, where turbulence conditions are close to being homogeneous.

In literature, there are also two theoretical investigations of dual plume interference. Vrieling and Nieuwstadt (2003) obtained an analytical equation for calculating the variance of the total concentration fluctuations using a generalization of the meandering plume model of Gifford (1959). This model allowed them to predict the nature of the interference in the plume concentration statistics in the regime of plume development where the meandering effect is dominant. However, at a sufficiently large downstream distance from the sources where the in-plume mixing (internal fluctuations) are dominant, the model for the cross covariance of the concentration from the two sources is (not surprisingly) in poor conformance with the DNS data for this quantity. Yee et al. (2003) used a meandering plume model incorporating internal fluctuations to provide explicit analytical expressions for various higher-order joint concentration statistics for plume fluctuations arising from a two-point source release in homogeneous isotropic turbulence. Their results for the second-order correlation function (cross correlation) between the concentration fluctuations of scalars released from two sources were in good agreement with some experimental data for a two-point source release in grid turbulence generated in a water-channel simulation.

In spite of these experimental and numerical investigations, high-quality data sets of concentration statistics arising from the interference of scalar fields produced by two or more concentrated sources are still rather limited. In this research, DNS is used to study the interference effects on the first-, second- and higher-order concentration moments generated by the release of passive scalars from two concentrated sources into two different types of turbulent flows (i.e., a neutrally-stratified wall-bounded shear flow and homogeneous isotropic turbulent flow).

1.3 Objectives

The general objective of this research is to improve the current state of knowledge of plumes dispersion and mixing. More specifically, the studies of the wall shear effects on the dispersion and mixing of plumes are limited in the literature. In this research, these effects will be systematically studied by comparing ground-level and elevated source release scenarios. The relevant scales in the mixing of plumes are only studied in a turbulent jet by Tong and Warhaft (1995) and in a high-aspect-ratio turbulent channel flow by Costa-Patry and Mydlarski (2008). In this research, the scales of the mixing of plumes will be studied using the advanced physical analysis of the concentration co-spectrum and coherency spectrum. The current understanding of the effects of plume interference on the probability of occurrence of high concentration levels is rather limited to the study of Sawford et al. (1985). In order to provide a deeper understanding of this phenomena, the effect of the cross correlation coefficient on the concentration exceedance distribution function (EDF) will be investigated in this research. Furthermore, the relationships between the various higher-order normalized concentration moments, which have been observed by Yee and Chan (1997) for a single plume, will be further examined for the total plume. Also, the clipped-gamma model of Yee and Chan (1997), which is used for the prediction of higher-order concentration moments of a single plume, will be extended to the total plume.

To achieve the general objective of this research, following detailed objectives need to be fulfilled.

- Develop, test, validate and optimize two computer codes for DNS of dispersion and mixing of plumes released from single and multiple concentrated sources into an open-channel flow or a homogeneous isotropic turbulent flow.

- Conduct simulations to investigate the influence of various relevant physical parameters on the physical processes of dispersion and mixing of plumes. This includes a systematic examination of the effects of source separations, Reynolds number, source elevation, mean shear, and background turbulent velocity field on the dispersion and mixing of plumes.

- Produce high-quality data sets of concentration statistics arising from the single and dual-source releases into open-channel and homogeneous isotropic turbulent flows. Because DNS provides the most accurate results for scalar statistics, these data sets can be used for the validation of various analytical and numerical models on plume mixing.

- Analyze the results of a single plume dispersion to achieve a deep insight into plume dispersion characteristics in the turbulent convective and turbulent diffusive regimes of a plume development.

- Perform a systematic comparative study of the dual-plume interference in both physical and spectral spaces. This includes detailed analysis of the basic quantities such as the mean and variance of the concentration field, and advanced quantities such as the cross correlation coefficients of the dual plume, the concentration co-spectra, coherency spectra, concentration EDF, and higher-order concentration moments.

- Extend the clipped-gamma model of Yee and Chan (1997) for a single plume to predict higher-order concentration moments of the total plume. The unknown parameters in the clipped-gamma model should be first calculated for the total plume case, and then the prediction of the model will be compared to the available DNS data to verify the accuracy of the clipped-gamma model for the total plume.

1.4 Outline

The remainder of this thesis is organized as follows:

In chapter 2, the governing equations, solution algorithm and the discretization scheme are described.

In chapter 3, the dispersion and mixing of passive scalars released from two near-ground point sources into an open-channel flow at two Reynolds numbers are studied.

In chapter 4, the dispersion and mixing of passive scalars released from two ground-level and elevated point sources into an open-channel flow are studied.

In chapter 5, the dispersion and mixing of passive scalars released from two line sources into homogeneous isotropic turbulent flow are investigated.

In chapter 6, major conclusions of this research are summarized followed by comments on future studies.

Chapter 2

Numerical Method

2.1 Governing Equations

In DNS, the velocity field is governed by the continuity and momentum transport equations and the passive scalar field is governed by the advection-diffusion equation. In the context of an incompressible flow, these equations assume the following forms:

$$\frac{\partial u_i}{\partial x_i} = 0 \quad , \tag{2.1}$$

$$\frac{\partial u_i}{\partial t} + u_j \frac{\partial u_i}{\partial x_j} = -\frac{1}{\rho}\frac{\partial p}{\partial x_i} + \nu \frac{\partial^2 u_i}{\partial x_j \partial x_j} + F_i \quad , \tag{2.2}$$

$$\frac{\partial c}{\partial t} + u_j \frac{\partial c}{\partial x_j} = \alpha \frac{\partial^2 c}{\partial x_j \partial x_j} + S \quad . \tag{2.3}$$

Here, u_i is the instantaneous velocity in the x_i-direction (with $i = 1$, 2 or 3, representing the streamwise (x), vertical (y), or spanwise (z) direction respectively), c is the instantaneous concentration, p is the pressure, ρ is the density of the fluid, ν is the kinematic viscosity, α is the molecular diffusivity of the scalar, S is the concentration source strength, and the body force F_i represents an artificial forcing for sustaining the homogeneous isotropic turbulence level (this term is deactivated in the context of an open-channel flow). In this research, the Schmidt number $Sc = \nu/\alpha$ is set to 1.0.

2.2 Solution Algorithm and Discretization Scheme

The DNS for the two types of flow (open-channel and homogeneous isotropic turbulent flows) studied in this research, was conducted using two different in-house codes developed using the FORTRAN 90/95 programming language and fully-parallelized using the message passing interface (MPI) library. In the following, a summary of the algorithms used for the open-channel flow code and the homogeneous isotropic turbulent flow code are presented. A detailed description of the discretization schemes used in these two codes is delivered in appendices A and B.

2.2.1 Open-channel Flow

The open-channel flow code is an extended version of a computer code developed by LePoudre (2003). In this code, the continuity equation and the momentum transport equations were discretized using the fully conservative second-order finite difference scheme of Ham et al. (2002). The fully implicit fractional step method of Choi and Moin (1994) was used for the solution of the momentum equations, in conjunction with a multi-grid solver for the Poisson equation for the pressure which was used to enforce the continuity equation.

The advection-diffusion equation that governs the transport of the passive scalar c was solved after the solution of the momentum equations at each time step. A Crank-Nicolson scheme and a central-differencing scheme were used for the time advancement and spatial discretization of the diffusion term in the advection-diffusion equation, respectively.

In the original LePoudre (2003)'s code, a second-order central differencing scheme was used for the discretization of the convective term in the advection-diffusion equation. However, it is well known that if a second-order central-differencing scheme is used for the discretization of the convective term in the advection-diffusion equation, non-physical oscillations may occur in the solution for c which can result in unphysical negative concentrations. This problem was solved by using a total variation diminishing (TVD) scheme with the Sharp and Monotonic Algorithm for Realistic Transport (SMART) limiter function of Gaskell and Lau (1988) for the discretization of the convective term.

2.2.2 Homogeneous Isotropic Turbulent Flow

The algorithm used in homogeneous isotropic turbulent flow code is based on a pseudo-spectral method described by Orszag and Patterson (1972) and Eswaran and Pope (1988). In this method, the velocity and pressure fluctuations are expanded into Fourier series in all three coordinate directions. The convection terms in the momentum transport equation are calculated in physical space, and the aliasing error is removed using the 3/2 rule. In order to generate a mean advection of the passive scalar, a constant mean streamwise velocity of $U = 5\hat{u}$ is superimposed on the velocity fluctuations obtained from the solution of the continuity and momentum equations. Here, $\hat{u}$ is the fluctuating velocity scale that is derived from the turbulence kinetic energy (TKE) k_u as $\hat{u}^2 = 2k_u/3$.

A similar finite difference scheme described for the open-channel flow code is used to discretize the advection-diffusion equation. However in homogeneous isotropic turbulent flow code, the time advancement for both the velocity and scalar fields is achieved using the explicit fourth-order Runge-Kutta scheme.

2.3 High-Performance Computing

Numerical simulations were conducted on the Western Canada Research Grid (WestGrid), which encompasses 15 partner institutions and is one of four consortia that provides high-performance computational resources across Canada. The simulations were executed until statistically stationary conditions were attained for both the velocity and scalar fields, after which various time-averaged statistics of the instantaneous velocity field, instantaneous individual scalar fields and of the instantaneous total scalar field from the multiple sources were obtained by averaging over a temporal interval of $50T_c$ in open-channel flow where $T_c = \delta/u_\tau$, and $500T_h$ in homogeneous isotropic turbulent flow, where $T_h = 2\pi/\hat{u}$. The total computing time spent on solving the flow and scalar fields and on collecting the statistics is over 160,000 and 50,000 CPU hours for open-channel and homogeneous isotropic turbulent flows, respectively.

Chapter 3

Dispersion and Mixing of Ground-Level Plumes

3.1 Introduction

In many dispersion and mixing of plumes applications, the sources are often located at ground level, where the flow is inhomogeneous and anisotropic. This further imposes challenges to the study of the temporal and spatial development and mutual interaction of passive scalar plumes, since most of the current theoretical models available for predicting turbulent dispersion and mixing of two or more scalars have been primarily limited to homogeneous and isotropic turbulent flows.

In this chapter, DNS is used to study the dispersion and mixing of passive scalars released from two near-ground point sources in the context of a neutrally-stratified wall-bounded shear flow at two Reynolds numbers. The first- and second-order concentration statistics of the single and total plumes are analyzed, the dynamic interaction of the two plumes in a turbulent wall shear layer and the correlations between their concentration fluctuations are investigated. Furthermore, in order to develop a deeper understanding of the mixing of two plumes at different length scales, a detailed analysis based on the co-spectrum and coherency spectrum of the plumes is also performed.

3.2 Problem Description

In this chapter, the release of two plumes from two point sources in an open-channel flow at two Reynolds numbers for $Re_\tau = u_\tau \delta/\nu = 180$ and 395 is considered. Here $\delta = 0.04$ m is the height of the open channel and u_τ is the friction velocity. Figure 3.1 shows a schematic of the computational domain, which extends $4\pi\delta \times \delta \times 4/3\pi\delta$ for $Re_\tau = 180$ and $2\pi\delta \times \delta \times \pi\delta$ for $Re_\tau = 395$ in the streamwise (x), vertical (y) and spanwise (z) directions, respectively.

For the velocity field, periodic boundary conditions were applied in the streamwise and spanwise directions, and a no-slip and a free-slip boundary conditions were employed respectively on the bottom and top surfaces of the computational domain. For the concentration field, a zero Dirichlet condition was applied at the inlet boundary, and zero Neumann conditions were applied at the other boundaries (viz., the gradients of the concentration in the direction normal to the boundary are assumed to vanish identically).

The two point sources labeled 'A' and 'B' in figure 3.1 are positioned symmetrically in the spanwise (z) direction with respect to the centerline of the open channel. The two sources are of equal strength and are positioned vertically at $y_s^+ = y_s u_\tau/\nu = 5$ above the lower wall. As such, both point sources are within the viscous sublayer, corresponding to a near-ground release condition. The effects of source separation d on the interference of plumes can be significantly influenced by the Reynolds number. In order to investigate this coupled mechanism, eight different test cases are considered. Table 3.1 summarizes the Reynolds numbers and source separation distances tested. Related to the grid resolution for DNS, the source sizes σ_0 used for the two different Reynolds numbers are also given in the table.

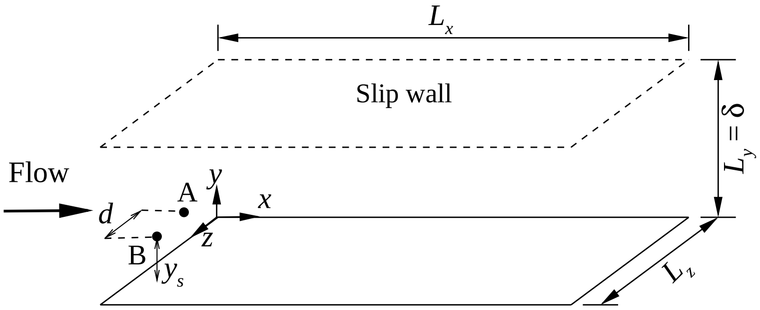

Figure 3.1: Schematic of the computational domain of the open-channel flow. Two point sources A and B are separated in the spanwise direction by a distance d and are each positioned at a distance y_s above the lower (solid) channel wall.

Table 3.1: Summary of test cases.

Case	Re_τ	Source separation (d/δ)	Source size (σ_0/δ)
1	180	0.066	0.014
2	180	0.131	0.014
3	180	0.295	0.014
4	180	0.558	0.014
5	395	0.049	0.007
6	395	0.115	0.007
7	395	0.279	0.007
8	395	0.541	0.007

3.3 Result Analysis

In this section, the DNS results of the eight test cases are analyzed, which include the velocity statistics of the first and second moments, the mean and variance of the concentration field of the single and total plumes, cross correlation coefficient of the two plumes, and co-spectrum and coherency spectrum of the two concentration fields.

3.3.1 Velocity Statistics

The focus of this research is on the interference of two instantaneous passive plumes. However, because the dispersion of passive plumes is dominated by flow convection, it is important to examine the quality of the predicted velocity field prior to the analysis of the concentration field. Figure 3.2 validates the present DNS predictions for the first- and second-order velocity statistics against some available DNS data published in the literature. The present DNS results for an open-channel flow at $Re_\tau = 180$ are compared against the open-channel DNS data of Handler et al. (1999). However, due to a lack of numerical and experimental data for an open-channel flow at $Re_\tau = 395$, the DNS results of Moser et al. (1999) for a plane-channel flow (of the same Reynolds number) are used in the comparative study. For the purpose of comparison, it should be noted that the upper boundary of the open channel coincides with the central plane (at the half-channel height) of the plane channel. All velocity statistics shown in figure 3.2 have been non-dimensionalized using the wall friction velocity u_τ.

Figures 3.2(a) and (b) show the vertical profiles of the non-dimensionalized mean streamwise velocity $U^+ = U/u_\tau$ for $Re_\tau = 180$ and 395, respectively. In addition to the DNS data of Handler et al. (1999) and Moser et al. (1999), the current DNS results for the mean streamwise velocity profiles are also compared against the classical law of the wall based on von Kármán's two-layer turbulent boundary-layer model. As shown in figures 3.2(a) and (b), the current DNS results are in very good conformance with reported data, exhibiting the expected mean streamwise velocity profile characteristics for a wall shear flow.

Figures 3.2(c) and (d) show the vertical profiles of the three components of the non-dimensionalized root-mean-square (RMS) velocities (i.e., $\hat{u}/u_\tau$, $\hat{v}/u_\tau$, and $\hat{w}/u_\tau$) for the two Reynolds numbers tested. For the lower Reynolds number case ($Re_\tau = 180$), the RMS velocities predicted by the current simulation are in excellent agreement with the DNS results of Handler et al. (1999). As shown in figure 3.2(c), for the case of $Re_\tau = 395$, the current simulation has well predicted the three RMS velocity components in the near-wall region and throughout most of the channel below the free surface (upper boundary) in comparison with the reported DNS results of Moser et al. (1999) on a plane-channel flow. However, close to the upper boundary, there are some discrepancies between the current and reported DNS results, especially as

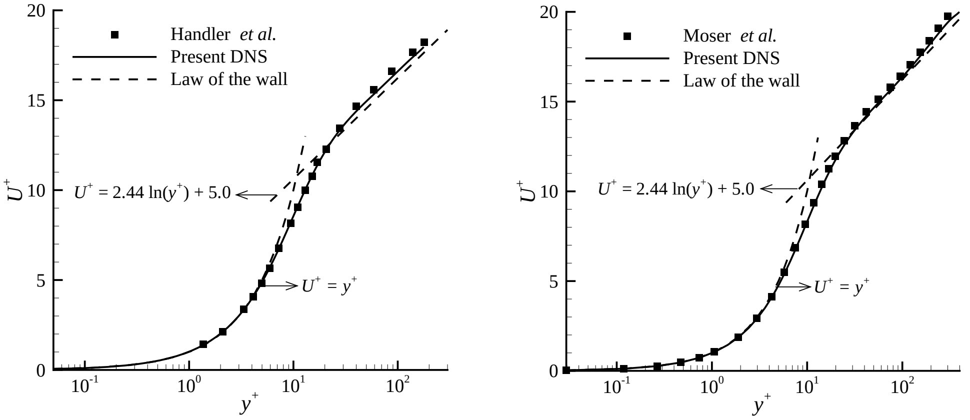

(a) Mean velocity ($Re_\tau = 180$) (b) Mean velocity ($Re_\tau = 395$)

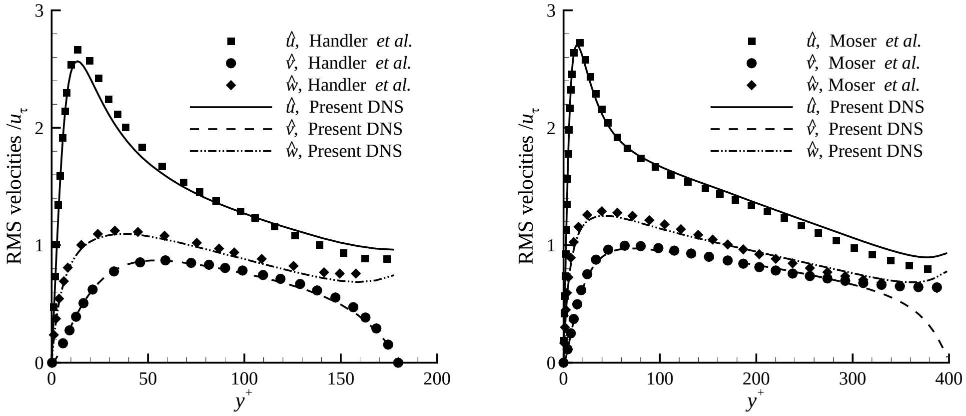

(c) RMS velocities ($Re_\tau = 180$) (d) RMS velocities ($Re_\tau = 395$)

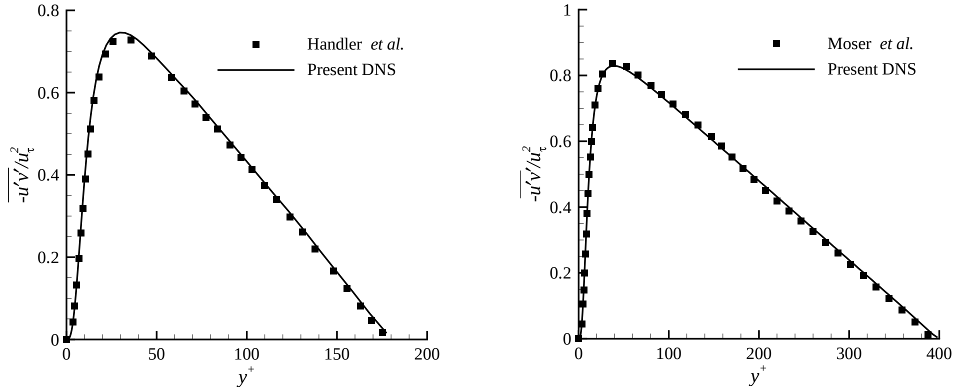

(e) Reynolds shear stress ($Re_\tau = 180$) (f) Reynolds shear stress ($Re_\tau = 395$)

Figure 3.2: Comparison of present DNS predictions of the velocity statistics of an open-channel flow against reported DNS data of Handler et al. (1999) for an open-channel flow and those of Moser et al. (1999) for a plane-channel flow. All flow statistics are non-dimensionalized using the wall friction velocity u_τ.

it pertains to the prediction of the wall-normal component $\hat{v}/u_\tau$. The value of $\hat{v}/u_\tau$ for the current open channel approaches zero at the upper boundary, while that of the plane channel reaches a nonzero value. These discrepancies are expected, as they reflect the differences between the current open-channel flow case and the plane-channel flow case of Moser et al. (1999). In an open channel, the flow boundary condition is prescribed as being free-slip (and therefore, non-penetrative in the wall-normal direction) along the free surface; however, this restriction does not hold along the central plane (at the half-channel height) in a plane-channel flow.

Figures 3.2(e) and (f) compare the predicted non-dimensionalized vertical profiles of Reynolds shear stress $-\overline{u'v'}/u_\tau^2$ with the reported DNS data for $Re_\tau = 180$ and 395, respectively. As is clearly shown in both these figures, the agreement between the current and previously reported DNS data sets is excellent, and the effects of wall anisotropy on the Reynolds shear stress profile is evident at both Reynolds numbers.

3.3.2 Mean Concentration

With reference to the streamwise development of a single plume, three regimes can be identified using the relative width (size) of the instantaneous plume; namely, (1) the molecular diffusive range where the width of the instantaneous plume is smaller than the Kolmogorov microscale, (2) the turbulent convective range where the width of the instantaneous plume is smaller than the size of the most energetic turbulent eddies, and (3) the turbulent diffusive range where the instantaneous plume width is of the same order or larger than the size of the most energetic turbulent eddies. Figure 3.3 shows a schematic of these three regimes of plume development. In the molecular diffusive range, the molecular diffusion is the dominant mechanism in the plume dispersion. Because the grid resolution for the current DNS is of same order as the Kolmogorov microscale, it is not possible to simulate computationally the molecular diffusive regime of plume development (which requires a study of the detailed physics of the flow and dispersion at scales finer than the Kolmogorov microscale).

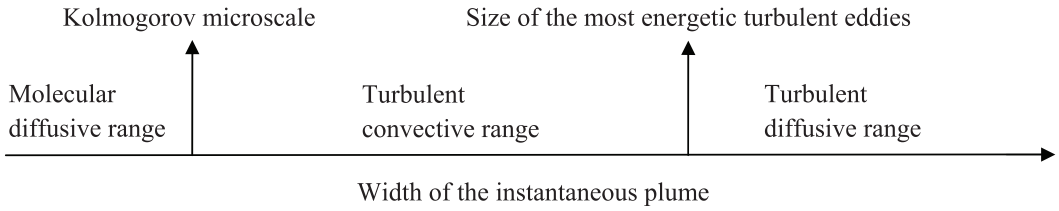

Figure 3.3: The relative width of the instantaneous plume at different regimes of plume development.

In the turbulent convective range, the width of the instantaneous plume is relatively small in comparison with the size of the most energetic turbulent eddies. Eddies that are smaller in size than the instantaneous plume contribute to internal development of the plume, associated with relative dispersion and internal fluctuations. In contrast, eddies with sizes that are greater than the instantaneous width of the plume contribute to the bulk meandering of the plume, associated with external fluctuations of the passive scalar. In the turbulent convective regime of plume development, the bulk meandering of the instantaneous plume provides the primary contribution to scalar fluctuations. However, its effect decreases as the downstream distance from the source increases. This is because as the downwind fetch from the concentrated (point) source increases, the instantaneous plume width increases relative to the size of the most energetic turbulent eddies. In the far downstream region of the source, the instantaneous plume width becomes comparable to and eventually larger than the size of the most energetic turbulent eddies. The development of the instantaneous plume then transitions into the turbulent diffusive regime where the major contribution to the scalar fluctuations arises from the internal fluctuations (in-plume mixing processes) and the effects of plume meander is minimal or zero.

The turbulent diffusive range of the plume development in the region far downstream of the source can be precisely identified using spectra of the velocity field. The spectrum of the spanwise velocity fluctuations is defined as

$$E_{w'w'}(k_z) = \frac{1}{2\pi}\int_{-\infty}^{\infty} e^{-\imath k_z \tau} R_{w'w'}(\tau) d\tau \quad , \tag{3.1}$$

where $\imath = \sqrt{-1}$ is the imaginary unit, k_z is the wavenumber and $R_{w'w'}(\tau)$ is the autocorrelation function of the spanwise velocity fluctuations at spatial lag τ, and $R_{w'w'}(\tau)$ is given by

$$R_{w'w'}(\tau) = \frac{\overline{w'(z)w'(z+\tau)}}{\hat{w}^2} \quad . \tag{3.2}$$

Figure 3.4(a) shows the velocity spectra $E_{w'w'}(k_z)$ plotted against the wavenumber k_z for the two Reynolds number flows. The velocity fluctuations used for the computation of these spectra were obtained at the source height $y_s^+ = 5$. In order to clearly show the size of the most energetic eddies, it is more convenient to display the velocity spectra pre-multiplied by the wavenumber (i.e., $k_z E_{w'w'}(k_z)$) plotted against the normalized spanwise wavelength $\Lambda_z/\delta = 2\pi/(k_z\delta)$, as it is shown in figure 3.4(b). The wavelength corresponding to the spectral peak in this figure is associated with the size of the most energetic turbulent eddies (i.e., $\Lambda_{z,m}$) of the flow, and its value is $\Lambda_{z,m}/\delta = 0.597$ and 0.283 for $Re_\tau = 180$ and 395, respectively. The turbulent diffusive range can be identified (approximately or better) using the criterion that the turbulent diffusive range corresponds to that range of downwind fetches where the width of the instantaneous plume exceeds the 'size' of the most energetic turbulent eddies[1] (viz., where $2\Sigma_r \geq \Lambda_{z,m}$). Here, Σ_r is the half width of the instantaneous plume in the spanwise direction and is defined as the plume spread over which the instantaneous concentration decreases to about 1% of its maximum value. To understand these concepts better, the example of a Gaussian distribution can be used. If the averaged instantaneous plume profile in the relative frame is Gaussian[2], then $2\Sigma_r = 2 \times 3\sigma_r = 6\sigma_r \geq \Lambda_{z,m}$. For the two Reynolds numbers tested, the wavelengths correspond to $\sigma_r/\delta \geq 0.1$ and 0.047 (equivalently, $\sigma_z/\delta \geq 0.111$ and 0.052) for $Re_\tau = 180$ and 395, respectively. Here, σ_z and σ_r represent the mean and relative plume dispersion, respectively.

The mean plume dispersion $\sigma_z(x)$ (of a single plume) in the lateral direction at

---

[1] The beginning of the turbulent diffusive range occurs when the instantaneous plume width is comparable to the size of the most energetic eddies in the flow.

[2] This is reasonable assumption at downstream locations close to the source (Warhaft, 1984).

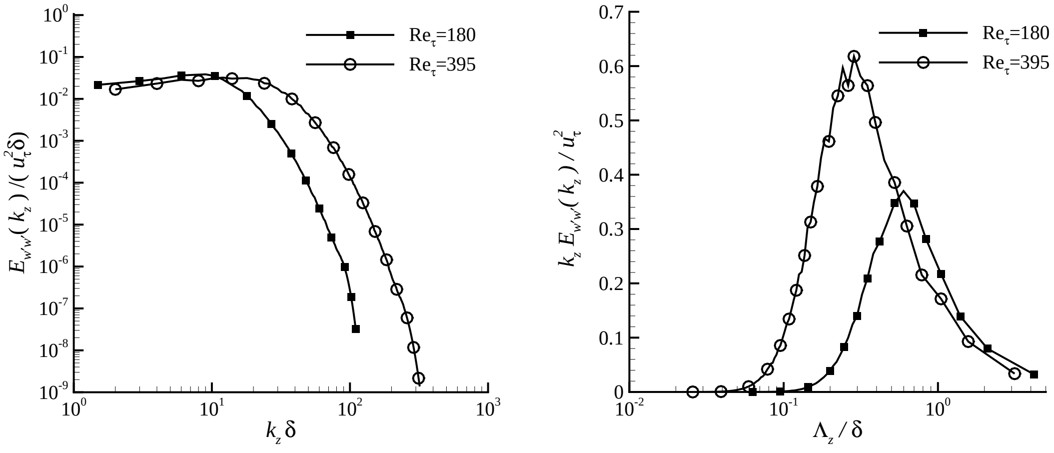

(a) Velocity spectra plotted against the spanwise wavenumber

(b) Pre-multiplied velocity spectra plotted against spanwise wavelength

Figure 3.4: Spanwise velocity fluctuations spectra and pre-multiplied spanwise velocity fluctuations spectra at $y_s^+ = 5$.

source height y_s is defined as

$$\sigma_z^2(x) = \frac{\int (z-\xi)^2 C(x, y_s, z) dz}{\int C(x, y_s, z) dz} \quad , \tag{3.3}$$

where C is the mean concentration, and ξ is the spanwise location of the centroid of the plume within the plane (parallel to the bottom plate) at the source height, defined as

$$\xi(x, y_s) = \frac{\int z C(x, y_s, z) dz}{\int C(x, y_s, z) dz} \quad . \tag{3.4}$$

The relative dispersion with respect to the centroid of the instantaneous plume (that is associated with internal fluctuations within the plume), and the dispersion of the centroid of instantaneous plume itself (that is associated with the bulk meandering of the plume) are the two physical mechanisms that are responsible for the growth of the mean plume. The mean plume dispersion σ_z, the relative plume dispersion σ_r and the dispersion of the center of instantaneous plume σ_c are related by

$$\sigma_z^2 = \sigma_r^2 + \sigma_c^2. \tag{3.5}$$

Figure 3.5 shows a schematic of mean and relative dispersion for a single plume release case. In this figure, $c_r(t, z)$ and $C_r(z)$ represent the instantaneous and mean concentration in the relative frame and $z_c(t)$ is the centroid of the instantaneous plume. The value of σ_c can be calculated using a given time series of $z_c(t)$. Once the values of σ_z and σ_c are available, σ_r can be evaluated using equation 3.5. The streamwise variation of the non-dimensionalized lateral mean plume dispersion (σ_z/δ) and the meandering ratio (defined as $M = \sigma_c^2/\sigma_r^2$) at source height is shown in figures 3.6(a) and (b), respectively. Figure 3.6(a) shows that the mean plume dispersion for $Re_\tau = 180$ is larger than that for $Re_\tau = 395$ at a given downstream location. This is because the streamwise convection is stronger at a higher Reynolds number, and therefore, the plume has less time to spread over the same downstream distance. Figure 3.6(b) shows the Reynolds number effect on the meandering ratio. As the Reynolds number increases from 180 to 395, the value of M decreases at a given location downstream of the point source. This indicates that the effect of meandering decreases and that of the relative dispersion increases as the mean streamwise velocity increases. Furthermore, as shown in figure 3.6(b), the value of the meandering ratio decreases rapidly as the downstream distance increases. This is because the plume size near the source is much smaller than the size of the energetic eddies in the near-source region, and in this regime of plume development, the bulk flapping of the plume provides the dominant contribution to the plume concentration fluctuations. As the downstream distance from the source increases, the plume grows in size, the meandering effect reduces and the mechanism of relative dispersion becomes more and more prominent.

In figures 3.6(a) and (b), the downstream positions where the width of the instantaneous plume reaches the size of the most energetic turbulent eddies are indicated using a dash and dash-dot-dotted lines for $Re = 180$ and 395, respectively. Downstream of these positions, the plume is in the turbulent diffusive range, whereas, upstream of these positions, the plume is either in the turbulent convective range or in transition to the turbulent diffusive range. Apparently, both ranges of plume diffusion have been well captured by the simulation at the two Reynolds numbers.

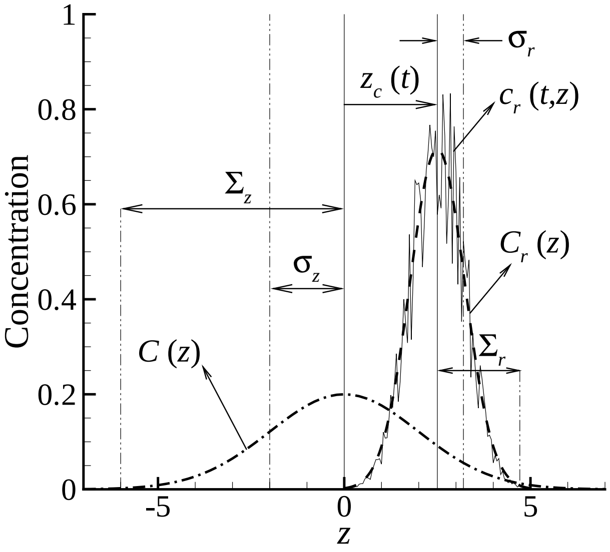

Figure 3.5: Schematic of the plume scales.

As shown in the figure, the beginning of the turbulent diffusive regimes occur at $x/\delta = 1.5$ and 0.6 for $Re_\tau = 180$ and 395, respectively.

As can be seen in figure 3.6, the instantaneous plume width for the lower Reynolds number flow reaches the size of the most energetic eddies in the flow at a greater downwind distance from the source than that for the higher Reynolds number flow. As shown previously in figure 3.4, this is due to the fact that the size of the most energetic eddies is larger for $Re_\tau = 180$ than that for $Re_\tau = 395$. This also causes the meandering ratio M for $Re_\tau = 180$ to be larger than that for $Re_\tau = 395$ as is shown in figure 3.6(b). Figure 3.6(b) also shows that when the width of the instantaneous plume reaches the size of the most energetic turbulent eddies, the meandering ratio is approximately equal to 0.25 for both Reynolds numbers (i.e. $M = 0.25$, as indicated using a horizontal solid line).

The scalar transport equation represented by equation 2.3 is linear with respect to the instantaneous concentration c field. Therefore, the mean concentration fields generated by the two point sources are linearly superposable and the total mean concentration can be simply determined as $C_T = C_A + C_B$. The mean concentration

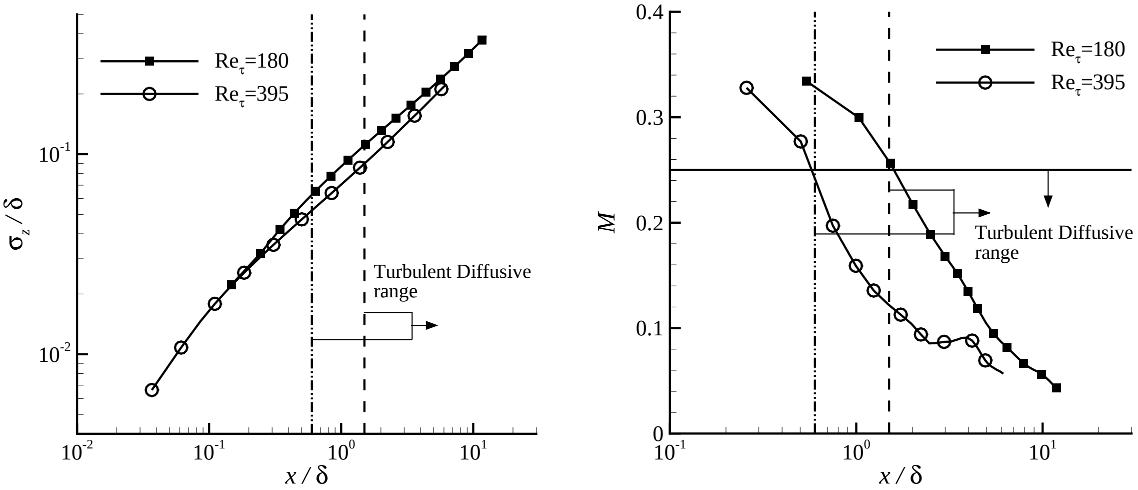

(a) Non-dimensionalized lateral mean plume dispersion

(b) Meandering ratio

Figure 3.6: Streamwise variation of the non-dimensionalized lateral mean plume dispersion (σ_z/δ) and meandering ratio ($M = \sigma_c^2/\sigma_r^2$) at source height. The dashed and dash-dot-dotted vertical lines show the locations where the width of the instantaneous plume first reaches the size of the most energetic turbulent eddies for $Re_\tau = 180$ and 395, respectively.

profiles of the single and total plumes for cases 3 and 7 are shown in figure 3.7 at three downstream locations corresponding to $x/\delta = 1$, 3 and 6. In this figure, the mean concentration has been non-dimensionalized using the concentration level at the source C_s. As shown in figures 3.7(a) and (b), close to the source, the total mean concentration profiles exhibit a dual-peak pattern, and the lateral positions of the dual-peaks coincide with the lateral positions of the two sources located at $z/\delta = 1.95$ and 2.25 for $Re_\tau = 180$ and at $z/\delta = 1.43$ and 1.71 for $Re_\tau = 395$, respectively. However, as the downwind distance from the sources increases, the distinct dual-peak pattern in the total mean concentration evident at the near-source locations disappears. As is clear in figures 3.7(c)-(f), the lateral profile of the total plume (as the linear superposition of the mean concentration from the two single plumes) transitions to a single-peak pattern. This transition is due to the fact that in the far downstream regions at $x/\delta = 3$ and 6, the two single plumes spread significantly in the lateral direction, such that the peak value of each single plume begins to merge with each other. Due to the equal strength of the two sources, the profile of the total concentration always shows a perfect symmetry in the lateral direction. By comparing figures 3.7(c) with 3.7(d) and 3.7(e) with 3.7(f), it is clear that the transition from the dual-peak to single-peak pattern in the total mean concentration profile occurs earlier in case 3 than in case 7. This physical feature is expected, and is consistent with the previous analysis of the single plume in figure 3.6(a) which indicates that the single plume width is wider in the lateral direction at the lower Reynolds number (case 3) than at the higher Reynolds number (case 7). As such, the peak value of the single plume is smaller at the lower Reynolds number, which facilitates the transition from the dual-peak to the single-peak pattern in the total mean plume.

Figure 3.8 shows the mean concentration profiles of the total plume for cases 3 and 7 at $x/\delta = 6$ for six values of y^+. In general, the profiles of the mean total plume exhibit Gaussian patterns at these six elevated positions relatively far downstream of the sources. It is seen that as the vertical distance above the source increases, the mean concentration level decreases monotonically. By comparing figures 3.8(a) and (b), it is clear that for a fixed y^+ value, the mean concentration level of case 3 ($Re_\tau = 180$) is higher than that of case 7 ($Re_\tau = 395$). This feature is expected. As the Reynolds number increases, the streamwise convection becomes stronger and the total plume is less spread in the vertical direction.

3.3.3 Variance of Concentration Fluctuations

In the previous subsection, it has been demonstrated that first-order concentration statistics of two plumes are linearly superposable. However, the second-order concentration statistics of two plumes are not linearly superposable. Specifically, it is known that $\overline{c_T'^2} \neq \overline{c_A'^2} + \overline{c_B'^2}$ holds generally, which arises from the nonlinear characteristics (in terms of second- and higher-order concentration statistics) of dual-plume interference. Figures 3.9(a) and (b) show the lateral profiles of the sum of the variances of concentration fluctuations of each single plume (i.e., $\overline{c_A'^2} + \overline{c_B'^2}$) and the variance of

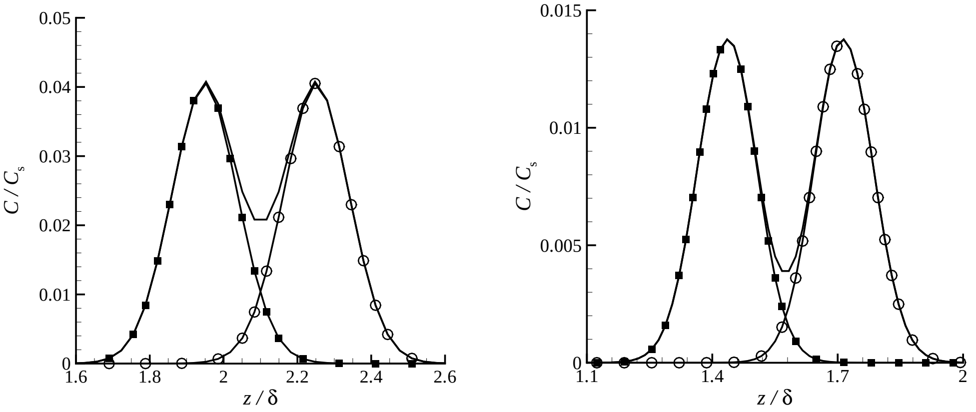

(a) Case 3 at $x/\delta = 1$ (b) Case 7 at $x/\delta = 1$

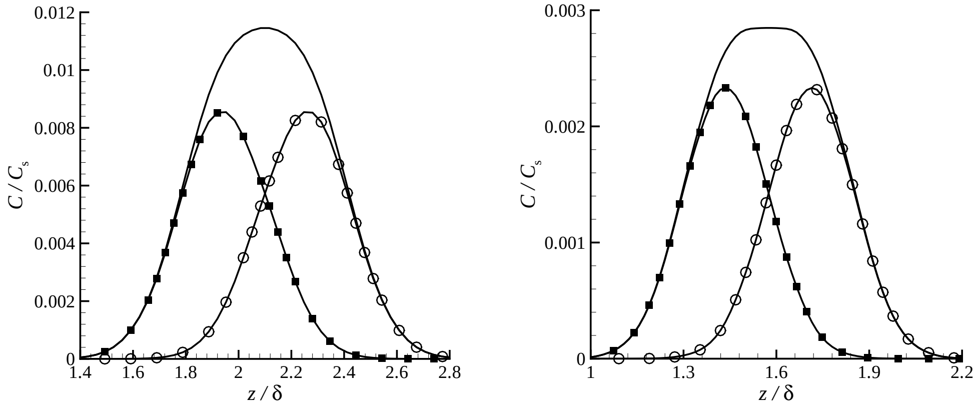

(c) Case 3 at $x/\delta = 3$ (d) Case 7 at $x/\delta = 3$

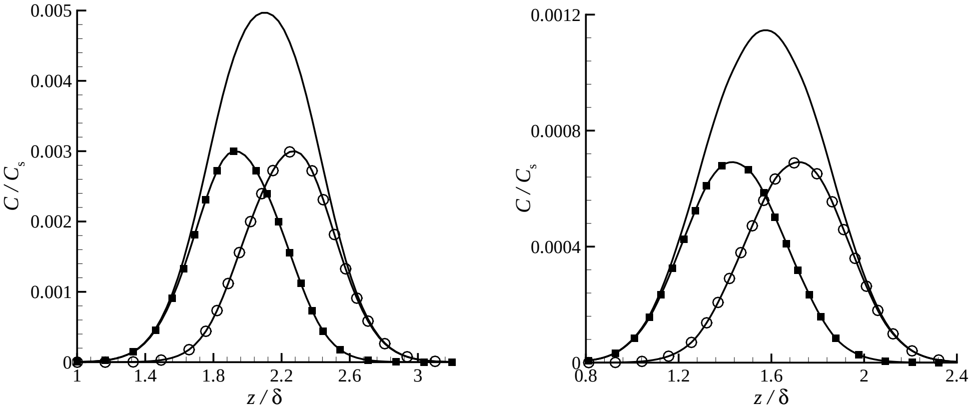

(e) Case 3 at $x/\delta = 6$ (f) Case 7 at $x/\delta = 6$

Figure 3.7: Lateral profiles of the mean concentration for the source at A (■), for the source at B (◯), and for both sources (solid line) at three streamwise locations.

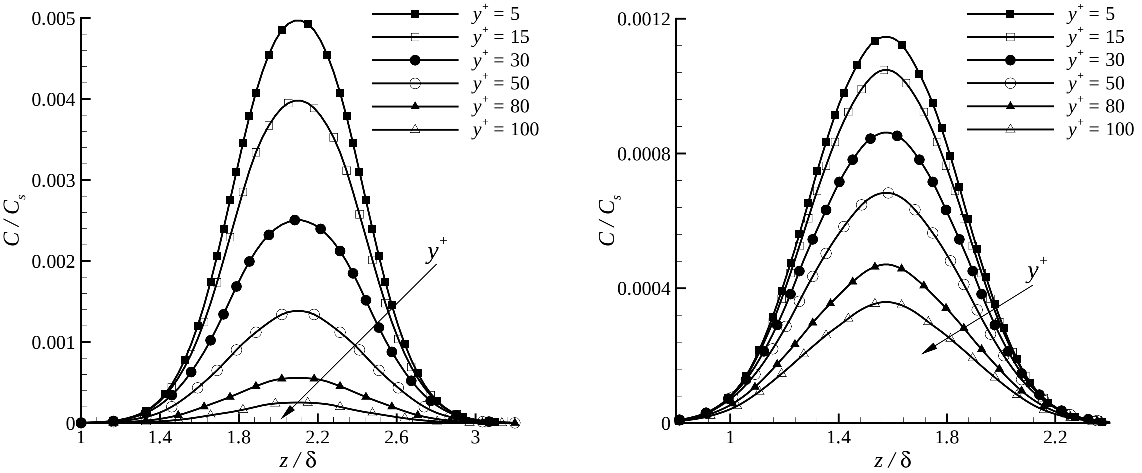

(a) Case 3

(b) Case 7

Figure 3.8: Lateral profiles of the total mean concentration for different y^+ values at $x/\delta = 6$. The arrow points to the increasing direction of y^+.

concentration fluctuations of the total plume (i.e., $\overline{c_T'^2}$) at $x/\delta = 4$ for cases 3 and 7, respectively. The ordinate of this figure is non-dimensionalized by the maximum variance of the concentration fluctuations for the total plume ($\overline{c_{T,m}'^2}$). As is evident from the figure, the sum of the variances is not equal to the variance of the total plume in general. For cases 3 and 7, within the central lateral region between the two sources, the sum of the variances is larger than the variance of the total plume; whereas, in the immediate lateral region of the two sources, the sum of the variances is smaller than the variance of the total plume. Furthermore, only in the far lateral regions of the sources does the sum of the variances equal the variance of the total plume.

The above observations can be precisely explained using the following identity

$$\overline{c_T'^2} = \overline{(c_A' + c_B')^2} = \overline{c_A'^2} + \overline{c_B'^2} + 2\overline{c_A' c_B'} \quad , \tag{3.6}$$

where c_A' and c_B' are the fluctuating components of the instantaneous concentration for the plumes released from sources A and B, respectively, and $\overline{c_A' c_B'}$ is the covariance of the concentration fluctuations of the two plumes. Equation 3.6 indicates that the variance of concentration fluctuations of the total plume produced by the two

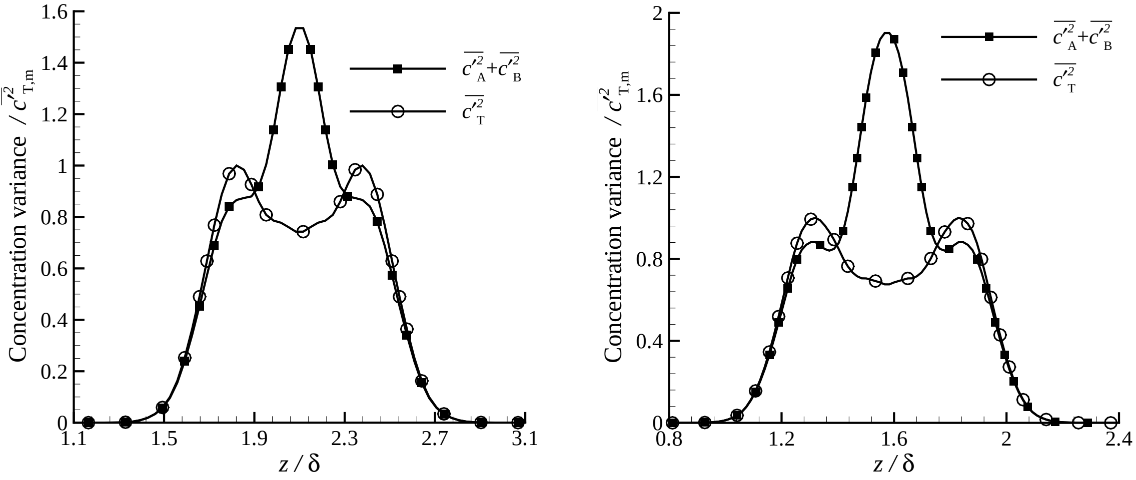

(a) Case 3

(b) Case 7

Figure 3.9: Lateral profiles of the variance of concentration fluctuations at $x/\delta = 4$.

point sources is not linearly superposable, because an additional term relating to the covariance of two single plumes needs also to be included. In the far lateral region, because the covariance between the two plumes decreases significantly ($\overline{c'_A c'_B} \to 0$), the variances of concentration fluctuations of two plumes become approximately superposable. In the remainder of this chapter, the relationship between the mean (C_T) and the variance ($\overline{c'^2_T}$) of the total plume is examined, and the property of the covariance of the concentration fluctuations of two instantaneous plumes will be further examined using the cross correlation coefficient, concentration co-spectrum and coherency spectrum.

Through the previous analysis, it has been shown that the turbulent diffusive range in the streamwise plume development starts at $x/\delta = 1.5$ and 0.6 for $Re_\tau = 180$ and 395, respectively. Within the turbulent diffusive range, the external plume fluctuations (e.g., meandering effect) is small in comparison with that of the internal plume fluctuations (e.g., relative dispersion and in-plume mixing). The production term in the transport equation for the variance of concentration fluctuations is proportional to the mean concentration gradient, i.e. $Pr = -2\overline{u'_i c'} \cdot \frac{\partial C}{\partial x_i} \propto \frac{\partial C}{\partial x_i}$ (see, e.g. Wang et al. (2009)). Therefore, as a necessary condition, locations where the mean concen-

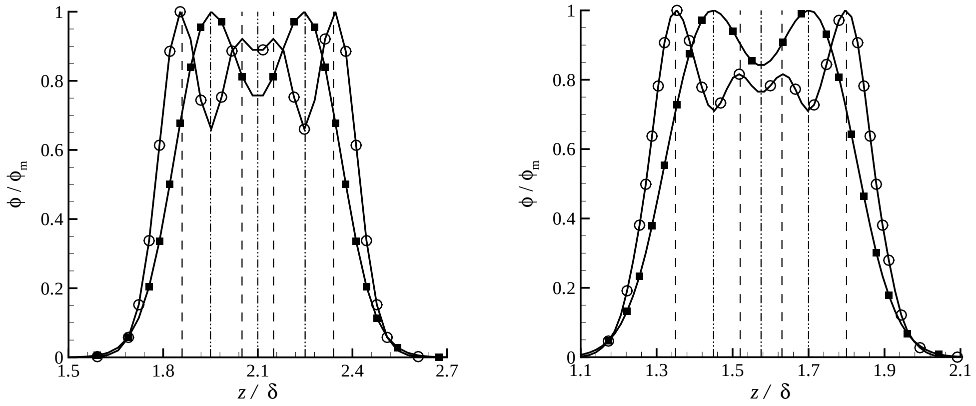

(a) Case 3 at $x/\delta = 2$

(b) Case 7 at $x/\delta = 2$

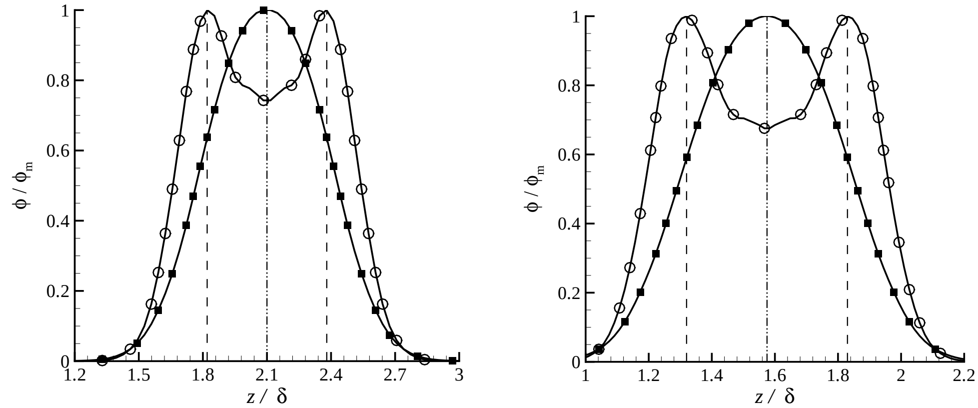

(c) Case 3 at $x/\delta = 4$

(d) Case 7 at $x/\delta = 4$

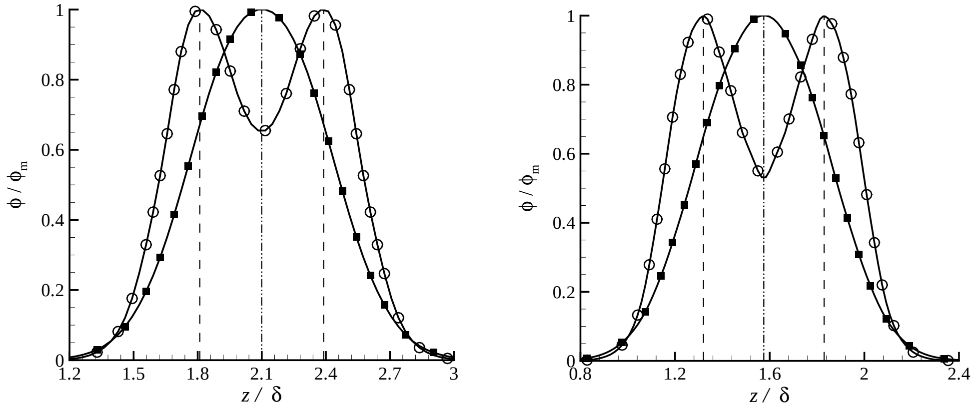

(e) Case 3 at $x/\delta = 6$

(f) Case 7 at $x/\delta = 6$

Figure 3.10: Lateral profiles of the total mean concentration C_T (■) and the variance of concentration fluctuations of the total plume $\overline{c_T'^2}$ (○). Straight vertical dashed and dash-dot-dotted lines indicate the locations of the local maxima of the absolute total mean concentration gradient and the locations of the local extrema of the mean concentration profile, respectively. Symbol ϕ represents either C_T or $\overline{c_T'^2}$.

tration gradient is zero (corresponding to local extrema of the mean concentration profile) can be also potentially the locations for local minima of the variance (since these locations correspond to locations of minimum variance production rate). On the other hand, because the production term functions as a source for the concentration variance, a large absolute value in the local mean concentration gradient tends to increase the local production rate, which in turn leads to an increase in the value of concentration variance. As such, locations where the absolute mean concentration gradient is maximum can be also potentially the locations for local maxima of the concentration variance. Figure 3.10 compares the lateral profiles of the mean (C_T) and variance ($\overline{c_T'^2}$) of the total plume at the source height ($y_s^+ = 5$) for cases 3 and 7 at three downstream locations. All profiles have been non-dimensionalized using their maximum values. As expected, at all downstream locations, the extrema locations in the C_T profile coincide with the locations associated with the local minima in $\overline{c_T'^2}$, and the locations of maximum absolute gradient of C_T coincide with the locations of the local maxima in $\overline{c_T'^2}$. Similar behavior is also observed for the other test cases at source height. This relationship between the mean and the variance of the concentration is also observed and investigated by Karnik and Tavoularis (1989) for a single plume dispersion in a uniformly sheared, nearly homogeneous turbulent flow. They found that at locations far downstream of the source, where the ratio of the streamwise velocity lengthscale to the half-width of the mean plume (which measures the strength of the plume meandering) is small, local conditions prevail and the concentration variance is nearly proportional to the local value of the mean concentration gradient. This is consistent with the above discussion and the results shown in figure 3.10 for the total plume.

The phenomenon of the appearance, disappearance and subsequent reappearance of the off-axis peaks in the concentration variance profiles with respect to the downstream location from the source is well established in the literature for single-source (Stapountzis et al., 1986; Karnik and Tavoularis, 1989) and dual-source dispersion

(Warhaft, 1984; Costa-Patry and Mydlarski, 2008) problems. In order to provide a better insight into this phenomenon, the effect of the wall distance on the concentration variance profile is studied in the remainder of this section. Figure 3.11 shows the spanwise profiles of the non-dimensionalized variance of concentration fluctuations of the total plume for cases 3 and 7 at $x/\delta = 6$ for different values of y^+. As is clear from figure 3.11(a), the spanwise profile of $\overline{c_T'^2}/\overline{c_{T,m}'^2}$ exhibits a distinct dual-peak pattern at lower elevations for $5 \leq y^+ \leq 15$. As the vertical distance from the wall increases, the dual-peak pattern vanishes around $y^+ = 50$ but reappears as the value of y^+ continues to increase (for $y^+ \geq 80$). By comparing figures 3.11(a) and (b), it is clear that this interesting dual-single-dual-peak pattern transitions with increasing elevation is common to both case 3 (for $Re_\tau = 180$) and case 7 (for $Re_\tau = 395$), albeit these pattern transitions occur at higher y^+ values in case 7 than in case 3.

Interestingly, the current observation of the dual-single-dual-peak transitions in the concentration variance profiles with increasing wall-normal distance from the bottom boundary at a fixed downstream distance is analogous to that described by Stapountzis et al. (1986) and Karnik and Tavoularis (1989) with respect to the downstream distance from the source at a fixed wall-normal distance. A similar interpretation can be used to explain the dual-single-dual-peak transitions with increasing height above the bottom wall at a fixed downstream location. Stapountzis et al. (1986) and Karnik and Tavoularis (1989) attributed the phenomenon of dual-single-dual-peak pattern transitions in the evolution of concentration variance profiles with increasing downstream distance from the source to the degree of meandering motions in the plume. These researchers further indicated that the dual-single-peak transition near the source is caused by the enhanced meandering as the downstream distance from the source increases, and meandering is a major source of concentration fluctuations in the region near the source. As the plume grows further in width (relative to the integral scales of turbulence), the effects of the meandering diminish and the single-dual-peak transition in the concentration variance profiles occurs at further

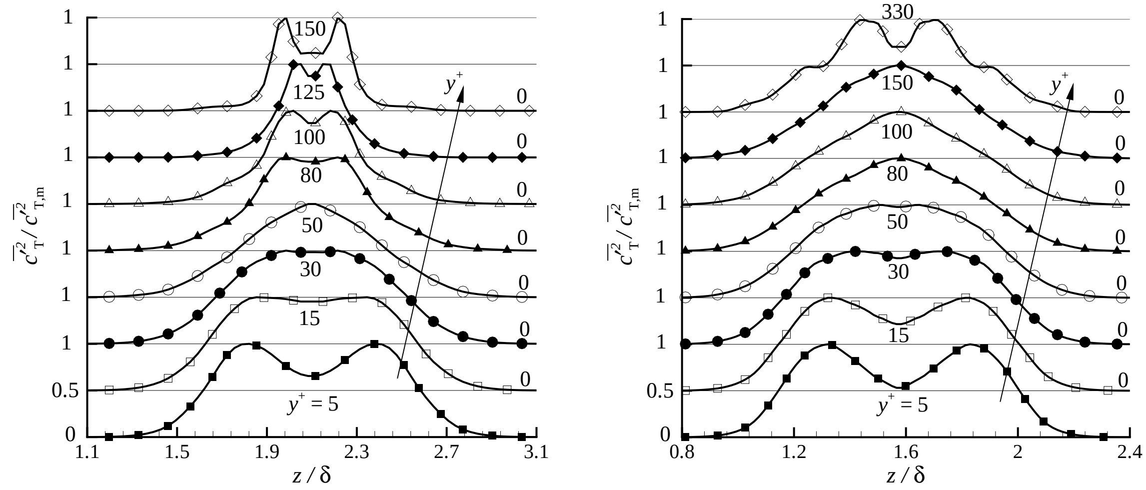

(a) Case 3 (b) Case 7

Figure 3.11: Lateral profiles of the variance of concentration fluctuations for different y^+ values at $x/\delta = 6$. Recall again that the source is located at $y^+ = 5$. The arrow points to the increasing direction of y^+.

downstream distances from the source.

For a given downstream location from the source, as the vertical distance from the wall increases, the size of the most energetic eddies of turbulence increases, and consequently, the meandering effect enhances and becomes the dominant source of concentration fluctuations. Then, the concentration fluctuations can be transported to locations of maximum absolute mean concentration gradients by turbulent eddies from the regions with zero or small mean concentration gradients, or vice versa. This mechanism "smears out" the local maxima and minima of the variance, leading to a single-peak pattern in the concentration variance profile. This explains the first transition from a dual- to a single-peak pattern profile, occurring within range $30 < y^+ \leq 50$ for $Re_\tau = 180$ (case 3) and within range $50 < y^+ \leq 80$ for $Re_\tau = 395$ (case 7). The second transition from a single- to a dual-peak pattern profile takes place at a higher elevation close to the free surface (located at $y^+ = 180$ and 395 for cases 3 and 7, respectively) of the open channel. As the free surface is approached, the upward-downwind distance from the point sources increases significantly, and both concentration and concentration variance levels drop significantly. These factors further lead to reduction in meandering effects and reemergence of the dual-peak pattern in the lateral profiles of the total concentration variance.

3.3.4 Cross Correlation Coefficient

The non-dimensionalized form of the scalar covariance $\overline{c'_A c'_B}$ represents a cross correlation of the two plumes, defined as

$$\rho^{[1|1]} = \frac{\overline{c'_A c'_B}}{(\overline{c'^2_A}\,\overline{c'^2_B})^{1/2}} = \frac{\overline{c'^2_T} - \overline{c'^2_A} - \overline{c'^2_B}}{2(\overline{c'^2_A}\,\overline{c'^2_B})^{1/2}} \quad . \tag{3.7}$$

Equivalently, $\rho^{[1|1]}$ can be expressed as

$$\rho^{[1|1]} = \frac{\overline{c_A c_B} - C_A C_B}{(\overline{c'^2_A}\,\overline{c'^2_B})^{1/2}} \quad . \tag{3.8}$$

According to Costa-Patry and Mydlarski (2008), the cross correlation $\rho^{[1|1]}$ reflects the quality of mixing while the scalar covariance reflects the total amount of mixing.

The streamwise variation of the cross correlation at the midpoint between the two plumes at the source height for cases 1–8 is shown using linear and semi-logarithmic scales in figures 3.12(a) and (b), respectively. The Reynolds number effects on the value of $\rho^{[1|1]}$ can be ascertained if cases with a similar source separation distance are compared (but different Reynolds numbers). By comparing cases 1 with 5, 2 with 6, 3 with 7, and 4 with 8, it becomes clear that the effect of Reynolds number on the streamwise variation of $\rho^{[1|1]}$ is insignificant (at least over the limited Reynolds number range in this research). Meanwhile, it is evident that the source separation distance has a significant impact on the streamwise distribution of $\rho^{[1|1]}$. Following the lead of Warhaft (1984) and Costa-Patry and Mydlarski (2008), the streamwise evolution of $\rho^{[1|1]}$ at the midspan between the two plumes can be generally categorized into the following four stages of development:

- **First stage** (zero interference, $\rho^{[1|1]} \approx 0$)

Very close to the source, there is no interaction between the two plumes. In other words, the width of the mean plume $2\Sigma_z$ and the width of the instantaneous plume $2\Sigma_r$ are smaller than the source separation distance d (i.e., $2\Sigma_z < d$ and $2\Sigma_r < d$) and the location at the midpoint between the two plumes is never exposed to both plumes simultaneously with the consequence that $\overline{c_A c_B} = 0$ and $C_A C_B = 0$. As a result, $\rho^{[1|1]}$ is identically zero in the region immediately downstream of the source. As shown in figure 3.12(b), this conclusion holds strictly for cases 4 and 8, whose source separation distances are the largest among all the test cases. The downstream extent of this stage reduces as the source separation distance d decreases. As such, for cases with smaller source separation distances (i.e., for cases 1, 2, 5 and 7), this stage (with $\rho^{[1|1]} \approx 0$) cannot be observed as the mean plumes overlap almost immediately after the scalar is released from the two sources.

- **Second stage** (destructive interference, $\rho^{[1|1]} < 0$)

As the downstream distance from the sources increases, the widths of the mean and instantaneous single plume exceed[3] the source separation distance d. In this stage, $\overline{c_A c_B} < C_A C_B$ and therefore, $\rho^{[1|1]}$ is negatively valued (cf. equation 3.8). The physical mechanism can be explained as follows. In the second stage and for small meandering motions, a relatively large eddy can transport a concentration "patch" from one plume to the other, causing the concentration to decrease in one plume while simultaneously increasing it in the other. However for strong meandering motions, Warhaft (1984) and Costa-Patry and Mydlarski (2008) attributed the negative cross correlation to the physical mechanism whereby a large eddy can move one plume off the measurement location while simultaneously moving the other plume onto the location. In both scenarios, the cross correlation value $\rho^{[1|1]}$ is negative at the measurement location.

From figure 3.12, it is observed that $\rho^{[1|1]}$ reaches its minimum value (a negatively

---

[3] The width of the mean plume exceeds the source separation distance at an earlier downstream position than does the instantaneous plume, because the mean plume width is always larger than or equal to the instantaneous plume width.

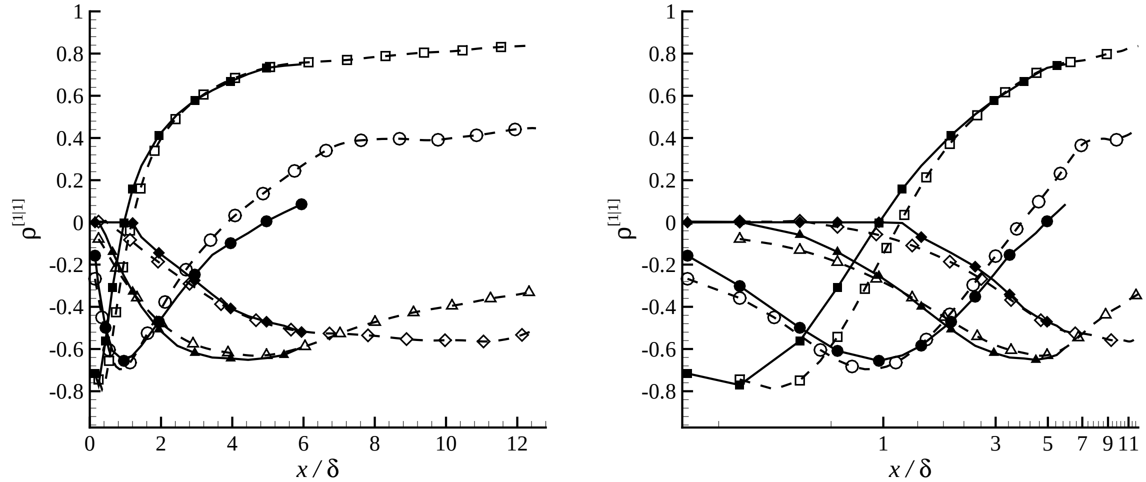

(a) Linear-linear

(b) Log-linear

Figure 3.12: Streamwise variation of the cross correlation $\rho^{[1|1]}$ in the midplane along the spanwise direction between the plumes at source height. Cases 1 (□), 2 (○), 3 (△), 4 (◇), 5 (■), 6 (●), 7 (▲), and 8 (♦).

valued trough) during this stage, and then increases towards a positive value with increasing distance from the source. Furthermore, it is clear that the smaller the source separation distance is, the shorter is the streamwise extent of this stage and the larger (in absolute magnitude) is the negative cross correlation between the two plumes. Indeed, as shown in figure 3.12, for cases 1 and 5 (for which the source separation is the smallest), the negatively valued trough of $\rho^{[1|1]}$ is the sharpest and the largest (in absolute magnitude), resulting in the shortest destructive interference range among all the test cases.

- **Third stage** (constructive interference, $\rho^{[1|1]} \geq 0$)

It is well-known (see, e.g. Costa-Patry and Mydlarski (2008)) that meandering of the plume and internal turbulent mixing are the two mechanisms which causes $\overline{c_A c_B} \geq C_A C_B$ (or equivalently, $\rho^{[1|1]} \geq 0$). However, from the previous analysis, it has been demonstrated that plume meandering effects are negligible over the downstream region for $x/\delta > 1.5$ and 0.6 at $Re_\tau = 180$ and 395, respectively. The third stage in the development of the cross correlation of all test cases occurs in this downstream region of the source. Therefore, the cross correlation in this stage of development mainly arises from the internal turbulent mixing of the two plumes which depends on a complicated physical process involving the stretching and folding of contaminant elements along with turbulent motions. When a blob of tracer is injected into a turbulent flow, it quickly deforms into thin folded strands and sheets. Turbulent fluid motions that repeatedly stretch and fold the contaminant elements serve also to increase the contact area for inter-diffusion and, hence, to enhance the molecular mixing, and to homogenize the plume concentration as the large spatial concentration gradients that are generated by the turbulent stirring are rapidly smeared out by molecular diffusion (Yee et al., 2003). This micromixing of the scalars from the two plumes makes a dominant contribution to the constructive interference of the two plumes in this stage. Specifically, $\overline{c_A c_B} \geq C_A C_B$ holds, and therefore, according to equation 3.8, the cross correlation is positive (i.e., $\rho^{[1|1]} \geq 0$). Furthermore, as the source separation distance decreases, the correlation between the two instantaneous plumes ($\overline{c_A c_B}$) in this stage of development increases drastically, leading to a fast growth in the value of $\rho^{[1|1]}$ with increasing downwind distance. As shown in figure 3.12, this trend in the streamwise development of $\rho^{[1|1]}$ is the most strongly expressed for cases 1 and 5 (the source separation distances are the smallest among all test cases, see table 3.1). However, for cases with larger source separation distances (such as cases 3, 4, 7 and 8), the increase in $\rho^{[1|1]}$ towards unity cannot be fully captured owing to the limited downwind extent in the current simulations.

- **Fourth stage** (complete mixing, $\rho^{[1|1]} \approx 1$)

In this final stage of development, the source separation distance is negligible in comparison with the long downstream distance from the sources. As such, the two plumes are completely mixed (i.e., $\rho^{[1|1]} \to 1$) and the total plume behaves as if it comes from a single source. A comparison of the profiles exhibited in figure 3.12 indicates that the cases with a smaller source separation distance tend to reach this complete mixing state earlier than the cases with a larger source separation distance.

Such an asymptotic behavior is captured in cases 1 and 5, and partially captured in cases 2 and 6. However, in order to reproduce this complete mixing stage in cases 3, 4, 7 and 8, a much longer downwind fetch would be required in the simulations.

It is seen that $\rho^{[1|1]}$ at source height is only a function of source separation distance d and the measurement locations. This is similar to the observation of Warhaft (1984) in grid turbulence. Generally, $\rho^{[1|1]}$ reaches the complete mixing state faster in this study than in the case of grid turbulence of Warhaft (1984). This can be attributed to the highly-sheared region near the wall (associated as such with hairpin structures and streak structures, etc.) where small-scale eddies are generated to increase the internal mixing in the plume. In addition to this, Costa-Patry and Mydlarski (2008) noted that by limiting both the growth and meandering of the plume while simultaneously increasing the turbulence kinetic energy, the presence of the wall will lead necessarily to an increased internal plume mixing.

Figures 3.13(a)-(c) compare the lateral profiles of $\rho^{[1|1]}$ for the eight different cases at the source height for three different downwind distances. The Reynolds number effects on the lateral profile of $\rho^{[1|1]}$ are also directly compared in this figure. Owing to the relatively long streamwise domain size used in cases 1–4 (for $Re_\tau = 180$), the influence of the source separation d on the profile of $\rho^{[1|1]}$ is singled out in the fully turbulent diffusive range (for $x/\delta = 12$), and the results are displayed in figure 3.13(d). To further facilitate the comparative study, the lateral coordinate has been shifted to the midpoint location between the two plumes (z_{mid}) and then non-dimensionalized using the mean plume dispersion. Consistent with the previous analysis of the streamwise profiles of $\rho^{[1|1]}$ given in figure 3.12, figure 3.13 also shows clearly that the dominant factor that determines the shape of the lateral profile of $\rho^{[1|1]}$ is the source separation distance d. By comparing cases 1 with 5, 2 with 6, 3 with 7, and 4 with 8, the effect of Reynolds number on the lateral profiles of $\rho^{[1|1]}$ can be observed, which appears to be much smaller than that of the source separation distance d.

The streamwise variation in the shape of the lateral profiles of $\rho^{[1|1]}$ also illustrates

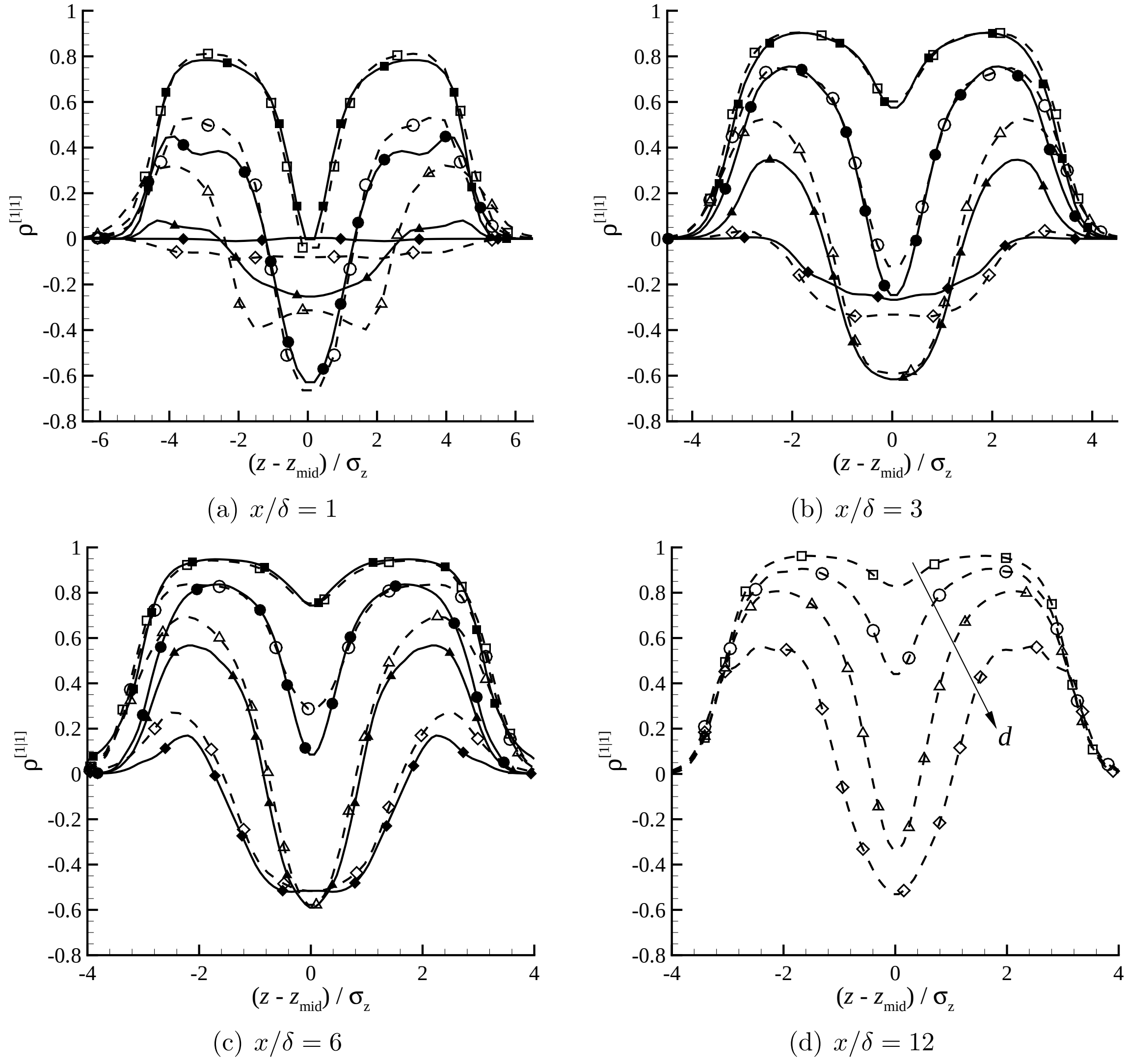

(a) $x/\delta = 1$ (b) $x/\delta = 3$ (c) $x/\delta = 6$ (d) $x/\delta = 12$

Figure 3.13: Lateral profiles of the cross correlation $\rho^{[1|1]}$ at source height. Cases 1 (□), 2 (○), 3 (△), 4 (◇), 5 (■), 6 (●), 7 (▲), and 8 (◆).

the four stages in its evolution. In the first stage, the shape of the profile is flat with a zero value, because there is no interaction between the two plumes. In the second stage, a M-shape profile, with a negative minimum value, begins to form. The M-shape profile has the minimum value of $\rho^{[1|1]}$ located midway between the two plumes and the maximum values are found at the edges of the plumes. As discussed earlier, the minimum value at the midpoint between the two plumes is due to the fact that a large eddy (relative to the plume width) at this location can cause the concentration contributed by one plume to increase and that contributed by the other plume to decrease. For sources that are close enough together, the maximum values in $\rho^{[1|1]}$ on both sides of the centerline (where the plume intermittency is large) arise from the fact that at these locations a large eddy can occasionally transport both plumes (in case of strong meandering) or bring together a patch of concentration from each of the plumes (in case of weak meandering), causing the two concentrations to either increase or decrease simultaneously. A similar M-shaped profile of $\rho^{[1|1]}$ was also observed by Warhaft (1984) in grid turbulence, Tong and Warhaft (1995) in a turbulent jet and Costa-Patry and Mydlarski (2008) in a turbulent plane-channel flow. Due to the noise sensitivity of their measurements, these investigators were unable to demonstrate conclusively that the value of $\rho^{[1|1]}$ approaches zero at the extreme lateral fringes of the plume. However, this is clearly demonstrated in figure 3.13. At the third stage in the development, the minimum of the M-shaped profile becomes positive and the profile begins to approach a constant value of unity (approximately or better), owing to the internal turbulent mixing of the two plumes. Finally at the fourth stage of development, a flat profile with a value of unity forms signaling that the scalars in the two overlapping plumes are perfectly well mixed.

3.3.5 Concentration Co-spectrum and Coherency Spectrum

The quantities studied so far contain no information about the scales of mixing of the two plumes. However, mixing of the two plumes is a multi-scale phenomenon, as the turbulent motions responsible for stirring act primarily on large and intermediate scales, with the molecular diffusion smearing out and completing the mixing at the smallest scales. Therefore, in order to improve the understanding of the physics of mixing of two plumes, the scales of the concentration fields that contribute to the turbulent stirring and molecular mixing need to be investigated. The information about the scales of mixing can be quantified using the so-called co-spectrum and coherency spectrum of the two plumes. Following the approach of Tong and Warhaft (1995) and Costa-Patry and Mydlarski (2008), the co-spectrum is defined as

$$Co_{c'_A c'_B}(f_s) = \left(E_{c'_T c'_T}(f_s) - E_{c'_A c'_A}(f_s) - E_{c'_B c'_B}(f_s)\right)/2 \quad , \tag{3.9}$$

where $E_{c'_A c'_A}(f_s)$, $E_{c'_B c'_B}(f_s)$ and $E_{c'_T c'_T}(f_s)$ are the concentration power spectra for plume A, plume B, and total plume, respectively. The integral of co-spectrum $(Co_{c'_A c'_B}(f_s)/(\overline{c'^2_A}\ \overline{c'^2_B})^{1/2})$ is the cross correlation coefficient $\rho^{[1|1]}$, i.e.

$$\rho^{[1|1]} = \int_{-\infty}^{\infty} Co_{c'_A c'_B}(f_s)/(\overline{c'^2_A}\ \overline{c'^2_B})^{1/2} df_s \quad . \tag{3.10}$$

The coherency spectrum $\rho_f^{[1|1]}$ is defined as

$$\rho_f^{[1|1]} = \frac{Co_{c'_A c'_B}(f_s)}{\left(E_{c'_A c'_A}(f_s) E_{c'_B c'_B}(f_s)\right)^{1/2}} \quad , \tag{3.11}$$

which describes the cross correlation coefficient in the frequency space. The pre-multiplied co-spectrum and the coherency spectrum obtained at the midpoint between the two plumes at source height for cases 1 and 5 are shown in figures 3.14 and 3.15, respectively. In order to investigate the streamwise evolutions of the pre-multiplied co-spectrum and coherency spectrum, several downstream locations (with different x/δ values) are considered in the comparative study. The frequency f_s in these figures has been non-dimensionalized using u_τ and δ, which leads to the Strouhal number defined as $f^* = f_s\delta/u_\tau$. In order to facilitate the discussion, the frequency corresponding to the Kolmogorov scale of the velocity field is shown using a straight vertical dashed line in figure 3.15. Furthermore, in order to identify the most energetic eddy scale and compare the local plume scale with it, the pre-multiplied energy spectrum of the spanwise velocity fluctuations (i.e., $f^* E_{w'w'}(f^*)$) is plotted using a long dashed curve in figure 3.15.

By definition, the co-spectrum $Co_{c'_A c'_B}$ and coherency spectrum $\rho_f^{[1|1]}$ studied here are closely related to the cross correlation coefficient $\rho^{[1|1]}$, with a difference that $Co_{c'_A c'_B}$ and $\rho_f^{[1|1]}$ provide explicit information on the interference of the two plumes in

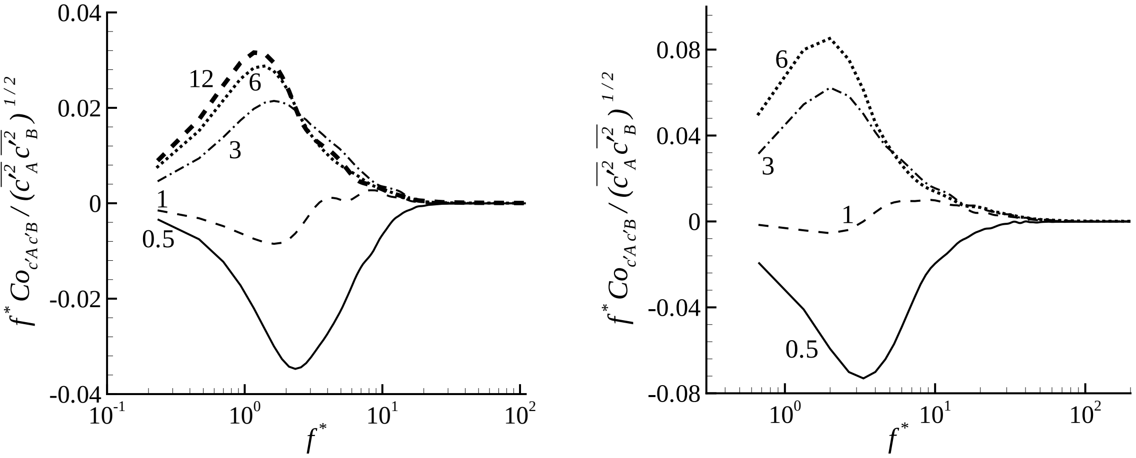

(a) Case 1 (small source separation, $Re_\tau = 180$)

(b) Case 5 (small source separation, $Re_\tau = 395$)

Figure 3.14: The pre-multiplied co-spectrum of two plumes for cases 1 and 5 obtained at the midpoint between the two plumes and at source height, for $x/\delta = 0.5$ (solid line), 1 (thin dashed line), 3 (dash-dotted line), 6 (dotted line) and 12 (thick dashed line).

the frequency space, whereas $\rho^{[1|1]}$ provides similar information in physical space. As such, it is useful to connect the physical features shown in figures 3.14 and 3.15 (in the frequency space) to those shown in figures 3.12 and 3.13 (in the physical space). Here, only $Co_{c'_A c'_B}$ and $\rho_f^{[1|1]}$ for cases 1 and 5 are presented, because these two cases (as shown previously in figure 3.12) cover the widest range of values for $\rho^{[1|1]}$ among all test cases. Also, except for the first stage, all other three stages in the development of the cross correlation are well captured by these two cases. The values for $Co_{c'_A c'_B}$ and $\rho_f^{[1|1]}$ in the first stage can be determined as $Co_{c'_A c'_B} = 0$ and $\rho_f^{[1|1]} = 0$, simply because there is no interference between the two plumes.

As shown previously in figures 3.12 and 3.13, the streamwise variation of the cross correlation is less sensitive to the Reynolds number than the source separation distance. A similar conclusion can be made for the streamwise variation of the pre-multiplied co-spectrum and the coherency spectrum by comparing figures 3.14(a) with 3.14(b) and 3.15(a) with 3.15(b). Furthermore, the streamwise evolution of the pre-multiplied co-spectrum and the coherency spectrum follows the streamwise evolution

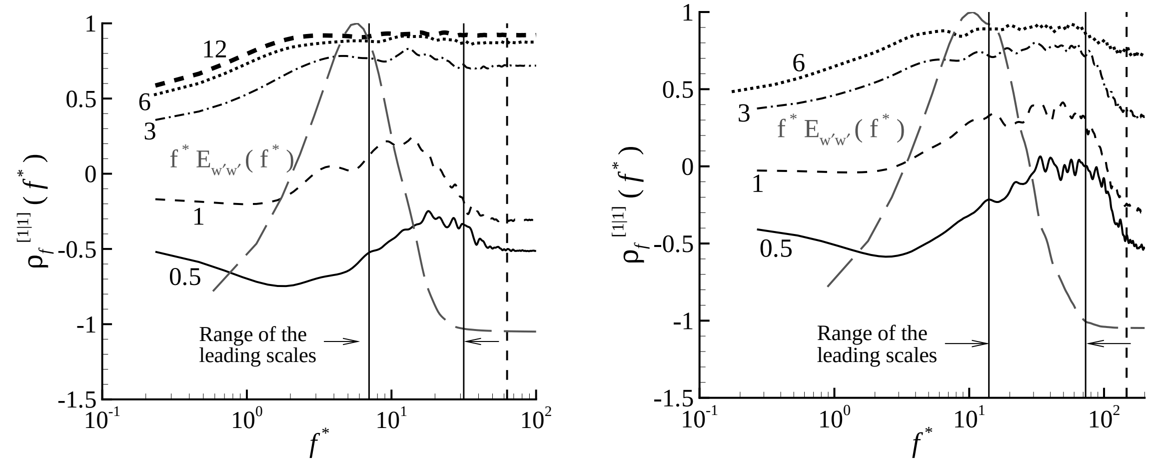

(a) Case 1 (small source separation, $Re_\tau = 180$)

(b) Case 5 (small source separation, $Re_\tau = 395$)

Figure 3.15: The coherency spectrum $\rho_f^{[1|1]}$ of two plumes for cases 1 and 5 obtained at the midpoint between the two plumes and at source height, for $x/\delta = 0.5$ (thin solid line), 1 (dashed line), 3 (dash-dotted line), 6 (dotted line) and 12 (thick dashed line). The straight vertical dashed line shows the frequency corresponding to the Kolmogorov scale. The long dashed curve shows the pre-multiplied energy spectrum $f^* E_{w'w'}$ of velocity fluctuations in the spanwise direction. The pre-multiplied energy spectrum $f^* E_{w'w'}$ is used here for identifying the frequency corresponding to the most energetic eddies (through its peak location), and its magnitude has been re-scaled arbitrarily in order to fit in the figure panel.

of the cross correlation and the aforementioned four stages in the development for the cross correlation can also be observed from the pre-multiplied co-spectrum and coherency spectrum.

In the first stage, because the measurement location is exposed to clean fluid most of the time, it is expected that the pre-multiplied co-spectrum exhibit values near zero at all scales. This is the case for a large source separation distance and for downstream locations close to the source. In the second stage of development, the two plumes meander in opposite directions as the result of the large-scale turbulent stirring. As is explained in subsection 3.3.4, this produces a negative spectral peak for the pre-multiplied co-spectrum at large scales (low frequencies). The frequency of this peak can be interpreted as the frequency of the most energetic scales of the mixing of the two plumes. The value of the cross correlation is mainly determined by these scales. Because the size of the plumes increases as the downstream distance from the sources increases, the frequency of the peak reduces. Indeed, as shown in figures 3.14(a) and (b), the peak frequency for $x/\delta = 1$ is lower than that for $x/d = 0.5$ in both cases 1 and 5.

In the third stage, the internal turbulent stirring and molecular mixing of the two plumes is expected to give rise to a positive spectral peak in the pre-multiplied co-spectrum. As the downstream distance from the sources increases, the value of this spectral peak increases and its frequency drops (indicating the scales of mixing become larger). This physical feature is evident for $x/\delta \geq 3$ in figures 3.14(a) and (b). In the fourth stage where the cross correlation reaches its maximum value of unity, it can be anticipated that the pre-multiplied co-spectrum reaches its asymptotic form and does not change further with increasing downstream distance from the source. Indeed, as shown in figure 3.14(a), as the downstream distance x/δ increases from 6 to 12, the profile of the pre-multiplied co-spectrum hardly changes.

From the above analysis, it is seen that the most energetic scales of the mixing of the two plumes, which mainly determine the cross correlation value, are generally associated with low frequencies (or, large scales). This is consistent with the observations of Tong and Warhaft (1995) and Costa-Patry and Mydlarski (2008). A physical explanation to this phenomenon is that large-scale eddies contain most of the turbulence energy, and consequently, the co-spectrum and cross correlation values are mainly determined by these large-scale eddy motions.

Figure 3.15 shows the streamwise variation of the coherency spectrum $\rho_f^{[1|1]}$, which is closely related to the cross correlation displayed in figure 3.12. However, it can be seen that at some small scales the coherency spectrum develops faster than at other scales. These small scales are two to ten times the Kolmogorov scale (shown using vertical dashed line in the figure) and they are called the “leading scales”, because the value of $\rho_f^{[1|1]}$ is the largest at these scales. As shown in the figure, that the leading scales can reach the asymptotic value of unity faster than any other scales. A careful perusal of the figure indicates that the frequency of the leading scales is either higher than (or close to) the frequency of the most energetic eddies of turbulence (indicated by peak frequency of the pre-multiplied energy spectrum $f^* E_{w'w'}(f^*)$ in the figure). This means that the rate of turbulent mixing of the two plumes becomes more efficient (faster) for those scales that are several times larger than the Kolmogorov scale and extending up to the scale of the most energetic eddies of the turbulent flow. In contrast, Tong and Warhaft (1995) and Costa-Patry and Mydlarski (2008) inferred from their analysis that the rate of mixing is fastest at the largest scales. Costa-Patry and Mydlarski (2008) attributed this to the fact that turbulence production is essentially a large-scale phenomenon, such that its effects occur first at the largest scales and these effects will be influenced by smaller scales only after a sufficient time has passed for the mixing effects to cascade down from larger to smaller scales. The reason the rate of mixing is the fastest at the largest scales in Tong and Warhaft (1995) and Costa-Patry and Mydlarski (2008) is that the plume meandering effect is dominant in these studies, which first takes place at the largest scales and subsequently is transferred down to the smaller scales. However, for the ground-level sources studied here, the plume meandering effect is negligible. Instead, the internal turbulent mixing is dominant, which first occurs at the smaller leading scales with their effects transferred subsequently to the other scales.

3.4 Chapter Summary

The interference of the plumes released from two near-ground point sources into an open-channel flow at two Reynolds numbers is studied using DNS. The first- and second-order statistics of the velocity and concentration fields have been analyzed. In order to investigate the effects of Reynolds number and source separation distance on the mixing of two plumes, the cross correlation function, co-spectra and coherency spectra of the two concentration fields are examined. Because the transport equation for the instantaneous concentration field is linear, the mean concentration (first-order concentration moment) of the total plume can be obtained as a sum of the mean concentration of each plume. However, other concentration moments (e.g., second-order and higher) are not linearly superposable and the interference of the two plumes should be taken into account for calculations of higher-order concentration moments of the total plume.

The streamwise variation of the cross correlation function ($\rho^{[1|1]}$) at the midpoint between the two plumes reveals that there are four stages in the mixing process, including (1) the zero interference stage where $\rho^{[1|1]} = 0$, (2) destructive interference stage where $\rho^{[1|1]} < 0$, (3) constructive interference stage where $\rho^{[1|1]} \geq 0$, and (4) complete mixing state where $\rho^{[1|1]} \rightarrow 1$. At the source height, the streamwise evolution of the cross correlation $\rho^{[1|1]}$ is insensitive to the Reynolds number but highly sensitive to the source separation distance d. For a small source separation case, as the downstream distance from the sources increases, the cross correlation first decreases and then it increases towards the asymptotic value of unity. However, for a large source separation case, the streamwise evolution of the cross correlation takes a much longer downwind fetch.

The results of the pre-multiplied co-spectrum ($f^* Co_{c'_A c'_B}$) and the coherency spectrum ($\rho_f^{[1|1]}$) obtained at the midpoint between the two plumes at source height for different downstream locations can provide deeper insights into plume mixing at different scales. In the first stage (zero interference stage), because the midpoint between the two plumes is exposed to clean fluid most of the time, the pre-multiplied co-spectrum is zero at all scales. In the second stage (destructive interference stage), due to large-scale turbulent motions, patches of concentration are transported from one plume to the other, resulting in a negatively valued peak in the pre-multiplied co-spectrum at low frequencies (corresponding to large scales). In the third stage (constructive interference stage), the internal turbulent stirring and molecular mixing of the two plumes give rise to a positive spectral peak in the pre-multiplied co-spectrum. As the downstream distance increases, the magnitude of this spectral peak increases monotonically as its frequency decreases (correspondingly, the scale of mixing becomes larger). In the fourth stage (complete mixing state), the cross correlation $\rho^{[1|1]}$ reaches its maximum value of unity, and subsequently, the pre-multiplied co-spectrum reaches its asymptotic form.

It is observed that there is a range of 'leading scales' which correspond to the largest values of $\rho_f^{[1|1]}$ in the coherency spectrum. These scales are typically two to ten times larger than the Kolmogorov scale but are smaller than or comparable to the scale of the most energetic eddies of turbulence. Within the range of leading scales, the mixing of two plumes is the fastest and $\rho_f^{[1|1]}$ approaches the asymptotic value of unity quicker than at any other scales.

In comparison to the studies of Warhaft (1984) in grid turbulence, Costa-Patry and Mydlarski (2008) in a turbulent plane-channel flow, and Tong and Warhaft (1995) in a turbulent jet, the following differences are identified.

- Large scale eddy motions provide the primarily contribution to plumes mixing in the studies of Warhaft (1984) and Costa-Patry and Mydlarski (2008). In contrast, the small scale internal turbulent mixing is dominant in plumes mixing of this study.
- $\rho^{[1|1]}$ reaches the asymptotic value of unity, faster in this study than in the case of grid turbulence of Warhaft (1984). This is attribute to the fact that the sources in this study are located at the highly-sheared region near the wall.
- Due to the limitations in the measurements, Warhaft (1984), Tong and Warhaft (1995), and Costa-Patry and Mydlarski (2008) were unable to observe that $\rho^{[1|1]}$ approaches zero at fringes of the plume, which is detected in this study.
- Because of large meandering motions, the rate of mixing is the fastest at the largest scales in the studies of Tong and Warhaft (1995) and Costa-Patry and Mydlarski (2008). However, for the ground-level sources studied here, the internal turbulent mixing is dominant and therefore, the mixing is the fastest at the smallest scales.

Chapter 4

Effect of Source Elevation on the Dispersion and Mixing of Plumes

4.1 Introduction

In chapter 3, the dispersion and mixing of two plumes released from two ground-level point sources in a turbulent open-channel flow have been studied. However, the dispersion and mixing of plumes released from elevated sources also represent an important topic in atmospheric sciences and environmental engineering. The atmospheric boundary layer is the lowest part of the atmosphere that is in contact with, and directly influenced by, the surface of the Earth. Its thickness is approximately 100 to 3000 meters and varies in both space and time. In a typical urban environment, the materials are released from a stack located at 10-50 meters above the ground into the atmospheric boundary layer. The source height in these types of application is approximately 0.3-50% of the boundary layer thickness. The lower and higher limits of this range corresponds to the release of materials into the atmospheric boundary layer from sources at the ground and elevated levels, respectively. In view of this, it is important to develop a deep understanding of the dispersion and mixing of plumes released from elevated sources in addition to ground-level sources.

Table 4.1: Summary of test cases. The near ground-level source (GLS) is located at $y_s^+ = 5$ and the elevated source (ES) is located at $y_s^+ = 40$.

Case	Source type	Source separation (d/δ)	Source size (σ_0/δ)
1	GLS	0.049	0.007
2	GLS	0.115	0.007
3	GLS	0.279	0.007
4	GLS	0.541	0.007
5	ES	0.049	0.008
6	ES	0.115	0.008
7	ES	0.279	0.008
8	ES	0.541	0.008

In this chapter, the effect of source elevation on the dispersion and mixing of two plumes released from two point sources in a turbulent open-channel flow is studied. The interference process of the two elevated plumes is compared with that of the ground-level plumes. Specifically, the concentration statistics, which include the mean and RMS concentrations, the cross correlation coefficient, the concentration co-spectrum and coherency spectrum, the concentration PDF, the concentration EDF and various higher-order concentration moments are examined.

4.2 Problem Description

The flow configuration in this chapter is identical to that used in chapter 3, and its geometry has been illustrated in figure 3.1. The dual plumes are released from two point sources into an open-channel flow with the Reynolds number set to $Re_\tau = 395$. The two sources are of equal strength and are located at a vertical distance of either $y_s^+ = 5$ (in the viscous sublayer) or $y_s^+ = 40$ (in the log-law region) from the lower (solid) wall, corresponding to a pair of near ground-level or elevated sources, respectively. The choice of these two elevations is related to the fact that the industrial sources (e.g., exhaust from vehicles and chimneys) are located either near the ground surface or in the lower portion of the atmospheric boundary layer (viz., surface layer). These two configurations allow us to study the effects of the wall on the interference of the concentration fields from the two point sources (each of size σ_0) in a neutrally-stratified wall-shear flow as a function of the source separation distance d in the spanwise direction. For each case of the ground-level and elevated releases, four different spanwise source separation distances d are investigated. The source separation and source size for the various test cases are summarized in table 4.1.

4.3 Results and Discussion

4.3.1 Mean Concentration Field

In this subsection, the mean concentration field for a single and the total plumes are presented and discussed.

4.3.1.1 Mean concentration of a single plume

The mean concentration in a dispersing passive plume released from a point source in grid turbulence assumes a Gaussian form in the spanwise direction (Uberoi and Corrsin, 1953; Townsend, 1954). Similarly, it is expected that spanwise profiles of the mean concentration of a plume released from either a ground-level or an elevated point source in a turbulent boundary layer also exhibit a Gaussian form. The horizontal mean concentration profile of a single plume at source height y_s can be fitted using a Gaussian distribution of the form:

$$C(x, y_s, z) = C_0(x, y_s)\text{exp}\left(-\frac{1}{2}(z - z_s)^2/\sigma_z^2\right) \quad , \tag{4.1}$$

where $C_0(x, y_s)$ is the plume centerline mean concentration at source height, z_s is the location of the source in the spanwise direction, and σ_z is the lateral mean plume dispersion. The lateral mean plume dispersion is the distance in the spanwise direction over which the mean concentration in the plume decreases to about 61% of its maximum value. The half width of the mean plume in the spanwise direction will be denoted by Σ_z, defined as the distance over which the mean concentration decreases to about 1% of its maximum value. For a Gaussian mean concentration profile, $\Sigma_z \approx 3\sigma_z$ as is shown in figure 3.5.

Figure 4.1 compares the streamwise development of the mean (absolute) and relative dispersion scales of a single plume released from near ground-level and elevated sources. The streamwise variation of the non-dimensionalized lateral mean plume dispersion σ_z/δ and the ratio of the lateral relative plume dispersion to the lateral absolute plume dispersion (viz., σ_r/σ_z) at source height are shown in figures 4.1(a) and (b), respectively. As is evident in figure 4.1(b), there are two stages in the streamwise evolution of the plume dispersion for the elevated source; namely, the turbulent convective regime where the meandering of the instantaneous plume provides the dominant contribution to the concentration fluctuations, and the turbulent diffusive regime where the internal mixing through eddy motions within the plume begin to dominate the concentration fluctuations. The turbulent convective regime can be defined as the downwind range where the meander ratio $M = \sigma_c^2/\sigma_r^2 \geq 1$ (or equivalently, $\sigma_r/\sigma_z \leq (1/2)^{1/2} \approx 0.7071$). Consequently, the turbulent diffusive regime can be defined as the downwind fetches where $M < 1$ (or equivalently, $\sigma_r/\sigma_z > (1/2)^{1/2} \approx 0.7071$).

For the elevated source, it is seen that the turbulent convective regime extends in the streamwise direction to about 2.2 times the boundary-layer height (i.e., $x/\delta = 2.2$, location marked using vertical dash-dot line in figure 4.1(b)), and the plume transitions to the turbulent diffusive regime beyond this location. Unlike the elevated-source release, the plume from the ground-source release only exhibits a turbulent diffusive regime of development as is shown in figure 4.1(b). This indicates that internal fluctuations are the dominant mechanism responsible for generating concentration fluctuations in the dispersing plume for the ground-level source release at all downwind fetches.

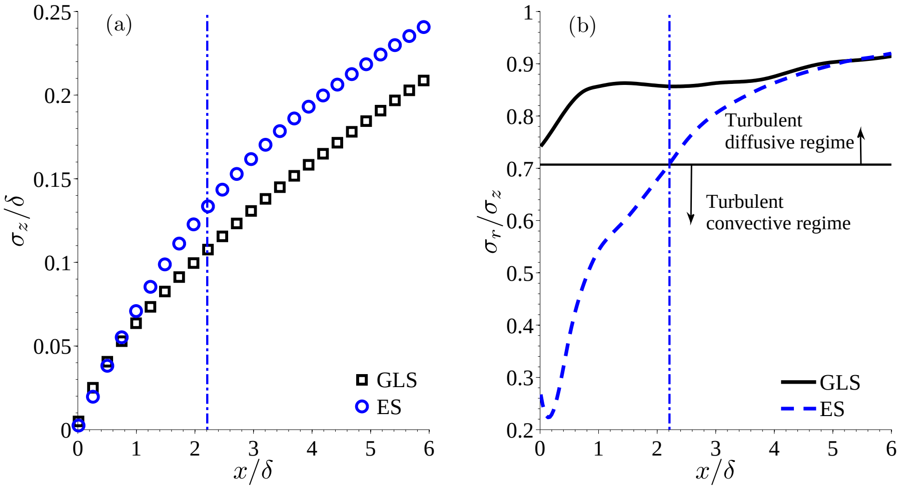

Figure 4.1: Streamwise development of a single plume. (a) The lateral mean (or absolute) plume dispersion σ_z scaled by the boundary-layer height δ and (b) the ratio of the lateral relative plume dispersion σ_r to the mean plume dispersion σ_z (for the ground-level and elevated sources) as a function of the non-dimensional downstream distance x/δ. The beginning of the turbulent diffusive range for the elevated source is demarcated using the vertical dot-dash line.

As it is discussed in chapter 3, in the turbulent convective regime for the plume from the elevated source, the width of the instantaneous plume is relatively small compared to the size of the most energetic turbulent eddies in the bulk flow. When the instantaneous plume width is comparable in size to that of the most energetic turbulent eddies, the development of the instantaneous plume transitions into the turbulent diffusive regime where the major contribution to the scalar fluctuations arises from the internal fluctuations (in-plume mixing processes) and the effects of plume meander become less and less important with increasing downwind fetch in this regime.

The above discussion for the plume growth of the elevated source can be further supported by comparing the size of the most energetic turbulent eddies in the flow with the width of the instantaneous plume at the beginning of the turbulent diffusive range. Figure 4.2(a) shows the velocity spectrum $E_{w'w'}(k_z)$ plotted against the wavenumber k_z. The velocity fluctuations used for the computation of this spectrum

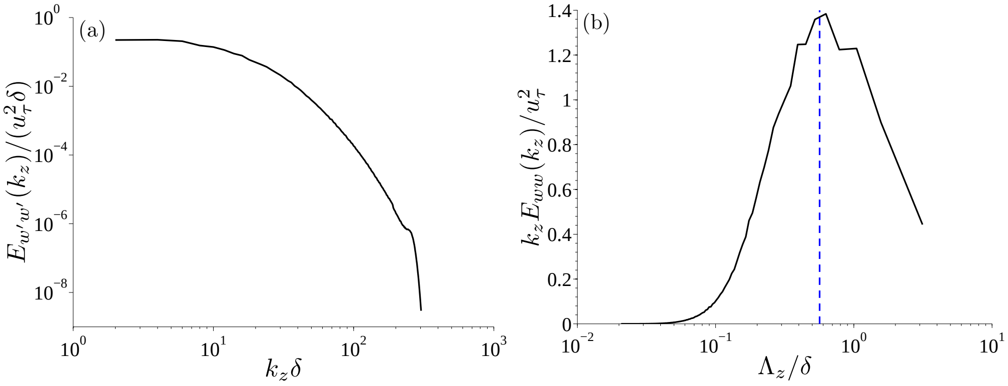

Figure 4.2: (a) Spanwise velocity spectrum plotted against the spanwise wavenumber and (b) pre-multiplied spanwise velocity spectrum plotted against the spanwise wavelength at $y^+ = 40$ (height of the elevated source). The full width of the instantaneous plume ($2\Sigma_r$) at the beginning of the turbulent diffusive range for the elevated source is indicated by the dashed vertical line.

were obtained at the elevated source height $y^+ = 40$. In order to clearly show the size of the most energetic eddies, it is more convenient to display the velocity spectrum pre-multiplied by the wavenumber (i.e., $k_zE_{w'w'}(k_z)$) plotted against the normalized spanwise wavelength $\Lambda_z/\delta = 2\pi/(k_z\delta)$. The wavelength corresponding to the spectral peak in this figure is associated with the size of the most energetic turbulent eddies in the flow. Also in this figure, the full width of the instantaneous plume at the beginning of the turbulent diffusive range for the elevated source (taken to be $2\Sigma_r = 6\sigma_r$ as defined in figure 3.5) is indicated using the dashed vertical line. As is evident from this figure, the width of the instantaneous plume at the beginning of the turbulent diffusive regime for the elevated source is comparable (approximately or better) to the size of the most energetic eddies in the flow.

The vertical mean concentration profile along the mean plume centerline in the horizontal direction ($z = z_s$) for a single ground-level source can be fitted using the following functional form (Fackrell and Robins, 1982):

$$C(x,y,z_s) = C_0(x,z_s)\text{exp}\left(-\frac{1}{2}(y/\sigma_y)^s\right) \quad , \tag{4.2}$$

where $C_0(x,z_s)$ is the maximum mean concentration along the centerline of the mean plume at ground level ($y = 0$), σ_y is the vertical mean plume dispersion and s is the power-law exponent. A least-squares fitting of the functional form of equation 4.2 to the DNS data for the vertical mean concentration profiles yielded a value for s of 1.5. In contrast, for a single elevated source (located at the lateral position $z = z_s$), a reflected Gaussian form (Fackrell and Robins, 1982) can be used to determine the vertical plume dispersion σ_y, viz.

$$C(x, y, z_s) \sim \exp\left(-\frac{1}{2}(y - y_s)^2/\sigma_y^2\right) + \exp\left(-\frac{1}{2}(y + y_s)^2/\sigma_y^2\right) \quad . \qquad (4.3)$$

Figure 4.3 shows the streamwise variation of the vertical mean plume spread σ_y for both the ground-level and elevated sources. It can be seen that for the ground-level source, the vertical mean plume spread is linear (viz., $\sigma_y \propto x$) over the range of downwind fetches studied. For the elevated source, the vertical spread in the mean plume is linear (approximately or better) up to a downwind distance from the source of about $x/\delta \approx 1$. After this range, there is a gradual transition[1] of the elevated plume form to a ground-level plume form. Indeed, as this transition occurs, the rate of the vertical mean plume spread for the elevated plume slows down (relative to that of the initial phase of development) and approaches a growth rate that is comparable to that observed for the ground-level plume.

Figure 4.4 shows the downstream development of the vertical profile of the mean concentration along the plume centerline for a ground-level and an elevated source. The vertical distance y has been non-dimensionalized by the corresponding vertical mean plume dispersion σ_y at the given downstream location. The figure shows that for the near ground-level source, the vertical mean concentration profiles at all downwind locations approach a self-preserving form. The transition of the elevated plume form to the ground-level plume form can be clearly seen in figure 4.4(b). It is evident that the vertical mean concentration profiles of the elevated source start to collapse on

---

[1] Transition of an elevated plume to a ground-level plume takes place when the bottom boundary of the plume begins to touch the lower (solid) wall. Eventually, at sufficient distances downwind of the elevated source, the vertical mean concentration profile in the plume approaches a self-preserving form similar to that observed for a ground-level plume.

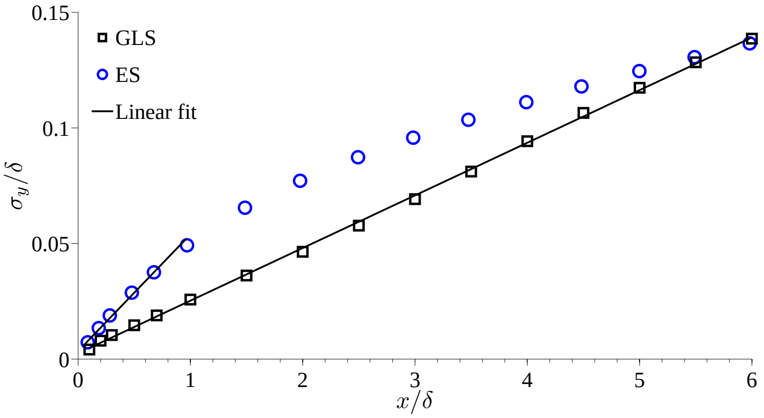

Figure 4.3: Streamwise variation of the vertical mean plume dispersion along the mean plume centerline for a ground-level and an elevated source.

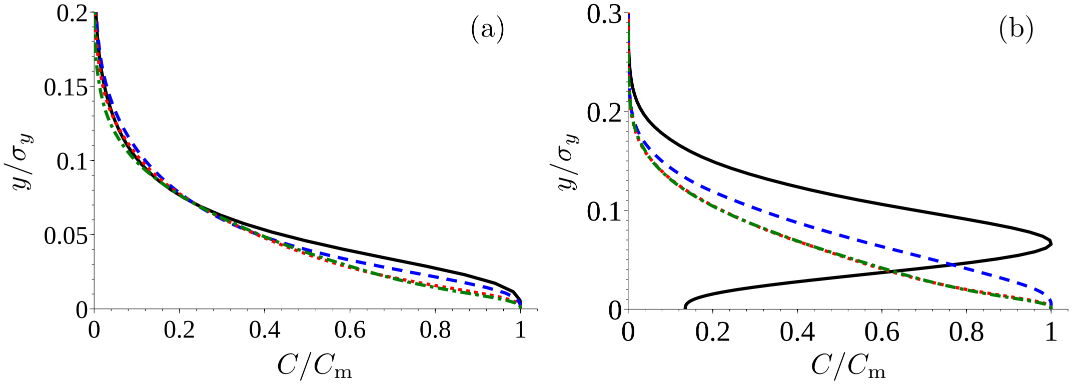

Figure 4.4: The vertical profiles of the mean concentration along the plume centerline for (a) a ground-level and (b) an elevated source at non-dimensionalized downwind fetches of $x/\delta = 1$ (solid line), 2 (dashed line), 4 (dotted line) and 6 (dash-dot line).

each other as the downwind distance from the source increases to $x/\delta = 4$ and 6. A further comparison of the vertical concentration profiles at these two downwind locations with those for the ground-level source shown in figure 4.4(a) confirms that the shape of these profiles for the elevated source is very similar to the corresponding self-preserving profiles for the ground-level source. This indicates that in a region far downstream of the source, the effect of source elevation on the mean plume dispersion becomes much reduced.

4.3.1.2 Mean concentration of the total plume

The streamwise development of the lateral (spanwise) profiles of the total mean concentration C_T for cases 1–4 corresponding to the ground-level sources is shown in figure 4.5. Similarly, figure 4.6 displays the streamwise evolution of C_T for cases 5–8 corresponding to the elevated sources. In all these cases, the total mean concentration has been non-dimensionalized using the corresponding maximum mean concentration $C_{T,\mathrm{m}}$ at a given downstream location. Recall again that the mean concentration from the two individual sources are additive, and therefore, the total mean concentration C_T for the two sources is simply a linear superposition of the two individual mean concentrations.

For the ground source release case, it is apparent from figures 4.5(a)-(d) that the dual peak pattern in the lateral profile of the total mean concentration (arising from the dual sources) varies with both the source separation distance d and the downwind distance x/δ from the sources. The dual peak pattern is the most strongly expressed in case 4 (which has the largest source separation). As the downwind distance increases, the dual peak pattern becomes less apparent. In contrast to the streamwise evolution of the total mean plumes of cases 3 and 4, the total plume in cases 1 and 2 exhibits only one single peak at the midpoint between the two sources at the four downwind locations examined. This is because the source separation is the smallest in cases 1 and 2 and the two plumes have already overlapped significantly for these cases at the four downwind locations shown in figure 4.5.

The streamwise development of the total mean concentration in the four elevated source release cases are compared in figures 4.6(a)-(d). Similar to the ground source release case, a dual peak pattern in the total mean plume appears at the near-source downwind locations for those test cases with large source separation. A comparison between figures 4.5 and 4.6 reveals that for all four source separation distances tested in the ground and elevated source release scenarios, the dual peak pattern vanishes entirely for $x/d > 15$ and 12, respectively. The difference in behavior here

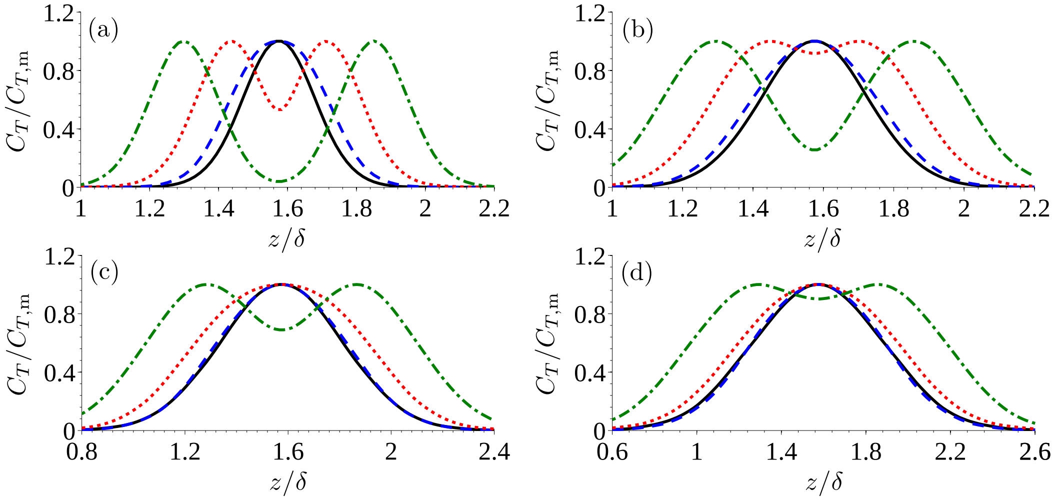

Figure 4.5: The lateral profiles of the total mean concentration for cases 1 (solid line); 2 (dashed line); 3 (dotted line); and, 4 (dash-dot line) at normalized downwind fetches of (a) $x/\delta = 1$, (b) 2, (c) 4, and (d) 6 for the ground-level sources. These profiles are obtained at the source height $y^+ = 5$.

arises from the fact that for the elevated plume, the absolute magnitude of the lateral plume spread exceeds that for the (near) ground-level source in the turbulent diffusive regime ($x/\delta > 2.2$). As a consequence, the disappearance (or, merging) of the two concentration peaks from the individual sources in the lateral profile of the total mean concentration occurs at a smaller downwind distance for the elevated source than for the ground-level source.

4.3.2 Concentration Fluctuations

In this subsection, the interaction of the dual plumes as manifested through the behavior of the second-order concentration moment is investigated. The RMS concentration profiles of a single plume are first studied in order to provide a point of reference for comparison with the results of the dual plumes.

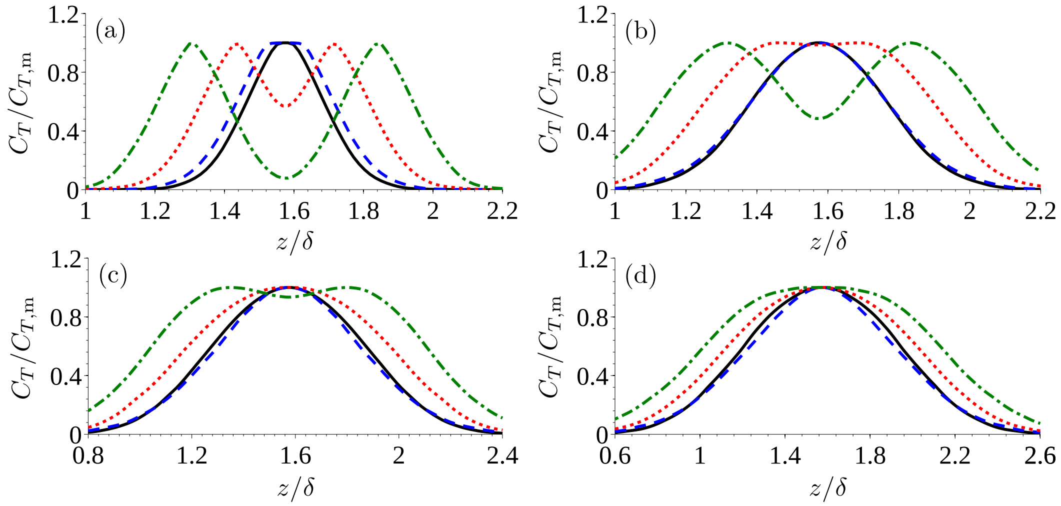

Figure 4.6: The lateral profiles of the total mean concentration for cases 5 (solid line); 6 (dashed line); 7 (dotted line); and, 8 (dash-dot line) at normalized downwind fetches of (a) $x/\delta = 1$, (b) 2, (c) 4, and (d) 6 for the elevated sources. These profiles are obtained at the source height $y^+ = 40$.

4.3.2.1 Single plume fluctuations

Figure 4.7 compares the lateral profiles of the RMS concentration $\hat{c}$ at source height for a single ground-level and a single elevated source release. The RMS concentration has been non-dimensionalized using its maximum value $\hat{c}_\mathrm{m}$ at a given downstream position. The RMS concentration profiles for the ground-level source exhibit off-axis peaks at all the downstream locations shown in figure 4.7. In contrast, the RMS concentration profiles for the elevated source have a single central peak at downstream locations close to the source (for $x/\delta = 1$ and 2) with the emergence of off-axis peaks at locations further downstream of the source (for $x/\delta = 4$ and 6). These differences exhibited in the RMS concentration profiles for the ground-level and elevated sources can be explained as follows.

From figure 4.7, it is seen that for the ground-level source, the off-axis peaks in the lateral profile of $\hat{c}$ occur approximately at $z_p = z_s \pm \sigma_z$. Owing to the fact that the lateral profiles of C are Gaussian, these off-axis peak locations coincide with the inflection points of the mean concentration profile, where the production rate

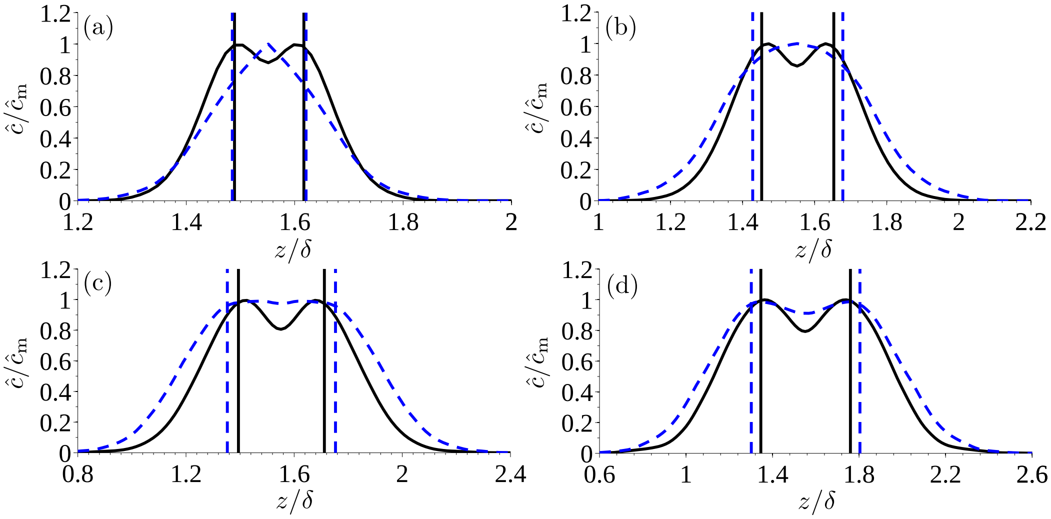

Figure 4.7: Comparison of the lateral profiles of $\hat{c}$ for a single ground-level (solid line) and a single elevated (dashed line) plume at source height and at four downwind fetches of (a) $x/\delta = 1$, (b) 2, (c) 4, and (d) 6 from the source. The vertical solid and dashed lines demarcate the spanwise positions located at $\pm\sigma_z$ from the mean plume centerline for the ground-level and elevated source, respectively.

of the concentration variance ($-\overline{u_i'c'}\partial C/\partial x_i$) is the largest due to the large mean concentration gradients. Similarly, the location of the local minimum in the lateral profile of $\hat{c}$ for the ground-level source occurs at a location with zero production rate of the concentration variance (i.e., $-\overline{u_i'c'}\partial C/\partial x_i = 0$), where the mean concentration is maximum (and associated with the location where the spanwise mean concentration gradient vanishes).

In contrast to the ground-level source, it is seen from figure 4.1 that for the elevated source, the plume is in the turbulent convective regime of development for $x < 2.2\delta$, where meandering motions are dominant. This distinct physical feature, where plume meander provides the major contribution to the concentration fluctuations, is absent for the ground-level source. Based on the study of a fluctuating plume model, Yee and Wilson (2000) indicated that strong meandering motions can lead to the obliteration of the off-centerline peaks in the lateral profiles of $\hat{c}$. However, as shown in figures 4.7(c) and (d), at locations further downstream of the elevated source when the plume has transitioned to the turbulent diffusive regime of development, the emergence of off-centerline peaks in the lateral profile of $\hat{c}$ is observed. Again, the location of these off-axis peaks in the profiles of $\hat{c}$ corresponds to the inflection points in the profile of the mean concentration C, which has a Gaussian distribution in the lateral direction. Note that for both the ground-level and elevated sources, off-axis peaks of $\hat{c}$ are observed in the turbulent diffusive regime of plume development where the meandering motions no longer provide the dominant contribution to the concentration fluctuations.

4.3.2.2 Total plume fluctuations

Figures 4.8 and 4.9 compare the lateral profiles of the RMS concentration of the total plume ($\hat{c}_T$) for the ground-level and elevated source releases at their respective source heights. In these lateral profiles, $\hat{c}_T$ has been normalized by the maximum value $\hat{c}_{T,\mathrm{m}}$, such that the highest value is unity. At all downstream locations shown in figure 4.8, the profiles of $\hat{c}_T$ for cases 1 and 2 (near ground-level sources) exhibit two off-axis peaks with a local minimum along the centerline (between the two sources) at all the downstream fetches considered. In contrast, profiles of $\hat{c}_T$ for cases 3 and 4 (near ground-level sources) exhibit four off-axis peaks at $x/\delta = 1$, 2 and 4, with the ratio of these peak values to the centerline value of $\hat{c}_T$ decreasing with increasing downstream distance from the sources. Lateral profiles of $\hat{c}_T$ for cases 5–8 (elevated sources) appear to be generally simpler in pattern than those for cases 1–4 (near ground-level sources). In particular, only case 8 at the further downwind fetches of $x/\delta = 4$ and 6 exhibit four off-axis peaks in the lateral profiles of $\hat{c}_T$ (albeit very weakly at $x/\delta = 4$). Based on the discussion for the downstream evolution of the spanwise profiles of the total mean concentration C_T and the RMS concentration $\hat{c}$ for a single plume in the previous section, the downstream evolution of the spanwise profiles of $\hat{c}_T$ for the ground-level and elevated sources can be explained as follows.

As is shown earlier for a single ground-level source, the meandering effect on

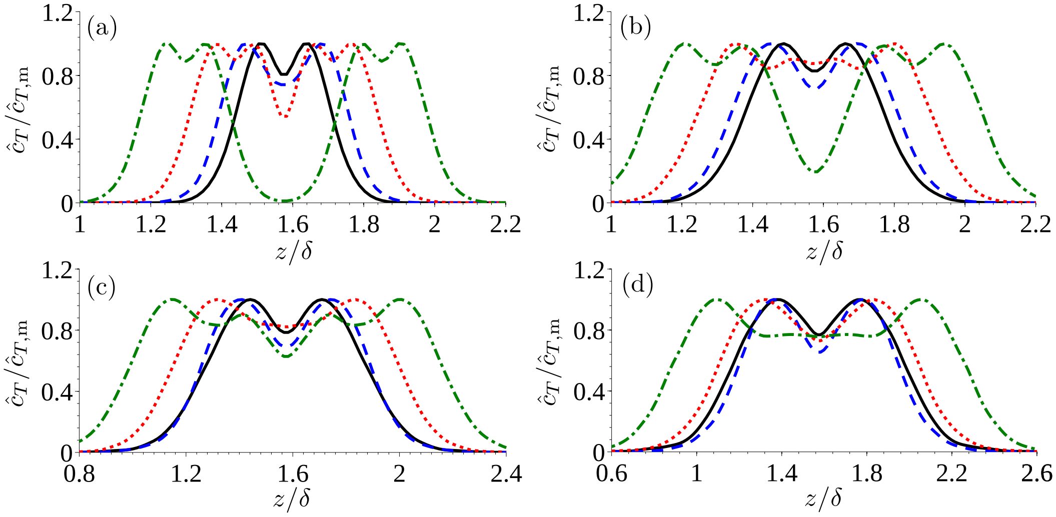

Figure 4.8: Lateral profiles of RMS concentration $\hat{c}_T$ of the total plume at source height corresponding to cases 1 (solid line), 2 (dashed line), 3 (dotted line) and 4 (dash-dot line) at four downwind fetches of (a) $x/\delta = 1$, (b) 2, (c) 4, and (d) 6 for two near ground-level sources.

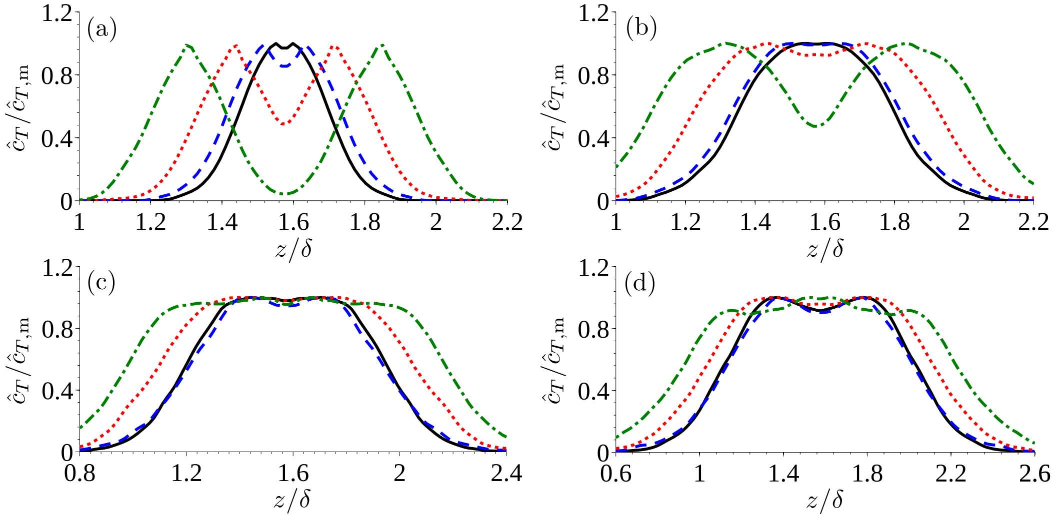

Figure 4.9: Lateral profiles of RMS concentration $\hat{c}_T$ of the total plume at source height corresponding to cases 5 (solid line), 6 (dashed line), 7 (dotted line) and 8 (dash-dot line) at four downwind fetches of (a) $x/\delta = 1$, (b) 2, (c) 4, and (d) 6 for two elevated sources.

concentration fluctuations is small. Therefore, the local minima of $\hat{c}_T$ for the ground-level source (cases 1–4) coincide with the extremal locations in the corresponding total mean concentration profile, and the locations of local maxima of $\hat{c}_T$ coincide with the locations of maximum absolute gradient of total mean concentration profile ($\partial C_T/\partial x_i$). This conclusion can be confirmed by comparing figure 4.8 with figure 4.5 for the ground-level source cases. To further investigate this phenomenon, in figures 4.10 and 4.11, the profiles of the mean concentration C_T and RMS concentration $\hat{c}_T$ of the total plume are directly compared at four downstream locations for cases 1 and 3, respectively. In both figures, the values of C_T and $\hat{c}_T$ have been normalized using the corresponding local maxima of the profiles and labeled generically using ϕ/ϕ_m. At all downstream fetches shown, the locations of the local minima in the $\hat{c}_T$ profile coincide with the locations of the local extrema in the associated C_T profile (viz., locations where the derivative of C_T with respect to z becomes vanishingly small). Similarly, the local maxima in the $\hat{c}_T$ profile coincide with the locations of the inflection points in the corresponding C_T profile (viz., locations corresponding to curvature changes in the profile associated with points where the second derivative of C_T with respect to z becomes vanishingly small). Similar behavior is also observed in cases 2 and 4 for the two near ground-level sources.

In section 4.3.1.1, it is shown that plume meandering for a single elevated source is significant at $x/\delta = 1$ and 2. However, at $x/\delta = 4$ and 6, the meandering effect is significantly attenuated with the result that the $\hat{c}_T$ profiles for the elevated sources resemble those for the ground-level sources. To investigate the dual plume interference, the lateral profiles of C_T and $\hat{c}_T$ for cases 5 and 7 (two elevated sources) are superimposed in figures 4.12 and 4.13, respectively, at 4 different downwind fetches from the sources. As shown in figures 4.12(a) and (b) and 4.13(a) and (b), close to the sources at $x/\delta = 1$ and 2, the RMS concentration from each single source is unimodal (with the mode at the respective plume centerline shown by downward pointing arrows) and these individual peaks are resolved in the total RMS concentration profile. This is

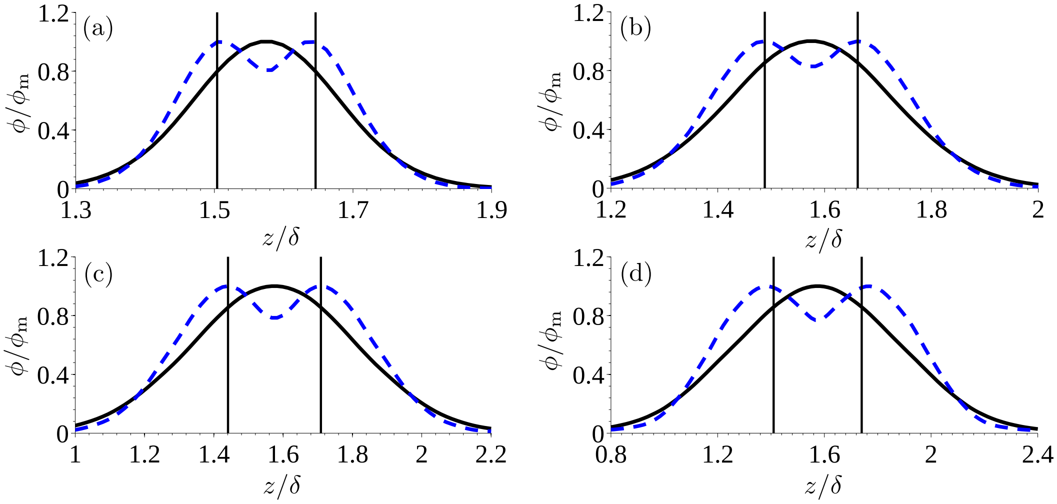

Figure 4.10: Lateral profiles of the total mean concentration C_T (solid line) and the total RMS concentration $\hat{c}_T$ (dashed line) at source height corresponding to case 1 (near ground-level sources separated by $d/\delta = 0.049$) at four downwind fetches of (a) $x/\delta = 1$, (b) 2, (c) 4, and (d) 6 from the two sources. Vertical solid lines indicate the locations of inflection points in the lateral profiles of the total mean concentration for case 1.

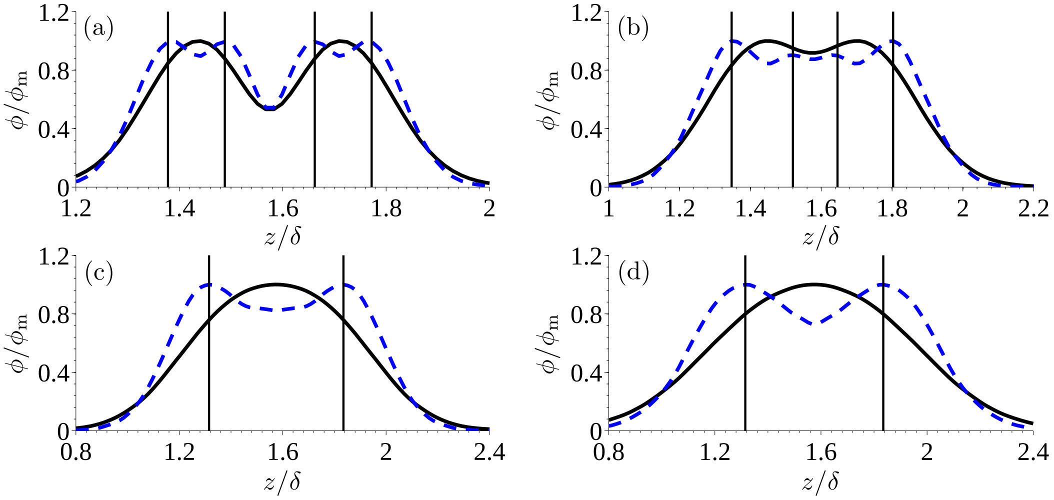

Figure 4.11: Lateral profiles of the total mean concentration C_T (solid line) and the total RMS concentration $\hat{c}_T$ (dashed line) at source height corresponding to case 3 (near ground-level sources separated by $d/\delta = 0.279$) at four downwind fetches of (a) $x/\delta = 1$, (b) 2, (c) 4, and (d) 6 from the two sources. Vertical solid lines indicate the locations of inflection points in the lateral profiles of the total mean concentration for case 3.

because at downwind fetches near the sources, the meandering effect is strong in each elevated plume, which tends to obliterate the off-axis peaks in the RMS concentration profile of each plume. As a result, the peaks in the total RMS concentration only occur at the mean centerline (axis) of the two plumes. By comparing figures 4.12(a) and (b) with 4.13(a) and (b), respectively, it is obvious that this physical feature (as a result of meandering effects) is more distinctively expressed as the source separation distance increases. Further downwind of the sources at $x/\delta = 4$ and 6, the meandering is either weak or negligible, and the dual plume interference is dominated by internal fluctuations. In consequence, as shown in figures 4.12(c) and (d) and figures 4.13(c) and (d), the total mean concentration C_T exhibits a single peak, and the locations of the local maxima in the $\hat{c}_T$ profile (off-axis peaks) coincide with the locations of the inflection points in the C_T profile. Similar behavior is observed in cases 6 and 8 for the two elevated sources with larger source separations.

4.3.3 Correlation Functions

The streamwise variation of the second-order correlation functions (or, cross correlation) at the midpoint in the spanwise direction between the two plumes at the source height is shown in figure 4.14. Similar to the observation in section 3.3.4, four distinct stages in the streamwise evolution of $\rho^{[1|1]}$ can be identified from figure 4.14, which are analyzed as follows. To facilitate the discussion, the streamwise developments of the mean plume width ($2\Sigma_z$) and the relative plume width ($2\Sigma_r$) for single ground-level and elevated sources are shown in figures 4.15 and 4.16, respectively.

- **Stage I: Zero Interference** ($\rho^{[1|1]} \approx 0$)

As is evident in figure 4.14, the zero interference pattern are the most strongly expressed for cases 3, 4, 7 and 8, which feature large source separation distances. However, if the source separation distance d is small (as in cases 1 and 5), this stage is not observed owing to the size of the sources σ_0 in relation to the source separa-

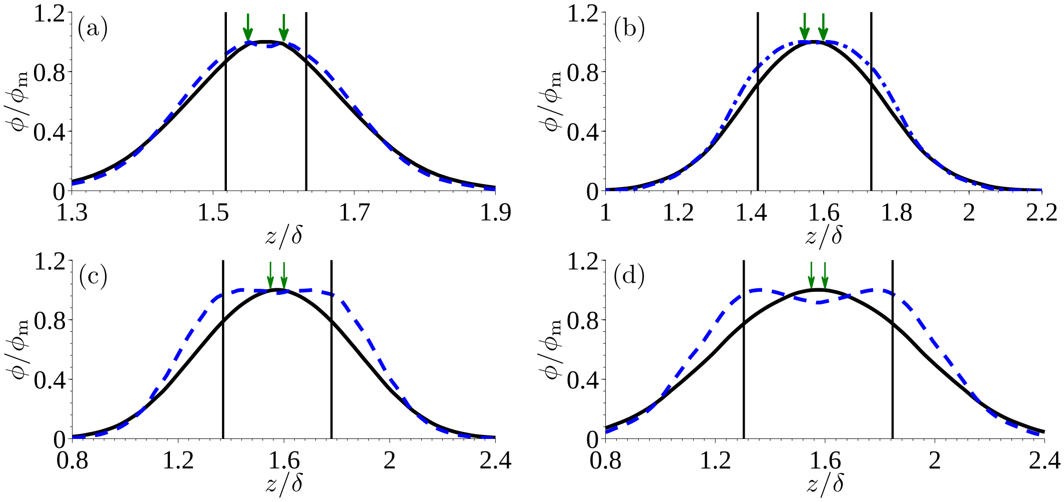

Figure 4.12: Lateral profiles of the total mean concentration C_T (solid line) and the total RMS concentration $\hat{c}_T$ (dashed line) at source height corresponding to case 5 (elevated sources separated by $d/\delta = 0.049$) at four downwind fetches of (a) $x/\delta = 1$, (b) 2, (c) 4, and (d) 6 from the two sources. Vertical solid lines indicate the locations of inflection points in the lateral profiles of the total mean concentration for case 5. The downward pointing arrows delineate the spanwise locations of the two sources.

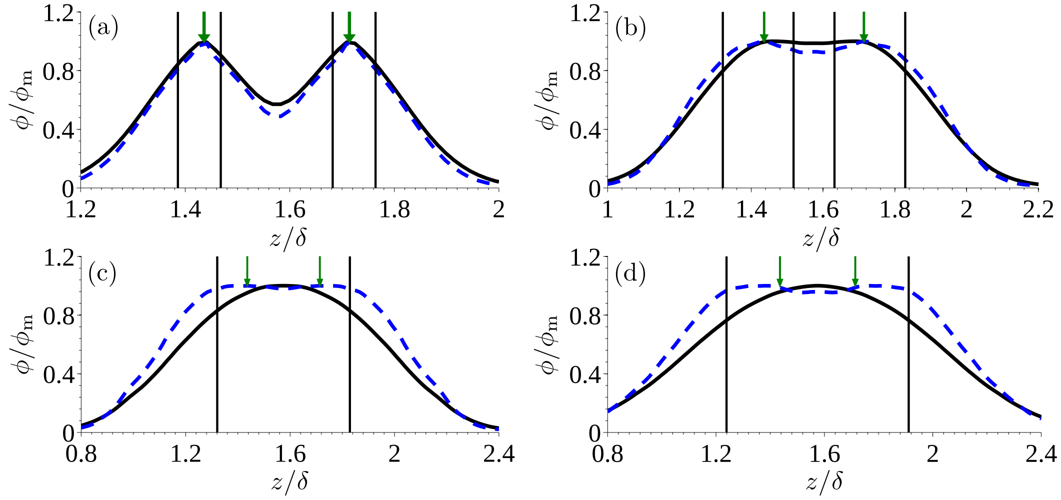

Figure 4.13: Lateral profiles of the total mean concentration C_T (solid line) and the total RMS concentration $\hat{c}_T$ (dashed line) at source height corresponding to case 7 (elevated sources separated by $d/\delta = 0.279$) at four downwind fetches of (a) $x/\delta = 1$, (b) 2, (c) 4, and (d) 6 from the two sources. Vertical solid lines indicate the locations of inflection points in the lateral profiles of the total mean concentration for case 7. The downward pointing arrows delineate the spanwise locations of the two sources.

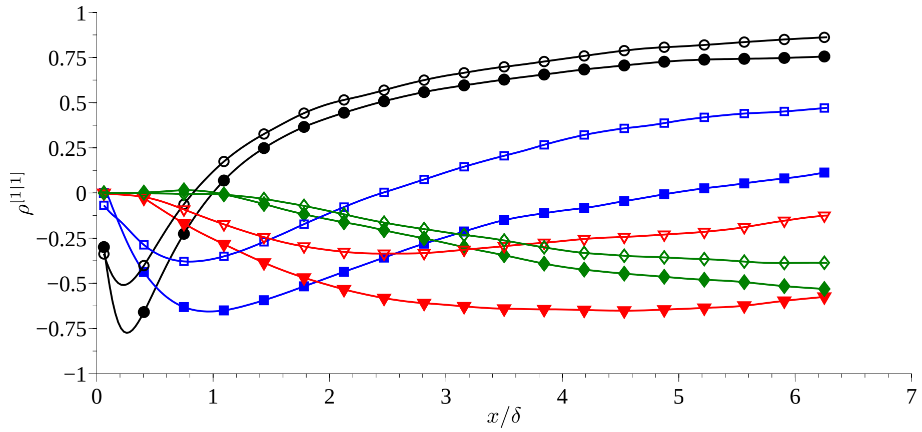

Figure 4.14: Streamwise variation of $\rho^{[1|1]}$ at the midpoint in the spanwise direction between the two plumes at source height. Cases 1 (●), 2 (■), 3 (▼), 4 (♦), 5 (○), 6 (□), 7 (▽), and 8 (◇).

tion distance d. As shown in figures 4.15 and 4.16 (for cases 1 and 5, respectively), at downwind fetches very close to the sources, the mean plume width (shown by solid symbols) of each source is comparable to or larger than the source separation d, resulting in a non-zero correlation between the two plumes. Figure 4.14 reveals that this stage of development extends to a shorter downwind distance for elevated source cases compared to ground-level source cases. This is because, as shown in figure 4.1(a), an elevated mean plume disperses faster compared to a ground-level mean plume, and consequently two elevated mean plumes overlap at a shorter downwind location compared to two ground-level mean plumes.

- **Stage II: Destructive Interference** ($\rho^{[1|1]} < 0$)

From figure 4.14, the destructive pattern exists in all 8 test cases. Furthermore, it is evident from an examination of figures 4.15 and 4.16 that in this stage, the lateral spreading of the mean plume (shown by solid symbols) is initially much larger than that of the relative plume (shown by hollow symbols) and $\rho^{[1|1]}$ becomes increasingly negative initially (owing to the fact that the correlation between the mean plumes $C_A C_B$ is stronger than that of the instantaneous plumes $\overline{c_A c_B}$). Eventually, the plume meandering decreases and the lateral spreading of the relative plume approaches

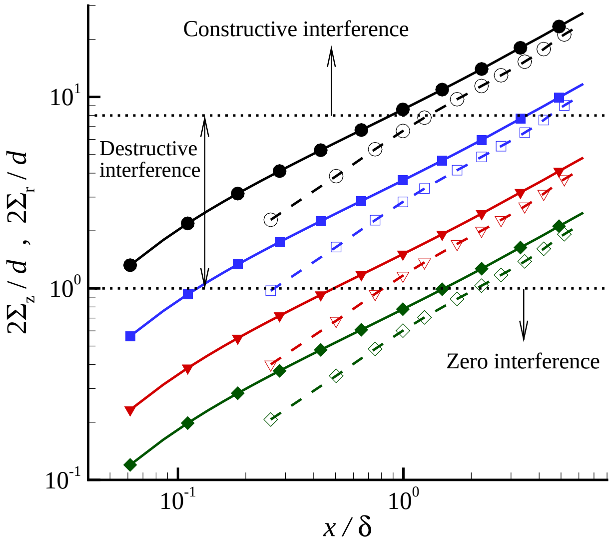

Figure 4.15: The streamwise evolution of the mean plume width $2\Sigma_z$ (solid symbols) and the relative plume width $2\Sigma_r$ (hollow symbols) for a single ground-level source non-dimensionalized by the source separation distance (d) for cases 1 (● and ○), 2 (■ and □), 3 (▼ and ▽) and 4 (◆ and ◇). The horizontal dotted lines used for dividing the four stages of dual plume interference are conceptual.

to that of the mean plume, leading to the condition that $\overline{c_A c_B}$ grows faster than $C_A C_B$. As a direct consequence, the value of $\rho^{[1|1]}$ starts to increase (towards less negative values) after reaching its absolute minimum. Figure 4.14 shows that in the second stage, the ground-level source cases have stronger negative cross correlation (a negatively valued trough) compared to the elevated source cases. This is because, as shown in figure 4.1(b), for a ground-level source release the lateral spreading of the relative plume approaches to that of the mean plume ($\sigma_r \to \sigma_z$) at a slower rate compared to that for an elevated source release.

- **Stage III: Constructive Interference** ($\rho^{[1|1]} \geq 0$)

This stage of development is observed for cases 1, 2, 5 and 6. A careful investigation of figure 4.14 in conjunction with figures 4.15 and 4.16 shows that the third stage of development begins roughly at downwind locations from the sources where the value of the ratio of the relative plume width to the source separation distance (i.e., $2\Sigma_r/d$) exceeds 8 and 5, respectively, for the ground-level and elevated sources. From

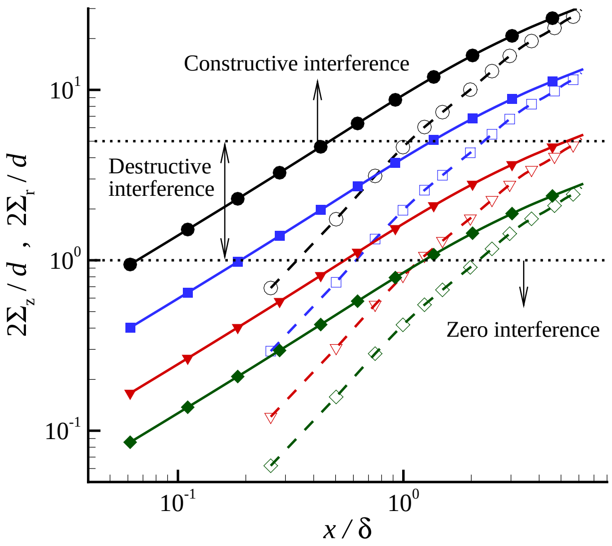

Figure 4.16: The streamwise evolution of the mean plume width $2\Sigma_z$ (solid symbols) and the relative plume width $2\Sigma_r$ (hollow symbols) for a single elevated source non-dimensionalized by the source separation distance (d) for cases 5 (● and ○), 6 (■ and □), 7 (▼ and ▽) and 8 (◆ and ◇). The horizontal dotted lines used for dividing the four stages of dual plume interference are conceptual.

figure 4.14, the cross correlation value is larger for the elevated source cases compared to the ground-level source cases at a given downwind location, although the rate of change of the cross correlation with downwind distance for the ground-level and elevated source cases is approximately equal (for the same source separation). This is because, as shown in figure 4.1 at far downwind locations from the sources, the rate of plume dispersion (absolute and relative) of an elevated plume approaches to that of a ground-level plume.

- **Stage IV: Complete mixing** ($\rho^{[1|1]} \approx 1$)

A comparison of the profiles exhibited in figure 4.14 indicates that the cases with a smaller source separation tend to reach this complete mixing state earlier than the cases with a larger source separation. Such an asymptotic behavior is captured in cases 1 and 5. However, in order to reproduce this complete mixing stage in the other six test cases, a much longer downwind fetch would be required in the simulations.

Figure 4.17 exhibits the lateral profiles of $\rho^{[1|1]}$ for all eight cases (see table 4.1)

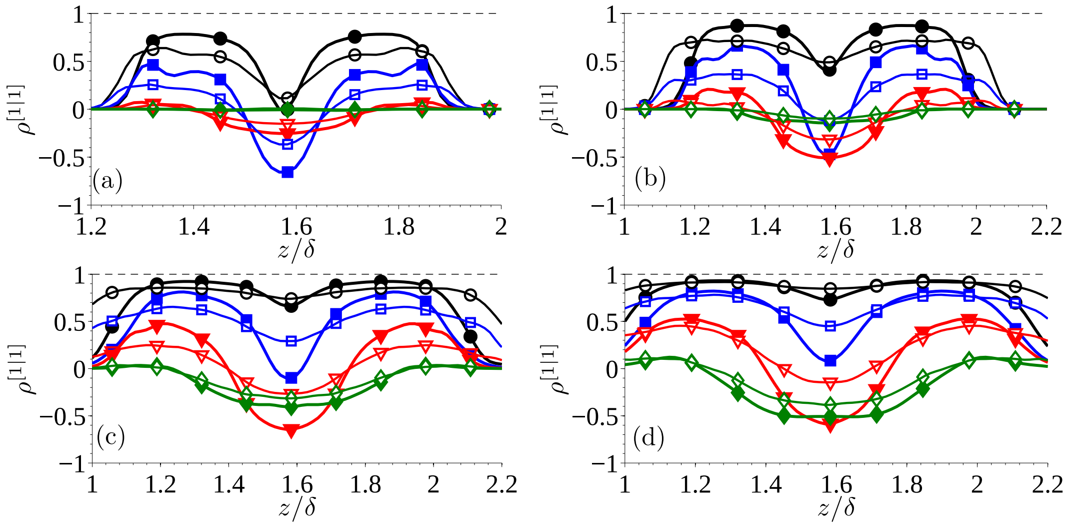

Figure 4.17: Lateral profiles of $\rho^{[1|1]}$ at source height at four downwind fetches of (a) $x/\delta = 1$, (b) 2, (c) 4, and (d) 6 from the two sources. Ground-level source releases are cases 1 (●), 2 (■), 3 (▼), 4 (♦). Elevated source releases are cases 5 (○), 6 (□), 7 (▽), and 8 (◇).

at the source height at four different downwind distances from the dual sources. The streamwise variation in the lateral profiles of $\rho^{[1|1]}$ also reflects the four stages in the mixing of the two plumes. In the first stage of the downwind development of $\rho^{[1|1]}$, the shape of the lateral profile is flat with a zero value, because there is no interaction between the two plumes (viz., a vanishingly small probability for the two instantaneous plumes to overlap). This first stage of development is more evident for those cases associated with a large source separation distance d and at downstream locations close to the sources (e.g., cases 4 and 8 at $x/\delta = 1$ in figure 4.17(a)). The second stage of development is associated with characteristic rounded M-shaped lateral profiles. These M-shaped lateral profiles exhibit a negative-valued minimum in $\rho^{[1|1]}$ midway between the two plumes and broad positive-value maxima are found on either side of the midpoint location. Typical examples of the second stage of development exhibited in figure 4.17 include case 2 for $x/\delta < 6$, cases 3 and 7 at all available downwind fetches and case 6 for $x/\delta < 4$.

As discussed earlier, the negative-valued minimum at the midpoint between the two plumes is due to the fact that a large eddy (relative to the plume width) at this location causes the concentration contributed by one plume to increase and that contributed by the other plume to decrease. For sources that are close enough together, the positive maximum values in $\rho^{[1|1]}$ away from the centerline arise from the fact that at these locations, the two plumes meander together frequently, causing the two concentrations to either increase or decrease simultaneously. During the third stage, the minimum of the M-shaped lateral profile becomes positively valued, and the profile itself begins to flatten out as the two plumes overlap each other to a greater and greater extent. Typical examples of the third stage of development can be observed in figures 4.17(a), (b) and (c) for cases 1 and 5, and figure 4.17(d) for cases 2 and 6. Finally, during the fourth stage of development, a uniform flat profile of $\rho^{[1|1]}$ with an asymptotic value of unity forms indicating that the concentrations in the two overlapping plumes are completely mixed. As shown in figure 4.17(d), this limiting behavior is seen by cases 1 and 5 at a large downwind distance (e.g., $x/\delta = 6$) from the sources.

4.3.4 Concentration Co-spectrum and Coherency Spectrum

Similar to the analysis given in section 3.3.5, the information about the scales of the mixing of the two elevated plumes can be quantified using the co-spectrum and coherency spectrum. The pre-multiplied co-spectrum and the coherency spectrum obtained at the midpoint between the two plumes at source height for case 5 are shown in figures 4.18(a) and (b), respectively. In order to investigate the streamwise evolutions of the pre-multiplied co-spectrum and coherency spectrum, several downstream locations (with different x/δ values) are considered in the comparative study. Here, the co-spectrum $Co_{c'_A c'_B}$ and the coherency spectrum $\rho_f^{[1|1]}$ for the elevated source are presented, as the results of the ground-level source are previously presented and discussed in section 3.3.5.

The streamwise evolution of $Co_{c'_A c'_B}$ and $\rho_f^{[1|1]}$ follows the streamwise evolution of

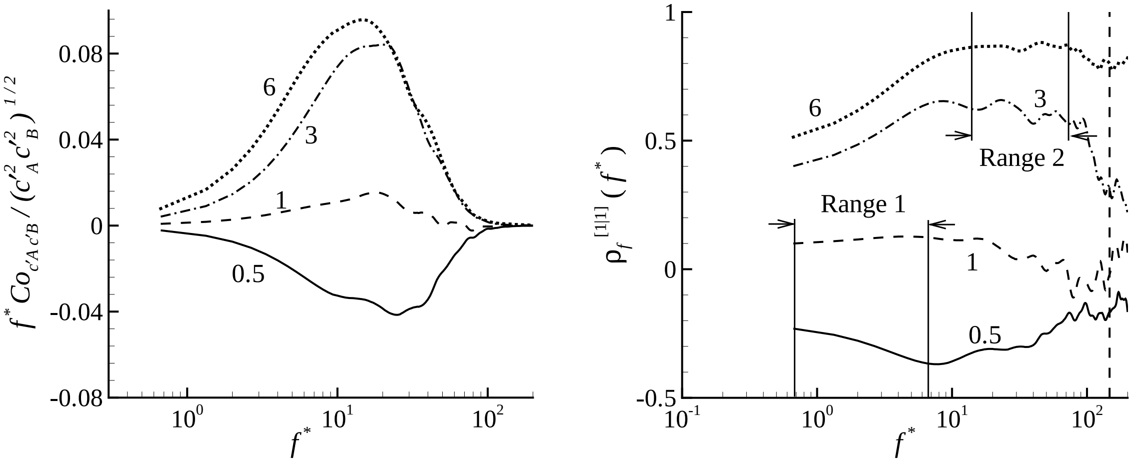

(a) Pre-multiplied co-spectrum (b) Coherency spectrum

Figure 4.18: The pre-multiplied co-spectrum and coherency spectrum of dual plumes for case 5 obtained at the midpoint between the two plumes and at source height, for $x/\delta = 0.5$ (solid line), 1 (thin dashed line), 3 (dash-dotted line), 6 (dotted line) and 12 (thick dashed line). The straight vertical dashed line shows the frequency corresponding to the Kolmogorov scale. Ranges 1 and 2 indicate the leading scales in the turbulent convective and the turbulent diffusive regimes, respectively.

the cross correlation. The four stages in the development of the cross correlation can also be observed from the pre-multiplied co-spectrum and coherency spectrum for case 5, which is similar to those for the ground-level sources (see figure 3.14(b) and figure 3.15(b)). The leading scales in the mixing of the two plumes are identified and labeled in figure 4.18(b) (i.e., ranges 1 and 2). It is seen that in the turbulent convective regime (i.e., $x/\delta < 2.2$), the leading scales (range 1) are located at low frequencies. However, in the turbulent diffusive regime (i.e., $x/\delta > 2.2$), the leading scales (range 2) are located at higher frequencies. This indicates that the rate of mixing of two plumes is faster at large scales in the turbulent convective regime. This is because plume meandering is a large-scale phenomenon, and it is the dominant mechanism in the mixing of the two plumes in the turbulent convective regime. The effect of meandering reduces significantly in the turbulent diffusive regime where the internal turbulent mixing provides the primary contribution to the mixing process. Therefore, the rate of mixing of two plumes is faster at small scales when the plume is in the turbulent diffusive regime. These observation for the elevated sources are consistent with those for the ground-level sources demonstrated previously in figure 3.15(b).

4.3.5 Concentration PDF and EDF

In this subsection, the concentration PDF of a single plume is first studied, followed by a detailed discussion of the effects of plume interference on the concentration EDF of the total plume.

4.3.5.1 Concentration PDF of a single plume

The concentration PDF at point $\mathbf{x} = (x, y, z)$ is defined as

$$f(\chi; \mathbf{x}) d\chi = \Pr\{\chi \leq c(\mathbf{x}) < \chi + d\chi\} \quad , \tag{4.4}$$

where $\Pr\{\cdot\}$ denotes the probability and χ is the value that can be assumed by the (random) instantaneous concentration $c(\mathbf{x})$. Figure 4.19 compares the nondimensionalized concentration PDF at source height along the mean plume centerline for a single ground-level or elevated source at four downwind distances from the source. This figure shows that the concentration PDF at the plume centerline for the ground-level source exhibits a Gaussian-like form (with the mode located at $\chi/C = 1$) at all downstream locations from the source.

In contrast to the concentration PDF for the ground-level source, the concentration PDF along the plume centerline of the elevated source exhibits an exponential form at downwind locations close to the source and approaches a Gaussian-like form as the distance from the source increases. As shown in figures 4.19(a) and (b), for the elevated source case, the concentration PDF assumes an exponential-like form (with the PDF having a prominent peak at $\chi/C = 0$) over immediate downwind fetches from about $x/\delta = 0.5$ to 1. The peak at zero concentration for the PDF in the near-source region is due to the large dominant meandering motions that cause plume to move off the receptor location to give long periods of zero concentration. However,

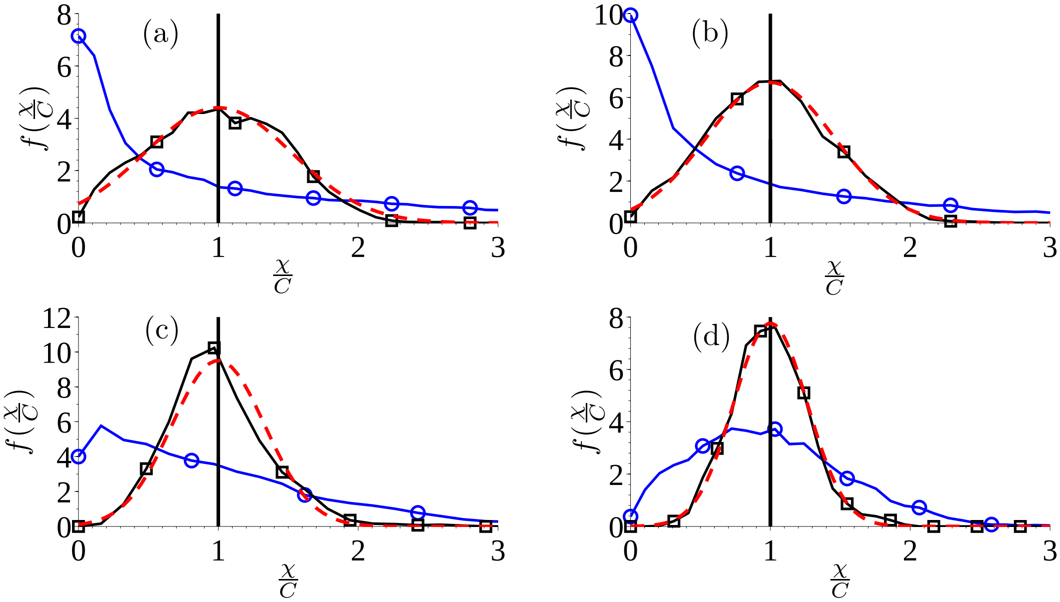

Figure 4.19: Concentration PDF at source height along the mean plume centerline for a single ground-level (□) or elevated (◯) source at four downwind fetches of (a) $x/\delta = 0.5$, (b) 1, (c) 3, and (d) 6 from the source. The dashed line shows the best Gaussian fit to the concentration PDF for the ground-level source.

as shown in figures 4.19(c) and (d), as the downstream distance increases beyond $x/\delta = 1$, the mode at zero concentration decreases significantly. Furthermore, as is evident in figure 4.19(d), in the region far downstream of the source, the concentration PDF for the elevated source tends to approach a Gaussian-like form (or, at least, a less skewed and more symmetrical) with the mode centered increasingly at $\chi/C \approx 1$. In this far downstream region, the instantaneous plume width has grown to fill the mean-plume width, the meandering effect becomes weaker and the mixing inside the instantaneous plume boundaries begins to dominate the concentration fluctuations.

Figure 4.20 compares the concentration PDF of the ground-level and elevated sources at four different crosswind locations off the mean plume centerline. The profiles in this figure are obtained at source height and at the downwind fetch of $x/\delta = 1$. As is evident in figures 4.20(a)-(d), as the crosswind distance from the plume centerline increases, the concentration PDF approaches an exponential-like form. Fackrell

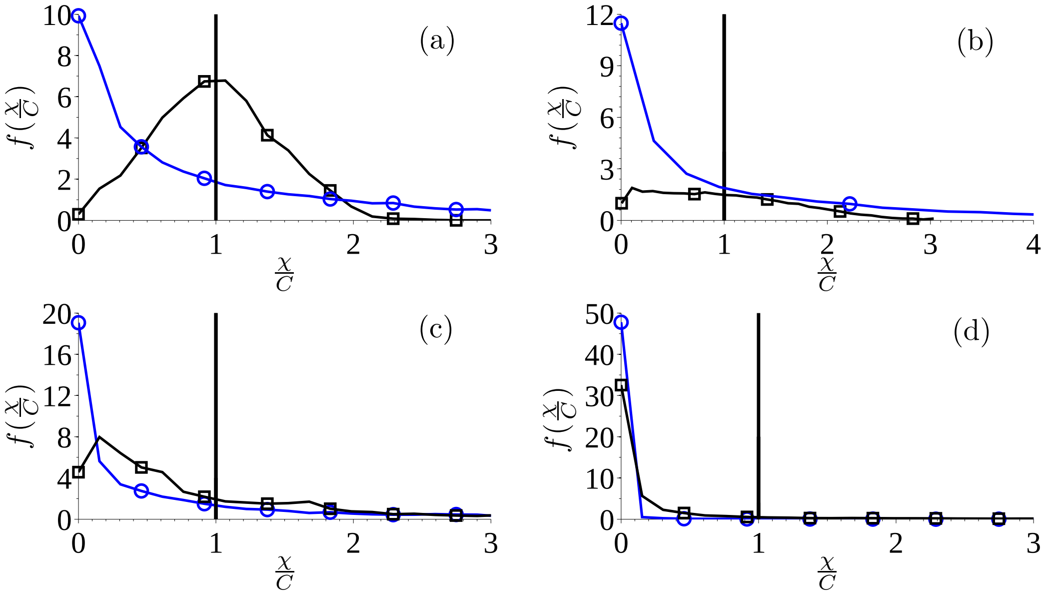

Figure 4.20: Concentration PDF at source height for a single ground-level (□) or elevated (○) source at the downwind fetch of $x/\delta = 1$ at crosswind locations from the mean-plume centerline of (a) $(z - z_s)/\sigma_z = 0$, (b) 0.8, (c) 1.9 and (d) 3.7.

and Robins (1982) obtained similar results in their experimental study of a tracer release from a single point source into a turbulent boundary layer. Naturally, as the plume fringes are approached, the concentration becomes ever more intermittent (viz., includes ever longer intervals of zero concentration), which results in a PDF with an increasingly narrow sharp peak at or near zero concentration and a form that becomes more and more skewed to the right. This trend holds for both the ground-level and elevated source cases, however, it is more strongly expressed for the elevated source releases.

4.3.5.2 Interference effect on concentration EDF of the total plume

One of the key interests in practical applications (such as industrial pollution monitoring and control in urban environments) is the knowledge of the probability of the occurrence of the largest concentration value (which corresponds to the most toxic or harmful condition to people). This can be quantified by the concentration EDF defined as

$$\mathrm{EDF}(\chi; \mathbf{x}) = 1 - \Pr\{c(\mathbf{x}) \leq \chi\} = 1 - \int_{0^-}^{\chi} f(\chi'; \mathbf{x}) d\chi' \quad . \tag{4.5}$$

Figure 4.21 compares the non-dimensionalized concentration EDF of the single and total plumes at four downwind distances from the source. The EDFs are obtained at source height at the midpoint between the two ground-level sources for case 1. The EDFs of the single plume are obtained at the same spatial location when only one of the ground-level sources is turned on. The concentration EDFs in this figure clearly reveal that the probability of finding a concentration above the level of the mean concentration (indicated by the vertical line) for the total plume is smaller than that for the single plume. More specifically, the distributions for the total concentration from the two sources exhibit shorter upper tails than those for the single source. This implies that in comparison with the single source release, the probability of observing very high concentrations is reduced for the two source release. Furthermore, as is clearly shown in figures 4.21(a)-(d), this effect of the shortening of the upper tail of the total plume EDF becomes less and less apparent as the downwind distance from the sources increases. Indeed, at $x/\delta = 6$, the elongation of the distribution in the upper tail becomes comparable for the single and two source releases. This observation is consistent with two source atmospheric tracer dispersion experiments of Sawford et al. (1985) and in the wind-tunnel tracer dispersion experiments of Stapountzis (1988).

In order to demonstrate in a more precise manner the reduction in the concentration $\mathrm{EDF}(\chi/C > 1)$ for the total plume in comparison with that for the single plume, a reduction factor RF is defined as follows:

$$\mathrm{RF}(\chi/C) = \frac{\mathrm{EDF}(\chi/C)_S}{\mathrm{EDF}(\chi/C)_T} \quad , \tag{4.6}$$

which is the ratio of the concentration EDF for a single plume (S) to that for the total plume (T). Figure 4.22 compares RF values for cases 1 and 2 (ground-level releases)

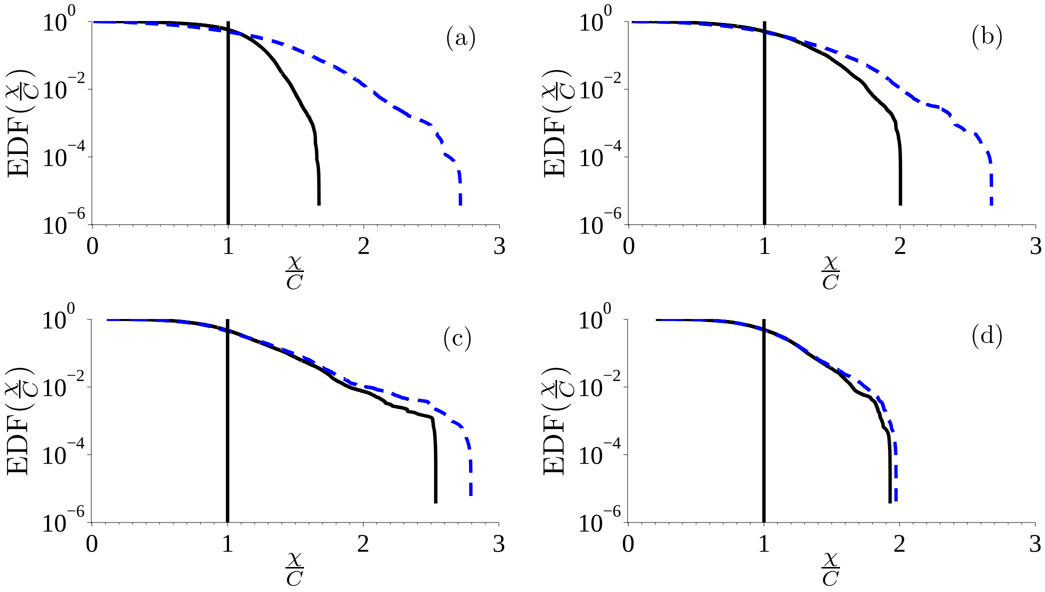

Figure 4.21: Concentration EDF of the total plume (solid line) and a single plume (dashed line) for case 1 in the midspan between the plumes at source height at four downwind fetches of (a) $x/\delta = 0.5$, (b) 1, (c) 3, and (d) 6 from the source(s).

and for cases 5 and 6 (elevated releases). This figure shows that for a concentration level below the mean concentration, RF(χ/C $<$ 1) $<$ 1. On the other hand, for a concentration level above the mean concentration, RF(χ/C $>$ 1) $>$ 1 for all cases and at all downstream locations shown in the figure. This indicates that occurrence of instantaneous concentration values less than the corresponding mean concentration is more frequent (is more probable) in the total plume than in the single plume. However, the reverse is true with respect to the frequency (or, probability) of occurrence of instantaneous concentrations greater than the corresponding mean concentration. Another interesting observation from figure 4.22 is that at a given downstream location, RF increases monotonically as the concentration level (χ/C) increases for $\chi/C > 1$. This implies that the difference between the probability of observing a high concentration in the single and total plume increases as the concentration level increases.

By comparing figures 4.14 with 4.22, there appears to be a negative correlation

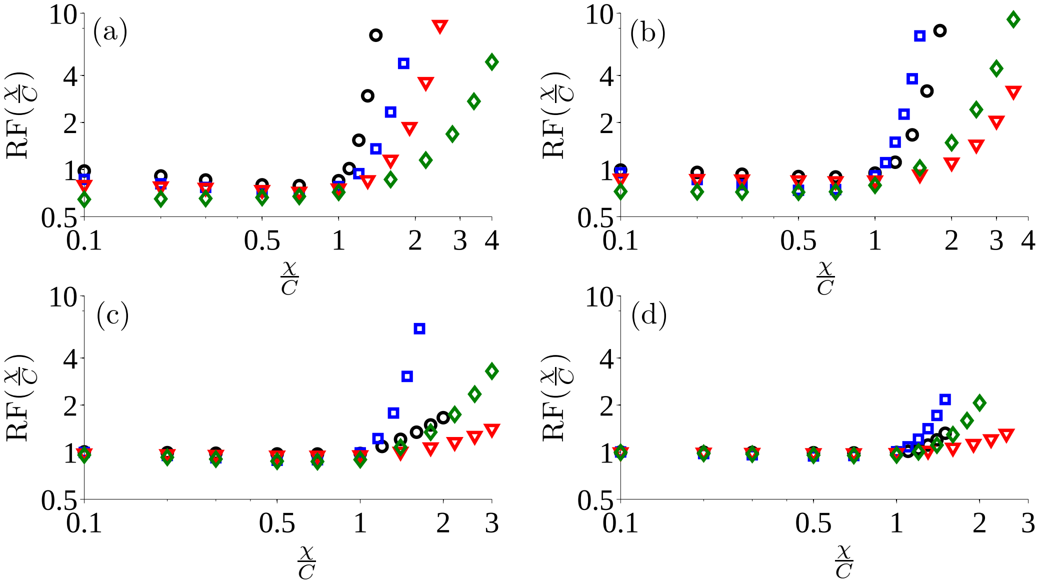

Figure 4.22: RF for cases 1 (◯), 2 (□), 5 (▽) and 6 (◇) as a function of concentration level at the midpoint between the two plumes at source height and at four downwind fetches of (a) $x/\delta = 0.5$, (b) 1, (c) 3, and (d) 6 from the sources.

between RF($\chi/C > 1$) and $\rho^{[1|1]}$ in the sense that an increase in RF($\chi/C > 1$) is associated with a decrease in $\rho^{[1|1]}$ and vice-versa at a given location. This observation is supported as follows. Figure 4.22 shows that RF for cases 1 and 5 decreases as the downstream distance increases from $x/\delta = 0.5$ to 6 for a given concentration level above the mean. In contrast, RF for cases 2 and 6 increases as the downstream distance increases from $x/\delta = 0.5$ to 1 for a given concentration level above the mean. However, RF($\chi/C > 1$) for cases 2 and 6 is seen to decrease with increasing downstream distance in the range from $x/\delta = 1$ to 6. From figure 4.14, it is seen that $\rho^{[1|1]}$ increases with increasing downwind distances over the range $0.5 \leq x/\delta \leq 6$ for cases 1 and 5. Furthermore, a perusal of figure 4.14 shows that $\rho^{[1|1]}$ first decreases over the range of downwind fetches from $x/\delta = 0.5$ to 1 and then increases over the range of downwind fetches from $x/\delta = 1$ to 6 for cases 2 and 6.

In order to investigate the relationship between RF($\chi/C > 1$) and $\rho^{[1|1]}$, figure 4.23 exhibits scatterplots of RF against $\rho^{[1|1]}$ for four concentration levels above the mean

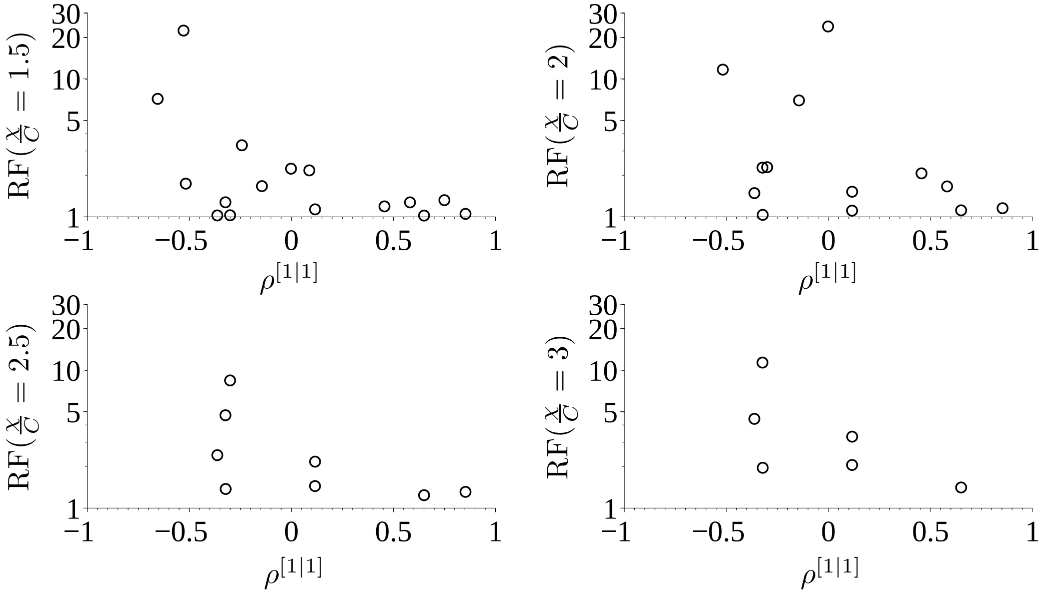

Figure 4.23: Scatterplots of RF against $\rho^{[1|1]}$ obtained at various downwind locations at the midpoint between the two plumes at source height.

concentration. The results in this figure are selected from cases in which the receptor location (z_m, midway in the spanwise direction between the two sources) lies within one mean plume dispersion σ_z of the plume centerline (z_s) for the single source, so that $|z_m - z_s| < \sigma_z$. This choice of the receptor location is to ensure that the plume intermittency has a minor role in the determination of the statistical correlation between RF($\chi/C > 1$) and $\rho^{[1|1]}$. A perusal of figure 4.23 shows that destructive interference (corresponding to $\rho^{[1|1]} < 0$) is associated with values of RF($\chi/C > 1$) that are significantly larger than unity, whereas constructive interference (corresponding to $\rho^{[1|1]} > 0$) is characterized by values of RF($\chi/C > 1$) that are comparable to unity. As shown in figure 4.23(d), this trend is the most strongly expressed for high concentration exceedances (associated with large χ/C values). This relationship between RF and $\rho^{[1|1]}$ can be explained as follows.

For the case of destructive interference (leading to $\rho^{[1|1]} < 0$) at a receptor location, the concentrations contributed by the two sources are out of phase in the sense that the two concentrations are simultaneously nonzero at the receptor location only rarely. The upshot of this is that the exceedance probability of a concentration level above the mean concentration is smaller for the total plume in comparison to that for a single plume. In contrast, for constructive interference at a receptor location (associated with $\rho^{[1|1]} > 0$), there is significant overlap between the two plumes which meander together (in phase) over the receptor location. In this stage of development, the initial source separation is forgotten and the concentration fluctuations from the two plumes behave as if they came from a coincident source. In consequence, the exceedance probabilities over various concentration levels for the total and single plume become more and more similar to each other with the result that $\mathrm{RF}(\chi/C)$ becomes more and more comparable to unity (and, indeed, it is expected that $\mathrm{RF}(\chi/C) \to 1$ as the two plumes overlap to such an extent that they become well mixed with $\rho^{[1|1]} \to 1$).

4.3.6 Higher-Order Concentration Moments

Figures 4.24(a) and (b) show the normalized concentration moment scatterplots of $\overline{c^3}/C^3$ and $\overline{c^4}/C^4$ plotted against $\overline{c^2}/C^2$ on a double logarithmic scale for a large number of points in the total plume. The concentration moments have been calculated for the total concentration of both the ground-level and elevated source releases. Remarkably, each of these scatterplots is seen to collapse onto a curve which implies that the third- and fourth-order concentration moments are determined effectively by a knowledge of the mean concentration and the second-order concentration moment.

The collapse of the normalized third- and fourth-order concentration moments against the normalized second-order concentration moment onto a curve has been reported by Yee and Chan (1997) for a single source release in a level open-terrain environment and by Yee (2009) in his follow-up study of a single source release in a built-up (urban) environment. From figures 4.24(a) and (b), it is interesting to note that this physical characteristic of the plume concentration field for a single source release reported by Yee and Chan (1997) also holds for the total concentration field resulting from a two source release for both the near ground-level and elevated sources. Yee and Chan (1997) proposed a left-shifted clipped-gamma distribution for the concentration PDF for a single plume dispersing in an open-terrain environment, viz.

$$f(\chi;\mathbf{x}) = \left(\frac{\chi+\zeta}{s}\right)^{\kappa-1} \frac{\exp\left(-(\chi+\zeta)/s\right)}{s\Gamma(\kappa)} + (1-\gamma)\delta(\chi) \quad . \tag{4.7}$$

There are four unknown parameters in this model: namely, $\kappa = \kappa(\mathbf{x}) > 0$, $s = s(\mathbf{x}) > 0$, $\zeta = \zeta(\mathbf{x}) \geq 0$ and $\gamma = \gamma(\mathbf{x}) \in [0,1]$. Here, $\Gamma(\kappa)$ is the gamma function, $\delta(\chi)$ is the Dirac delta function and χ is restricted to $0 \leq \chi < \infty$. Using the modeled concentration PDF, the nth-order concentration moment can be calculated as

$$\overline{c^m}(\mathbf{x}) = \int_{0^-}^{\infty} \chi^m f(\chi;\mathbf{x}) d\chi \quad . \tag{4.8}$$

The number of unknown parameters can be reduced to three independent parameters by recognizing that the intermittency factor γ can be determined as the area remaining under the clipped-gamma PDF curve for $c > 0$ so

$$\gamma(\mathbf{x}) = \Pr\{c(\mathbf{x}) > 0\} = \frac{\Gamma(\kappa;\zeta/s)}{\Gamma(\kappa)} \quad , \tag{4.9}$$

where $\Gamma(\kappa;\zeta/s)$ denotes the complementary incomplete gamma function. Using a comprehensive data set obtained from the CONFLUX project on a single plume dispersion (Yee et al. (1993b,a);Yee et al. (1994a,b)), Yee and Chan (1997) formulated a relationship between the normalized mean-square concentration $\overline{(c/C)^2}$ and the plume intermittency factor, viz.

$$\gamma = \min\left(1, \frac{3}{\overline{(c/C)^2}}\right) \quad . \tag{4.10}$$

With the two constraints given by equations 4.9 and 4.10, the four unknown parameters (κ, s, ζ and γ) can be uniquely determined by solving a system consisting of two transcendental equations (see Yee and Chan (1997) for more details). In the above procedure, only a knowledge of the mean concentration and the mean-square concentration is required to uniquely determine the four unknown parameters from this system of equations. Once these four parameters are determined, the concentration PDF in equation 4.7 is uniquely specified, and any higher-order concentration moments can be calculated using equation 4.8. Using this model, Yee and Chan (1997) and Yee (2009) were able to show that the higher-order concentration moments can be well predicted using only a knowledge of the mean and mean-square concentrations for the dispersion of a single plume in an open terrain or a built-up environment.

The solid line in figures 4.24(a) and (b) shows the normalized third- and fourth-order concentration moments for the total plume predicted using the clipped-gamma distribution model. Interestingly, it is seen that the clipped-gamma distribution provides very good predictions for the higher-order concentration moments of the total plume once the first- and second-order concentration moments of the total plume are known.

The collapse of the higher-order concentration moments on the two lowest-order concentration moments has important implications for the modeling of concentration fluctuations. Firstly, the collapse of the third and fourth-order concentration moments on the second-order concentration moment indicates that the concentration PDF can be described adequately by at most two parameters. Secondly, this two-parameter concentration PDF appears to be universal in the sense that it applies to the concentration from a single source or from two sources (generalization of this conclusion to more than two sources yet needs to be investigated). Thirdly, a knowledge of the first and second-order concentration moments of each single plume and of the second-order correlation function (required for the prediction of the second-order concentration moment of the total plume) is sufficient for the prediction of all higher-order concentration moments of the total plume. This is simply because the first-order concentration moment of the total plume is linearly superposable and the second-order concentration moment of the total plume can be obtained from $\overline{c_T^2} = \overline{c_A^2} + \overline{c_B^2} + 2(\rho^{[1|1]}(\overline{c_A^2} - C_A^2)^{1/2}(\overline{c_B^2} - C_B^2)^{1/2} + C_A C_B)$ which is an extension of equation 3.7.

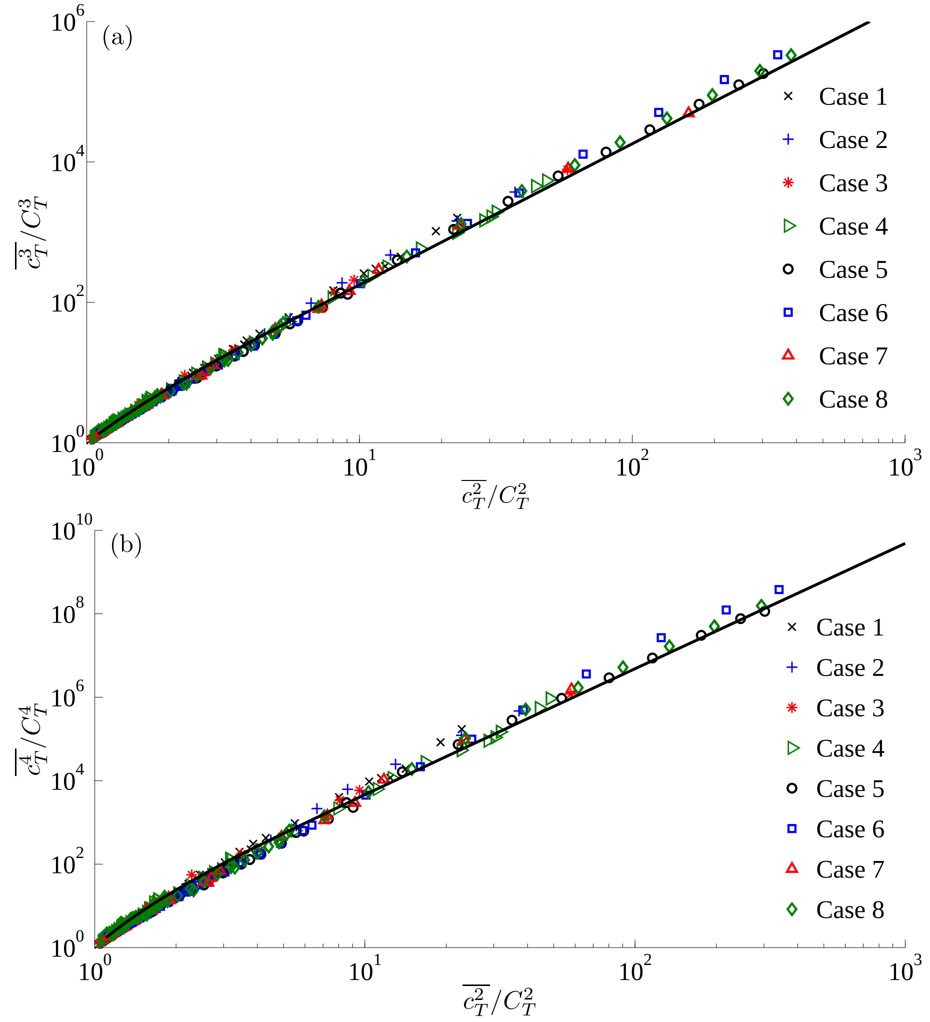

Figure 4.24: Scatterplots of the non-dimensionalized (a) third-order concentration moment and (b) fourth-order concentration moment, plotted against the non-dimensionalized second-order concentration moment for a large number of locations in the total plume. The prediction of the relationship between these moments provided by the clipped-gamma distribution model (solid line) is superimposed on the scatterplots.

4.4 Chapter Summary

DNS has been performed to study the effect of source separation distance on the interaction of two plumes released from two ground-level or elevated point sources in an open-channel flow. The dual plume interference has been investigated based on the mean and RMS values of the total concentration, the second-order correlation coefficients between the concentrations from the two sources, EDF for the total concentration, and the relationship between the third-order and fourth-order concentration moments and the second-order concentration moment for the total plume.

For both the ground-level and elevated releases, four distinct stages in the downwind development of the second-order correlation coefficient $\rho^{[1|1]}$ have been identified with respect to its distribution along the centerline between the two sources. These four stages of development include: (1) the zero interference stage where $\rho^{[1|1]} = 0$, (2) the destructive interference stage where $\rho^{[1|1]} < 0$, (3) the constructive interference stage where $\rho^{[1|1]} \geq 0$, and (4) the complete mixing state where $\rho^{[1|1]} \to 1$. Along the centerline between the two sources, the particular stage of development depends on the separation distance between the sources, the absolute and relative plume dispersion of the individual plumes, and the elevation of the sources in the wall-shear flow. It is observed that the downwind evolution of the second-order correlation coefficient over the four stages becomes faster as the source separation distance is reduced. Furthermore, the second-order correlation coefficient for a fixed source separation is generally larger for the elevated sources than for the ground-level sources at all downwind fetches.

The results of the concentration EDF showed that the probability of finding a concentration above the level of the mean concentration for the total plume is smaller than that for a single plume. The reduction in the exceedance probability of a high concentration level (above the mean concentration) in the total plume compared to that in a single plume can be precisely revealed through the so-called reduction factor (RF). It is observed that there is an anti-correlation between the RF and the second-order correlation function $\rho^{[1|1]}$. For destructive interference ($\rho^{[1|1]} < 0$), the RF values are significantly larger than unity, implying that exceedance probability for concentration levels above the mean concentration is significantly reduced for the total plume relative to that for a single plume. In contrast, for constructive interference

($\rho^{[1|1]} > 0$), values for the RF approach unity, implying that the exceedance probabilities for concentration levels above the mean concentration for the total plume and a single plume are comparable. Indeed, for strong constructive interference where $\rho^{[1|1]} \rightarrow 1$, it is expected that RF $\rightarrow 1$ as the total plume approaches to a single plume.

It is interesting to observe that the scatterplots of the normalized third and fourth-order concentration moments against normalized second-order concentration moment for the total plume collapse onto a single (universal) curve. The clipped-gamma model of Yee and Chan (1997) for a single plume was found to provide a good prediction of the higher-order concentration moments given knowledge of the only first and second-order concentration moments for the dual source release. This implies that a knowledge of the first and second-order concentration moments for the single plume in conjunction with a knowledge of the second-order correlation between the concentrations from the two sources would allow all the higher-order concentration moments (viz., higher than second order) for the total plume to be determined.

Chapter 5

Dispersion and Mixing of Plumes in Isotropic Turbulence

5.1 Introduction

In chapters 3 and 4, the dispersion and mixing of passive scalars in a wall-bounded shear flow have been studied. The physical processes associated with the interaction between two plumes are sensitive to many factors such as the source sizes, source separation, background turbulence level, Reynolds number, Schmidt number, turbulent eddy sizes (or spectra of eddy motions), and mean shear. In order to develop deeper physical insights into the interaction of two plumes, it is useful to study the problem in more idealized flows such as homogeneous isotropic turbulence which is characterized by the absence of mean shear.

Anand and Pope (1985) developed an analytical solution for the development of the mean plume spread in decaying homogeneous isotropic turbulence, using a marked particle (or, Lagrangian stochastic) model. In so doing, three distinct regimes of plume development have been identified: namely, the molecular diffusive, the turbulent convective and the turbulent diffusive regimes. According to Anand and Pope (1985), of the three regimes for plume dispersion, the turbulent convective regime is perhaps the most challenging to understand and to model. Currently, very few studies have focused on the elucidation and understanding of the characteristics of dispersion and mixing of plumes in the turbulent convective regime in the context of homogeneous isotropic turbulence. In view of this, the objective of this chapter is to investigate the phenomenon of dual plume interference in the turbulent convective regime associated with the release of passive scalars from two line sources in homogeneous isotropic turbulence.

5.2 Problem Description

In this chapter, DNS is performed to study the release of plumes from two line sources into homogeneous isotropic turbulence at a Reynolds number of $Re_\lambda = 150$. In order to generate a mean advection of the passive scalar in homogeneous isotropic turbulence, a constant mean streamwise velocity of $U = 5\hat{u}$ is superimposed on the velocity fluctuations obtained from the solution of the continuity and momentum equations. Here, $\hat{u}$ is the fluctuating velocity scale that is derived from the turbulence kinetic energy (TKE) k_u as $\hat{u}^2 = 2k_u/3$. Figure 5.1(a) shows a schematic of the computational domain, which is a cubic box with a side length of $L = 2\pi$. For the concentration field, a zero Dirichlet condition was applied at the inlet boundary (y-z plane located at $x = 0$), a zero Neumann condition was imposed at the outlet boundary (y-z plane located at $x = 2\pi$), and periodic boundary conditions were used at the other boundaries of the computational domain.

The two line sources labeled ‘A’ and ‘B’ in figure 5.1(a) are oriented along the spanwise direction and positioned symmetrically in the vertical direction with a separation distance d. The size (diameter) of the two line sources is equal to $0.021l$. Figure 5.1(b) exhibits a snapshot of the instantaneous concentration field in a vertical x-y plane when both line sources are active. In order to investigate the effect of source separation distance d on the mixing of the two plumes, five different test cases

Table 5.1: Summary of test cases.

Case	1	2	3	4	5
d/l	0.02	0.06	0.08	0.15	0.23

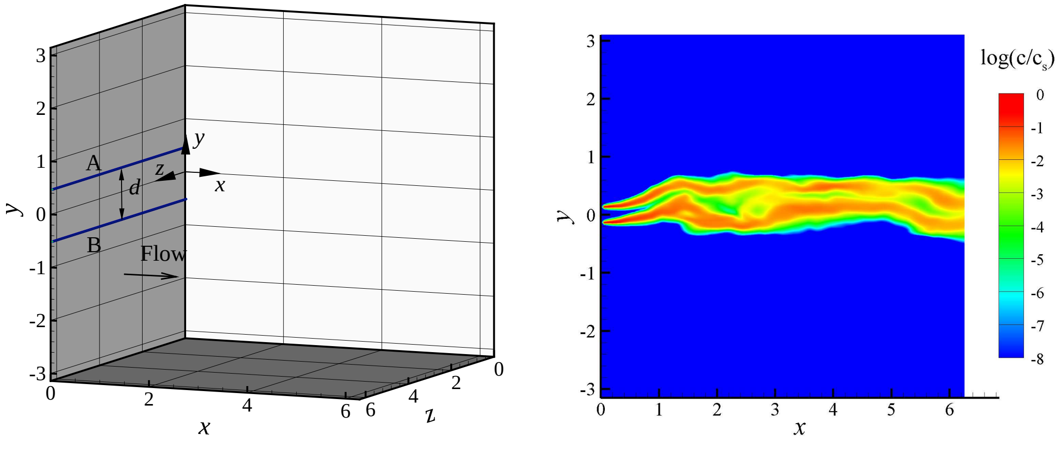

(a) (b)

Figure 5.1: (a) Schematic of the computational domain and (b) a snapshot of the instantaneous concentration field when both sources are active for case 4 at $z = \pi$. The two horizontal line sources positioned at A and B are separated in the y direction by a distance d.

are considered. Table 5.1 summarizes the non-dimensionalized source separation distances d/l used in these cases. For all these cases, the (molecular) Schmidt number (Sc) of the scalar is set to 1.0.

5.3 Result Analysis

In this section, the results of the five test cases are analyzed. These results include the velocity statistics, the mean and variance of the concentration field of the single and total plumes, the cross correlation coefficient of the two plumes, the co-spectrum and coherency spectrum of the two concentration fields, the concentration PDF, the concentration EDF and the higher-order concentration moments.

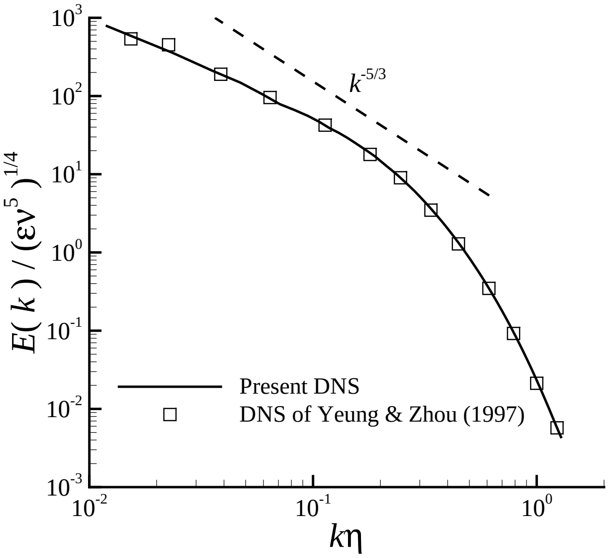

Figure 5.2: Velocity energy spectra from DNS.

5.3.1 Velocity Statistics

Because the dispersion and mixing of passive plumes are influenced by the fluid flow, it is necessary to verify the predicted velocity field prior to the analysis of the concentration field. Figure 5.2 compares the energy spectrum obtained from the present DNS with that obtained by Yeung and Zhou (1997). As shown in figure 5.2, the energy spectrum is in very good conformance with that obtained by Yeung and Zhou (1997). Furthermore, the well-known Kolmogorov $-5/3$ law for the form of the energy spectrum in the inertial subrange is shown as the dashed line in figure 5.2. Note that the wavenumber range corresponding to the inertial subrange for the energy spectrum is very limited (less than about 1/3 of a decade centered around $k\eta \approx 0.1$) owing to the low Re_λ value of the flow.

5.3.2 Mean Concentration

In this section, the results of the mean concentration plume(s) released from a single and from two sources are analyzed and compared.

5.3.2.1 Single Source

In homogeneous isotropic turbulence, the profile of the mean concentration C is expected to be Gaussian at any location downwind of a localized source (Uberoi and Corrsin, 1953; Townsend, 1954; Warhaft, 1984; Stapountzis et al., 1986). For example, the mean concentration profile in the y-direction at a fixed downwind location x from the source is expected to have the following functional form:

$$C(x,y) = C_m(x)\text{exp}\left(-\frac{1}{2}(y-y_s)^2/\sigma_a^2(x)\right). \tag{5.1}$$

Here, $C_m(x)$ is the maximum mean concentration at a given downwind location x, y_s is the elevation of the source, and $\sigma_a(x)$ is the mean (absolute) plume dispersion. The absolute dispersion $\sigma_a(x)$ can be determined from a least-squares fit of the Gaussian form of Eq. (5.1) to the mean concentration profiles obtained at various downwind distances x from the source.

Using Taylors's diffusion equation (1921) which recognizes turbulent diffusion as a continuous mixing process, the absolute dispersion σ_a in homogeneous isotropic turbulence is given by

$$\sigma_a^2 = 2\hat{u}_L^2[tt_L - t_L^2(1-\mathrm{e}^{-t/t_L})] \quad , \tag{5.2}$$

where $t = x/U$ is the travel time, t_L is the Lagrangian time scale and $\hat{u}_L$ is the Lagrangian velocity standard deviation. In order to use this formula, one needs an estimate for t_L and $\hat{u}_L$. In stationary homogeneous turbulence, the Lagrangian and Eulerian single-point velocity moments are equivalent (Lumley (1962)), implying that $\hat{u}_L = \hat{u}$. The Lagrangian time scale is assumed proportional to the Eulerian length scale of turbulence so

$$t_L = \beta\lambda/\hat{u}_L \quad , \tag{5.3}$$

with $\beta \approx 0.35 - 0.8$ (Pasquill and Smith (1983)). Using the lower limit of $\beta = 0.35$, the Lagrangian time scale can be evaluated as $t_L = 1.88$. In figure 5.3, the mean plume dispersion obtained from our DNS results and that predicted using Taylor's

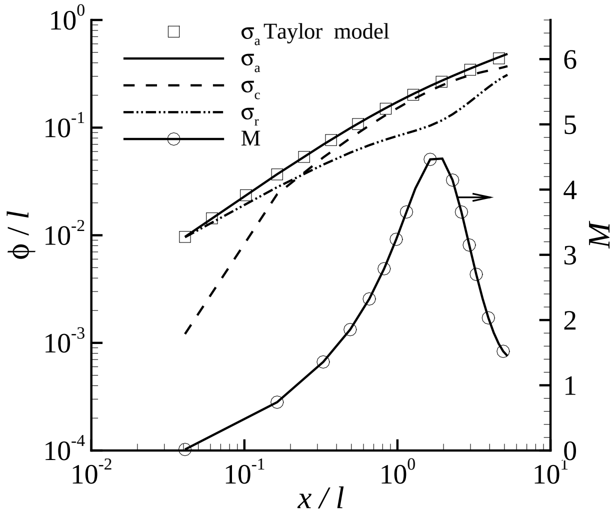

Figure 5.3: Streamwise development of the mean plume dispersion σ_a, the dispersion of the center of instantaneous plume σ_c, the relative plume dispersion σ_r and the meander ratio ($M = \sigma_c^2/\sigma_r^2$). Here, ϕ represent σ_a, σ_r or σ_c.

diffusion equation (equation 5.2) are shown by the solid line and (□) symbols, respectively. The agreement between these two results for the absolute dispersion is very good. The streamwise development of the relative plume dispersion σ_r, the dispersion of the instantaneous plume centroid σ_c and the meander ratio ($M = \sigma_c^2/\sigma_r^2$) are also shown in figure 5.3. It is evident from this figure that the bulk meandering of the instantaneous plume is the dominant mechanism for the mean plume dispersion ($\sigma_c > \sigma_r$, or equivalently, $M > 1$) over the downwind fetches available in the DNS data provided $x/l > 0.22$. This range of downwind distances is associated with the turbulent convective regime of plume development.

5.3.2.2 Two Sources

The streamwise development of the profiles of the total mean concentration C_T for cases 1–5 is shown in figure 5.4. In this figure, the total mean concentration has been non-dimensionalized by the corresponding maximum mean concentration $C_{T,\mathrm{m}}$ at a given downwind location. The total mean concentration C_T for the two sources is simply the linear superposition of the two individual mean concentrations. As shown in figure 5.4(a), for large source separations (e.g., cases 3-5), the total mean concentration profiles exhibit a dual-peak pattern at downstream locations close to the source (for $x/l = 0.5$). Furthermore, the y positions of the two peaks in these profiles coincide with the locations of the two sources at $y/l = \pm d/(2l)$. However, as the downwind distance increases, the dual-peak pattern transitions to a single-peak pattern. This transition is due to the fact that at far downstream locations from the sources, the spread of the two plumes is significant enough that their individual peaks begin to merge.

5.3.3 Variance of Concentration Fluctuations

In this section, the results of the variance of concentration fluctuations of the plumes released from two sources are compared against those from the single source release.

5.3.3.1 Single Source

Figure 5.5 shows profiles of the concentration variance $\overline{c'^2}(x, y)$ at four downstream locations for a single source. The concentration variance is non-dimensionalized by the centerline value $\overline{c_c'^2}$ at the given downstream location x. At all downstream locations, the concentration variance profiles exhibit a single peak at the plume centerline. As shown and discussed previously in chapters 3 and 4, strong meandering motions of a plume can lead to the obliteration of the off-centerline peaks in the profiles of $\overline{c'^2}$. At all downstream locations shown in figure 5.5, the plume is in the turbulent convective regime of its development (meander dominant regime). The dominant bulk meandering of the plume in the turbulent convective regime smears the off-axis maxima in the concentration variance profile. In consequence, the maximum in the concentration variance profile occurs at the mean-plume centerline as is evident in figure 5.5.

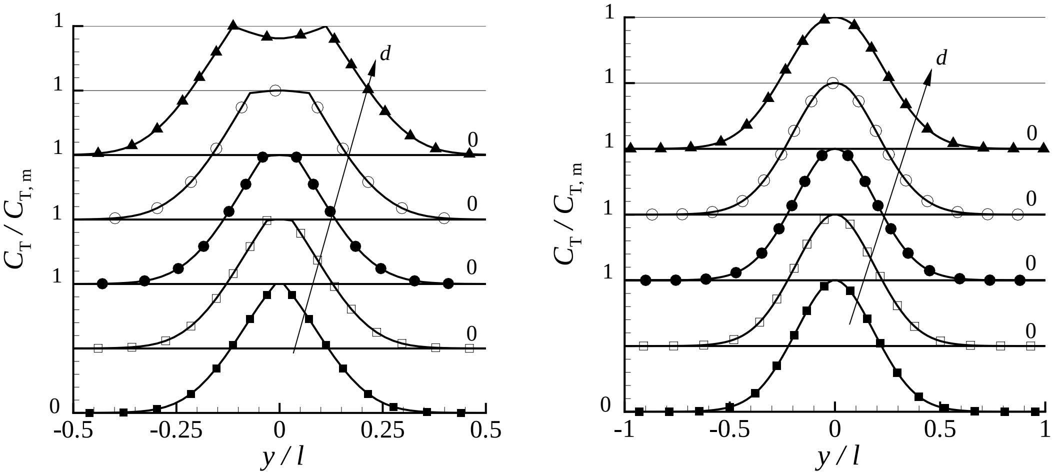

(a) $x/l = 0.5$ (b) $x/l = 1.0$

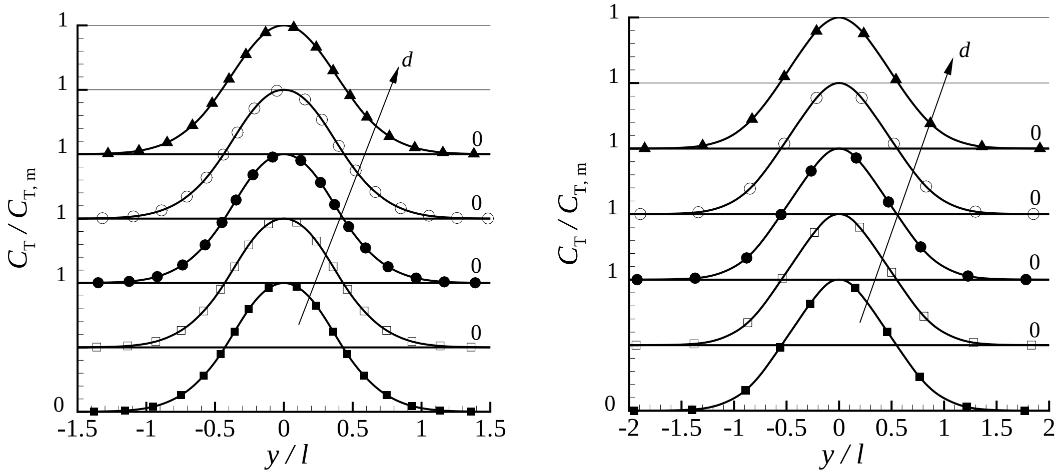

(c) $x/l = 3.0$ (d) $x/l = 5.0$

Figure 5.4: Profiles of the total mean concentration at four different downwind locations. Cases 1 (■), 2 (□), 3 (●), 4 (○), and 5 (▲). The arrow points towards increasing values of d.

5.3.3.2 Two Sources

In subsection 5.3.3.1, it is shown that the strong meandering of a single plume obliterates (to a greater or lesser extent depending on the strength of the meandering) the off-axis peaks in the concentration variance profiles, resulting in a single peak along the centerline of each plume. Similarly, in the context of dual plume dispersion, the strong meandering effects "smears out" the off-axis peaks in the total concentration variance profile, leading to a single peak located at the midpoint between the two sources. This smearing (by meandering) is the most strongly expressed if the source separation is small and the downwind distance from the sources is large. This hypothesis has been shown previously, in chapters 3 and 4, to be valid for the dispersion and mixing of ground-level and elevated plumes in wall-bounded shear flow. In order to further examine this hypothesis in homogeneous isotropic turbulence, figure 5.6 exhibits the profiles of the total concentration variance ($\overline{c_T'^2}$) for cases 1 and 5 (which correspond, respectively, to the smallest and largest separation between the sources) at four downwind locations. The total concentration variance has been non-dimensionalized by the maximum value ($\overline{c_{T,m}'^2}$) at a given downwind location. As is evident in figure 5.6, for case 1 (which is associated with the smallest source separation) all the concentration variance profiles exhibit a single peak at the midpoint between the two sources (viz., at $y/l = 0$). In contrast, in case 5 (which is associated with the largest source separation) the total concentration variance profiles at downwind fetches closer to the two sources (e.g., at $x/l = 0.5$ and 1) exhibit a dual peak pattern. Obviously, owing to the large source separation of case 5, the individual peak of each single plume is preserved in the profile of $\overline{c_T'^2}$ along each mean-plume centreline in the near-source region. However, further downwind of the sources (at $x/l = 3$ and 5), the individual peaks associated with the two plumes merge together as the width of each plume increases to such an extent that the two plumes begin to overlap significantly.

In the following subsections, the characteristics of the covariance of the concentration fluctuations of two instantaneous plumes will be examined using the cross correlation coefficient, the concentration co-spectrum and coherency spectrum. The effect of the non-dimensionalized covariance (cross correlation coefficient) on the EDF of the total plume concentration will be also investigated.

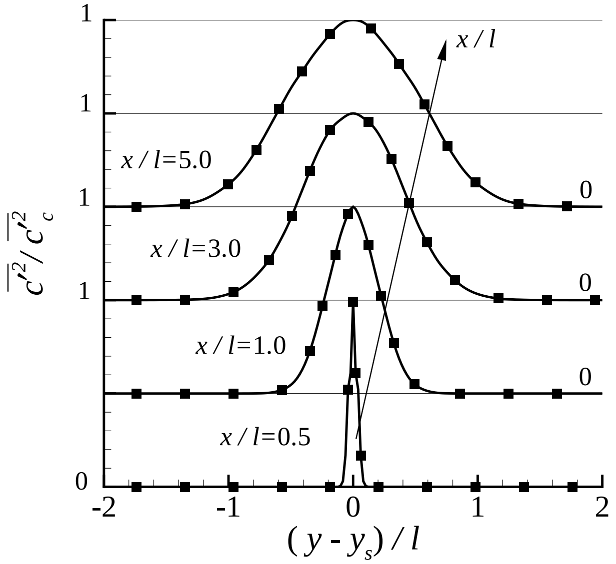

Figure 5.5: Concentration variance profile of a single plume at four downwind locations from the source.

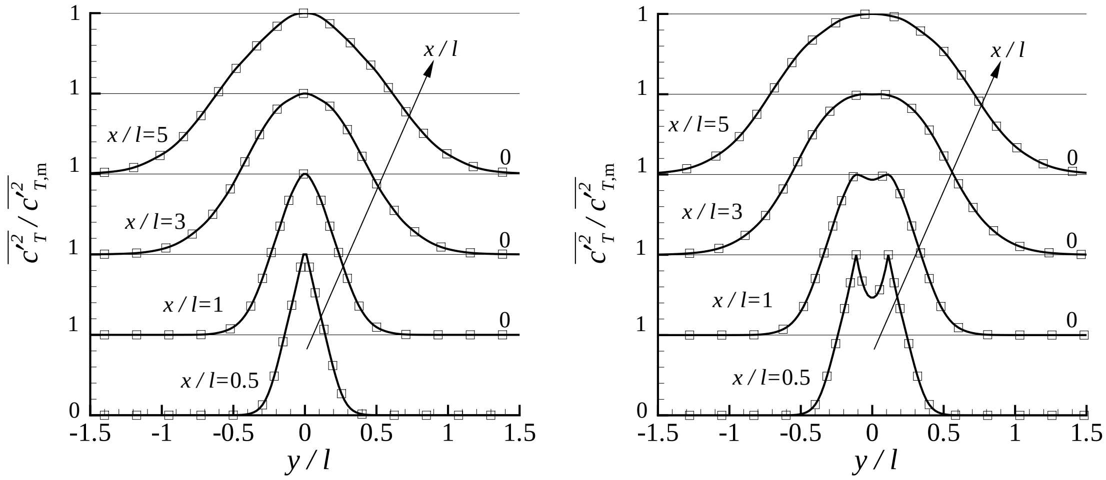

(a) Case 1

(b) Case 5

Figure 5.6: Profiles of the concentration variance at four downstream locations for the two source configuration. The arrow points in the direction of increasing downwind location x/l.

5.3.4 Cross Correlation Coefficient

Figure 5.7 exhibits the streamwise development of the (concentration) cross correlation along the midpoint ($y = 0$) between the two sources for cases 1-5. Similar to

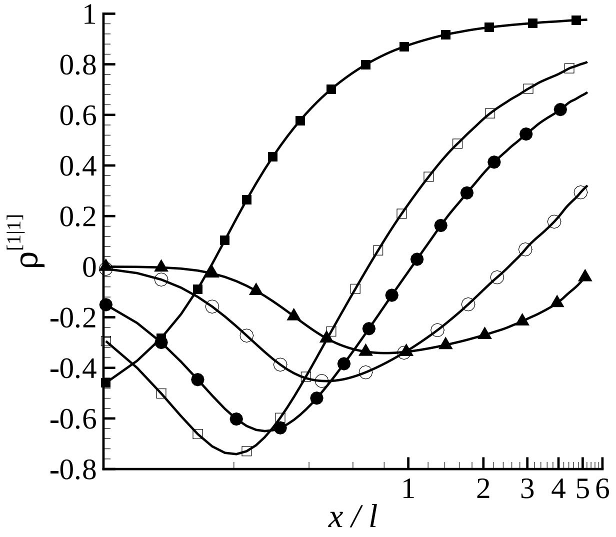

Figure 5.7: Streamwise variation of the cross correlation $\rho^{[1|1]}$ at the midpoint ($y = 0$) between the two sources. Cases 1 (■), 2 (□), 3 (●), 4 (○), and 5 (▲).

the observation in chapters 3 and 4 in the context of a wall-bounded turbulent shear flow, the streamwise evolution of the cross correlation in this chapter (homogeneous isotropic turbulent flow) at the midpoint between the two plumes can be categorized into the four stages of (1) the zero interference stage where $\rho^{[1|1]} = 0$, (2) the destructive interference stage where $\rho^{[1|1]} < 0$, (3) the constructive interference stage where $\rho^{[1|1]} \geq 0$, and (4) the complete mixing state where $\rho^{[1|1]} \to 1$.

Figure 5.8 compares profiles of $\rho^{[1|1]}$ in the y-direction for cases 1-5 at four downwind locations. It is clearly seen that for all cases and at all downstream locations, the local minimum value of $\rho^{[1|1]}$ occurs midway between the two plumes (at $y = 0$), and the local maximum values occur at the plume fringes where the plume intermittency is large. The cross correlation decreases towards zero at the extreme outer edges of the two plumes. A perusal of figures 5.8(a)-(d) shows that $\rho^{[1|1]} \to 1$ approaches the asymptotic value of unity faster at the fringes (edges) of the total plume than at a point midway between the two plumes. At the midpoint between the sources, a large eddy tends to transport the plume from one source over this location while simultaneously moving the plume from the other source off this location (resulting

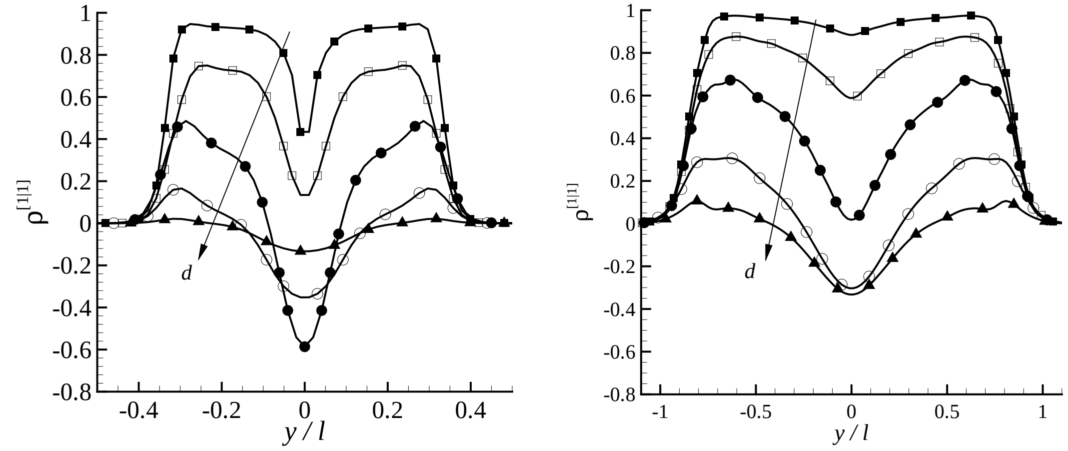

(a) $x/l = 0.3$

(b) $x/l = 1.0$

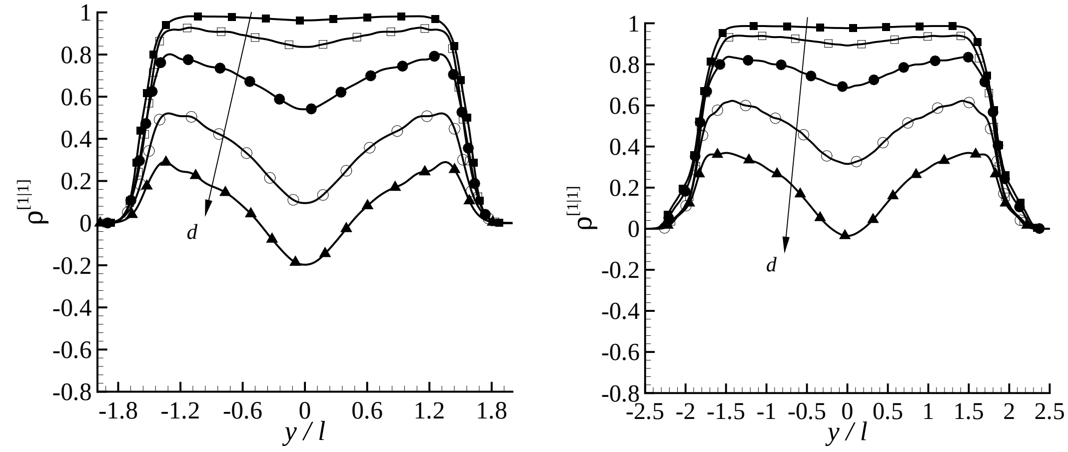

(c) $x/l = 3.0$

(d) $x/l = 5.0$

Figure 5.8: Profiles of the cross correlation in the y-direction. Cases 1 (■), 2 (□), 3 (●), 4 (○), and 5 (▲). The arrow points in the direction of increasing values of d.

in out-of-phase fluctuations). However, at the plume fringes, a large eddy can occasionally transport both plumes to or from these locations simultaneously (resulting in in-phase fluctuations). The out-of-phase fluctuations reduces the value of $\rho^{[1|1]}$ at a location midway between the two plumes compared to the in phase fluctuations at the plume fringes.

5.3.5 Concentration Co-spectrum and Coherency Spectrum

Following the approach used in sections 3.3.5 and 4.3.4, in order to develop deeper insights into the dispersion and mixing of two plumes, it is beneficial to study the relevant scales of mixing using the co-spectrum $Co_{c'_A c'_B}(k_z)$ and coherency spectrum $\rho_{k_z}^{[1|1]}$. The streamwise evolution of the pre-multiplied co-spectrum and the coherency spectrum obtained at the midpoint between the two sources for cases 1 and 5 are shown in figures 5.9 and 5.10, respectively. Here, only $Co_{c'_A c'_B}(k_z)$ and $\rho_{k_z}^{[1|1]}$ for cases 1 and 5 are presented, because these two cases correspond to the smallest and largest source separations, respectively, and together they cover the widest range of values for $\rho^{[1|1]}$ (as shown in figure 5.7).

A comparison between the streamwise evolution of the pre-multiplied co-spectrum in the context of homogeneous isotropic turbulence (figure 5.7) with that of a wall-bounded turbulent shear flow (figures 3.14 and 4.18(a)) reveals that they share some common features. The aforementioned four distinct stages in the streamwise development of the cross correlation can be also observed in the streamwise evolution of the pre-multiplied co-spectrum and the coherency spectrum.

In the first (zero interference) stage, because a sensor at the measurement location is not exposed to the instantaneous concentrations from both plumes simultaneously (viz., the instantaneous plumes do not overlap), the pre-multiplied co-spectrum vanishes at all scales. This is clearly seen in figure 5.9(b) for case 5 at $x/l = 0.15$. In the second (destructive interference) stage, the bulk meandering of the two plumes in the same direction gives rise to a negative spectral peak for the pre-multiplied co-spectrum at large scales (small wavenumber). The value of the cross correlation (which is the integral of the co-spectrum over all wavenumbers) is primarily determined by these scales. Therefore, these scales represent the most energetic scales in the interference of the two plumes. The existence of the second stage of development is evidenced by case 5 for $x/l = 0.5$ and 2 in figure 5.9(b). Furthermore, as indicated by the peaks of the pre-multiplied co-spectra in figure 5.9, the most energetic

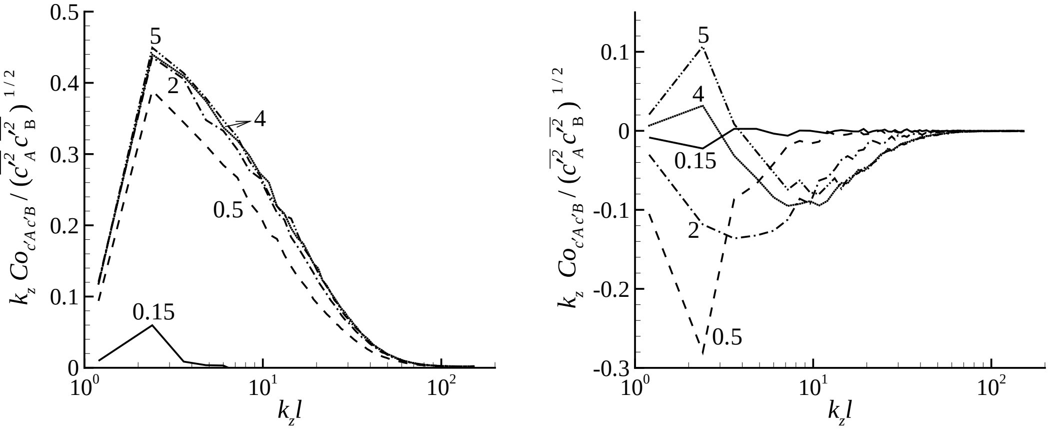

(a) Case 1

(b) Case 5

Figure 5.9: The pre-multiplied co-spectrum of the concentration of the two plumes for (a) case 1 and (b) case 5 obtained at the midpoint location between the two sources ($y = 0$), for $x/l = 0.15$ (solid line), 0.5 (dashed line), 2 (dash-dotted line), 4 (dotted line) and 5 (dash-dot-dotted line).

scales in the interference of the two plumes occur within the range of wavenumbers for $2 < k_z l < 4$ at all downwind distances examined.

In the third (constructive interference) stage, the meandering of the two plumes in opposite directions leads to a positive spectral peak in the pre-multiplied co-spectrum. The wavenumber of this peak is expected to be small because the bulk meandering is a large-scale phenomenon. The characteristics of the third stage are evident in figure 5.9(a) at $x/l = 0.15$ and 0.5. In the fourth (complete mixing) stage where the cross correlation reaches its maximum value of unity, the pre-multiplied co-spectrum reaches its final form and is expected to be invariant with increasing downwind distance. The characteristics of this stage are evident in figure 5.9(a) for case 1 (associated with the smallest source separation). Note that the co-spectrum for this case is invariant (approximately or better) for x/l increasing from 2 to 5.

Following the method of analysis in sections 3.3.5 and 4.3.4, the leading scales in the mixing of the two plumes are identified and labeled in figure 5.10. The leading scales are referred to those scales in which the coherency spectrum develops faster than at other scales. The coherency spectrum $\rho^{[1|1]}_{k_z}$ at the leading scales can reach its

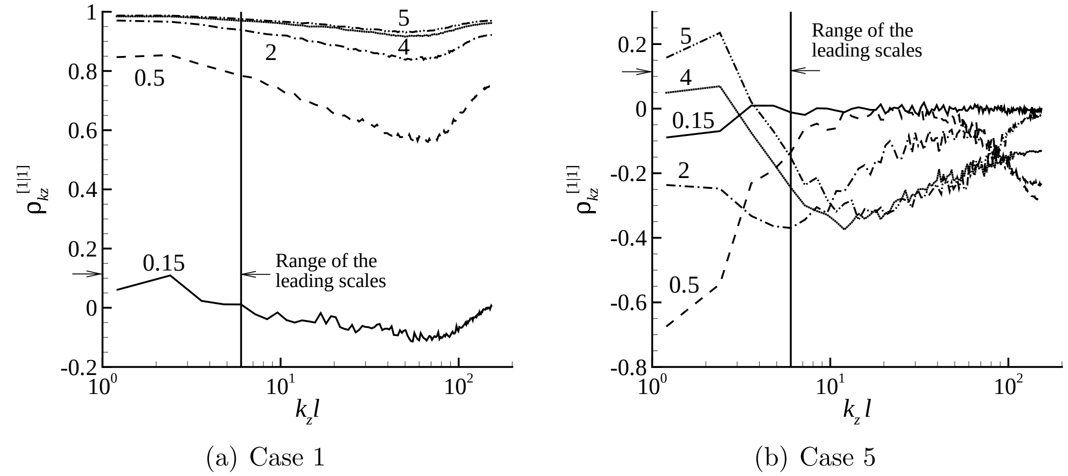

(a) Case 1

(b) Case 5

Figure 5.10: The coherency spectrum $\rho_{k_z}^{[1|1]}$ of the concentration of the two plumes for (a) case 1 and (b) case 5 obtained at the midpoint between the two sources, for $x/l = 0.15$ (solid line), 0.5 (dashed line), 2 (dash-dotted line), 4 (dotted line) and 5 (dash-dot-dotted line).

asymptotic value of unity faster than any other scales. As shown in the figure, the leading scales of the test cases considered in this chapter are located at large scales (small wavenumbers). This further confirms that the rate of mixing of two plumes leads at large and small scales in the turbulent convective and turbulent diffusive regimes, respectively. The reason that the mixing of the two plumes leads at large scales in the turbulent convective regime can be attributed to the plume meandering which is a large scale phenomenon. In contrast, the mixing of the two plumes leads at small scales in the turbulent diffusive regime. This is because the internal turbulent mixing, which is a small-scale phenomenon, provides the primary contribution to the dual plume mixing process.

5.3.6 Concentration PDF and EDF

In this subsection, a brief discussion on the concentration PDF of the single plume is presented, followed by a detailed analysis of the effects of plume interference on the concentration EDF of the total plume.

5.3.6.1 Concentration PDF of the single plume

Figure 5.11 compares the concentration PDF (i.e., $f(\chi/C)$) along the mean plume centerline at five downwind distances from the source. This figure shows that the concentration PDF is almost an exponential-like form at all downstream locations shown. It is also seen that the mode of zero concentration along the plume centerline is predominant, indicating that the measurement location is exposed to the clean fluid for most of the time. In order to understand the streamwise development of the PDF, the mode of zero concentration $f(0)$ is singled out and plotted using a sub-panel in figure 5.11. As is clear from this sub-panel figure, the value of $f(0)$ first increases as x/l increases from 0.5 to 2, and then decreases in the downwind distance from the sources. This trend in the streamwise evolution of zero concentration is similar to that of the meandering ratio M shown in figure 5.3. When the thin instantaneous plume passes over the measurement location, the concentration level increases drastically for a short period of time, and then the measurement location is exposed to the clean fluid until the instantaneous plume passes over this location again. For a large meandering ratio, the time in which the measurement location is exposed to the clean fluid is long, which increases the probability of zero concentration along the mean plume centerline.

Figure 5.12 compares the distributions of the concentration PDF at four vertical positions at the same downwind location for $x/l = 1$. As is evident form the figure, as vertical distance from the mean plume centerline increases from $y/l = 0$ to 0.14, the mode of zero concentration increases dramatically. In order to highlight this physical feature, the vertical distribution of the mode of zero concentration $f(0)$ is displayed using sub-pannel. This is similar to the results shown in figure 4.20 for the ground-level and elevated plumes.

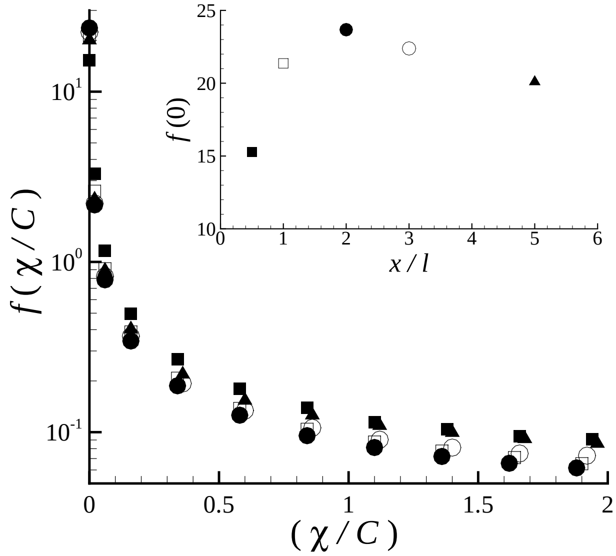

Figure 5.11: Concentration PDF along the mean plume centerline at the normalized downwind fetches from the source for $x/l = 0.5$ (■), 1 (□), 2 (●), 3 (○) and 5 (▲).

5.3.6.2 Cross correlation effect on concentration EDF of the total plume

Figure 5.13 shows the concentration EDF at various streamwise locations at the midpoint ($y = 0$) between the two sources for case 5. In order to understand the effects of dual plume interference, the concentration EDF for a single source is also displayed in figure 5.13 for the purpose of comparison. The concentration EDFs in this figure clearly reveal that the probability of exceeding a high concentration level (above twice the mean concentration $\chi/C > 2$) for two sources is smaller than that for a single source. In other words, the upper tail of the EDF for the total concentration from the two sources is shorter than that for a single source. Similar results are also observed for cases 1–4.

This observation is consistent with the results obtained in the wall-bounded shear flow presented in section 4.3.5.2. However, in the context of the wall-bounded shear flow, it is observed that the cross-over point in the concentration EDF for the dual and single sources occurs at $\chi/C > 1$, rather than at $\chi/C > 2$ as observed in the context of homogeneous isotropic turbulence. This difference can be attributed to

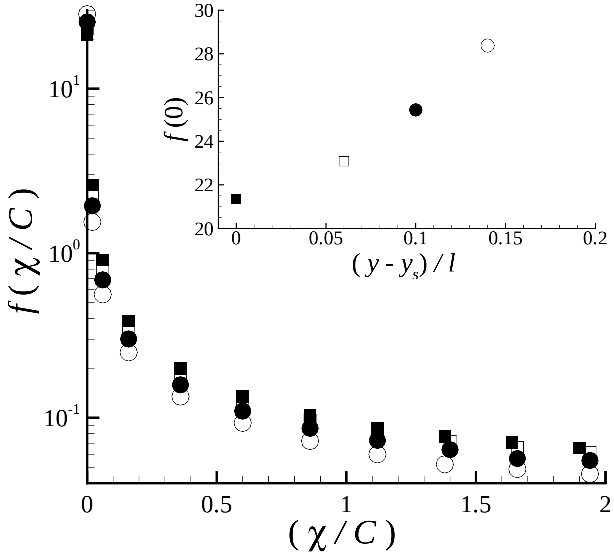

Figure 5.12: Concentration PDF at the downwind fetch of $x/l = 1$ at four vertical locations from the mean plume centerline for $(y - y_s/l) = 0$ (■), 0.06 (□), 0.1 (●) and 0.14 (○).

the absence of the mean shear in the homogeneous isotropic turbulence. The effect of mean shear on the concentration field is to increase the mixing and the rate of decay of scalar fluctuations, which results in a shorter upper tail in the concentration EDF for dispersion in a sheared flow compared to that in a shearless flow.

In order to quantify the reduction in the exceedance probability across high concentration levels (e.g., for $\chi/C > 2$) for the two source release in comparison to the single source release, the reduction factor (RF) is calculated for cases 1-5. Figure 5.14 shows the RF plotted against the concentration level (χ/C) for cases 1-5. This figure reveals that for a concentration level above twice the mean value, RF is larger than one (i.e., RF(χ/C $> 2) > 1$), and for a concentration level below twice the mean value, RF is smaller than one (i.e., RF(χ/C $< 2) < 1$) for all cases and at all downstream locations tested. This implies that the probability for exceeding a concentration level that is more than twice the mean concentration is larger for the single source release than for the release from two sources. From figures 5.13 and 5.14, it is clear that the opposite condition holds for concentration levels less than twice the mean con-

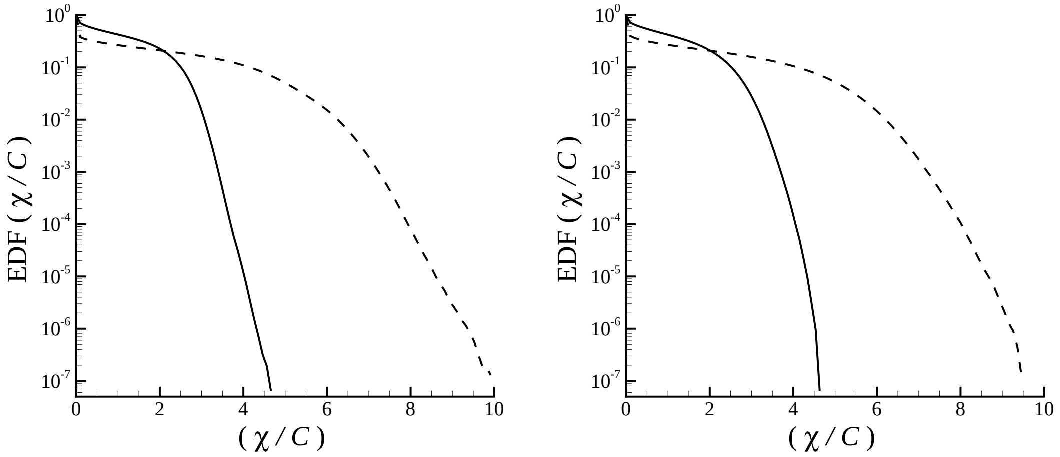

(a) $x/l = 0.5$ (b) $x/l = 1.0$

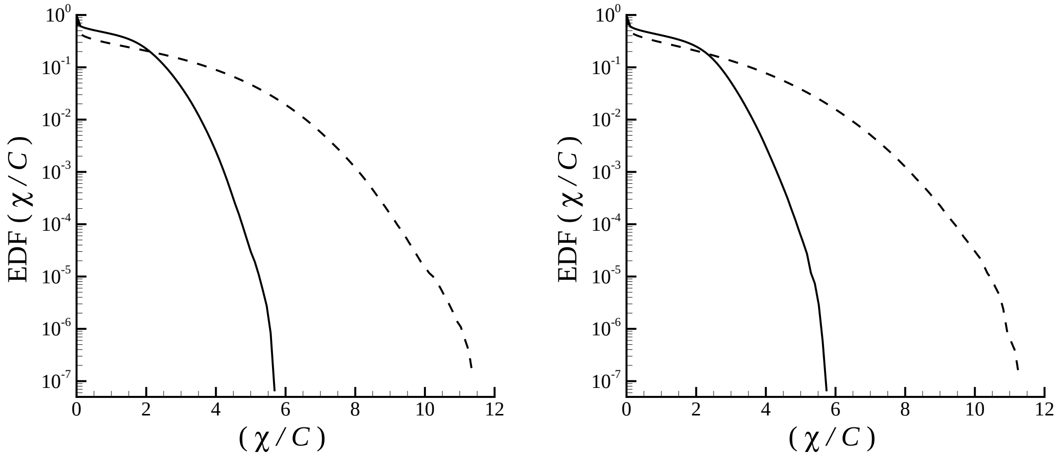

(c) $x/l = 3.0$ (d) $x/l = 5.0$

Figure 5.13: Concentration EDF of the total plume (solid line) and a single plume (dashed line) for case 5 at the midpoint ($y = 0$) between the two sources at various downwind distances.

centration. Another interesting physical feature observed from figure 5.14 is that RF increases monotonically with the concentration level for $\chi/C > 2$. This indicates that the difference between the probability of observing a high concentration in the dual and single source increases as the concentration level increases.

A careful comparison of figure 5.7 with figure 5.14 reveals that there seems to be a negative correlation between RF($\chi/C > 2$) and $\rho^{[1|1]}$. In another words, increases in RF($\chi/C > 2$) are associated with decreases in $\rho^{[1|1]}$ and vice-versa. In order to

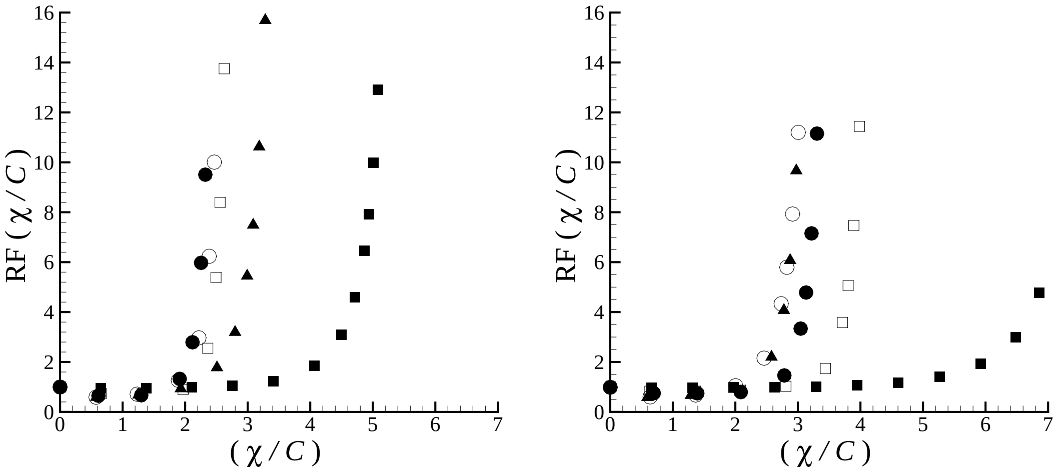

(a) $x/l = 0.5$ (b) $x/l = 1.0$

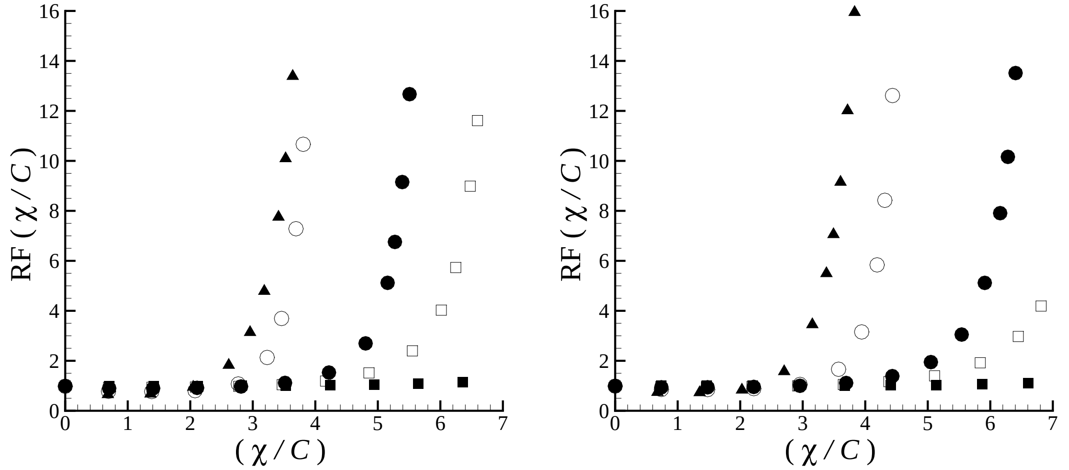

(c) $x/l = 3.0$ (d) $x/l = 5.0$

Figure 5.14: RF for cases 1 (■), 2 (□), 3 (●), 4 (○), and 5 (▲) as a function of the non-dimensionalized concentration level χ/C. These results were obtained at $y = 0$ (which for the two source release corresponds to the midpoint between these sources).

examine the possible correlation between RF($\chi/C > 2$) and $\rho^{[1|1]}$, figure 5.15 displays scatterplots of RF against $\rho^{[1|1]}$ for four different concentration levels above twice the mean concentration. This figure clearly shows that $\rho^{[1|1]} < 0$ (corresponding to destructive interference) is associated with values of RF($\chi/C > 2$) that are significantly larger than unity, whereas $\rho^{[1|1]} > 0$ (corresponding to constructive interference) is associated with values of RF($\chi/C > 2$) that are comparable to unity. The negative

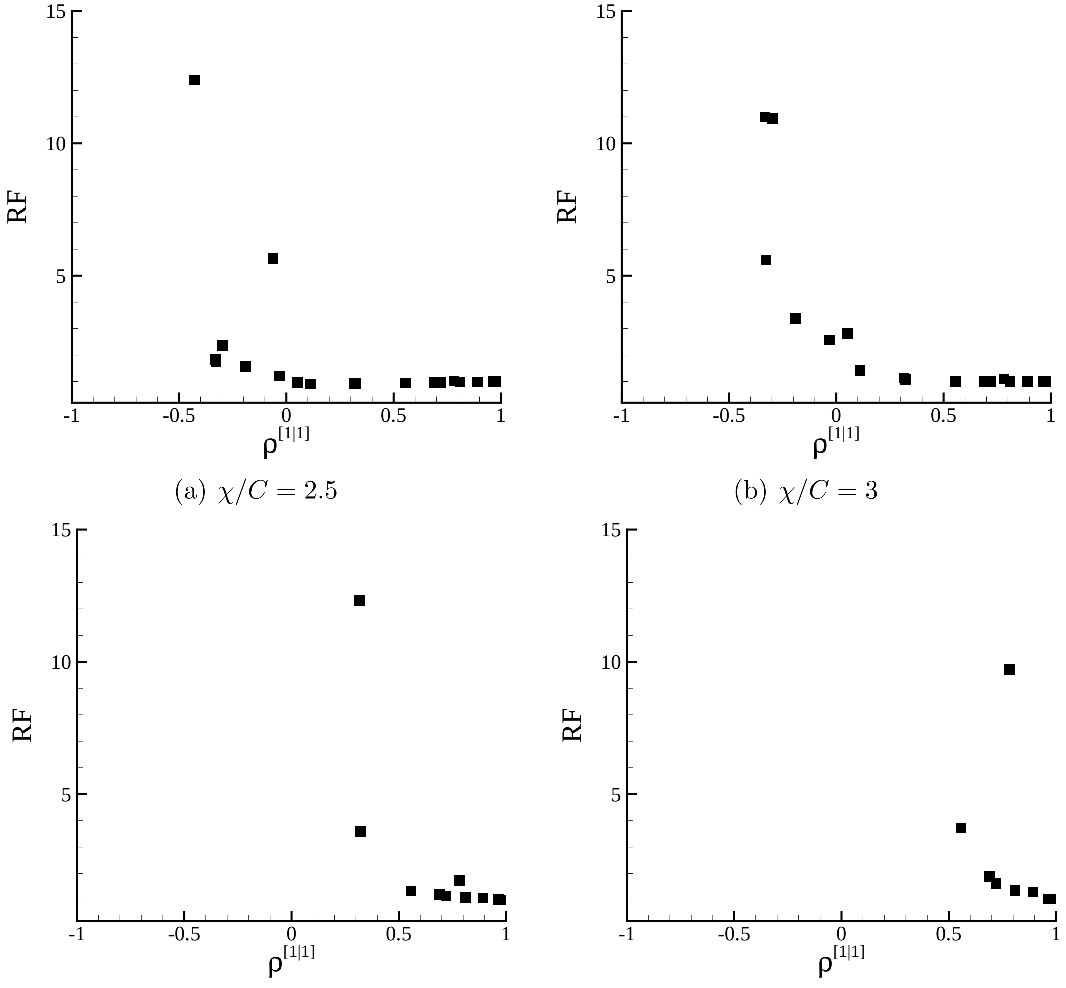

(a) $\chi/C = 2.5$ (b) $\chi/C = 3$

(c) $\chi/C = 4$ (d) $\chi/C = 5$

Figure 5.15: Scatterplots of RF against $\rho^{[1|1]}$ obtained at various downstream locations at the midpoint between the two sources.

correlation between RF and $\rho^{[1|1]}$ in the context of a wall-bounded shear flow is also observed and explained in section 4.3.5.2.

5.3.7 Higher-Order Concentration Moments

Figure 5.16 shows the normalized concentration moment scatterplots of $\overline{c^3}/C^3$ and $\overline{c^4}/C^4$ plotted against $\overline{c^2}/C^2$ on a double logarithmic scale for a large number of points in the total plume of cases 1-5. Similar to the observation in section 4.3.6, these

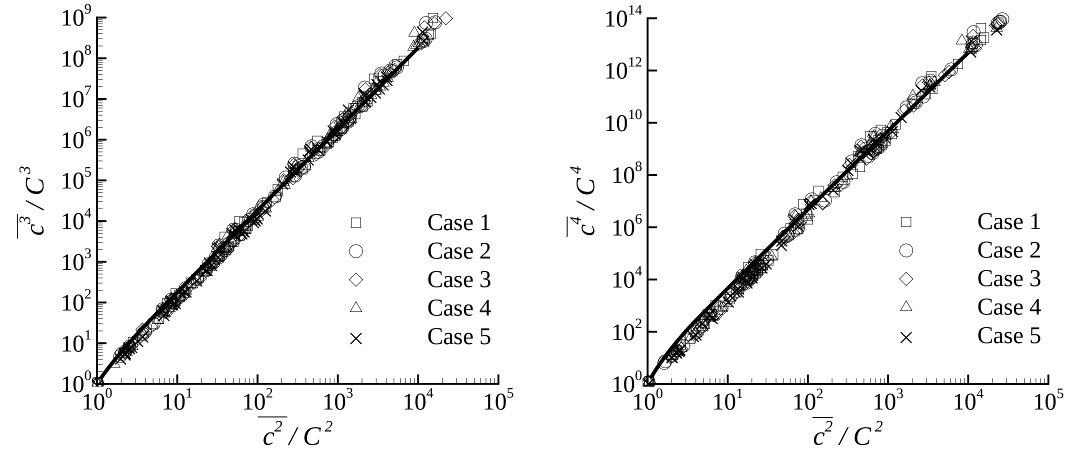

(a) third-order concentration moments (b) fourth-order concentration moments

Figure 5.16: Scatterplots of the normalized third- and fourth-order concentration moments plotted against the normalized second-order concentration moment for a large number of locations in the plume. The prediction of the relationship between these moments provided by the clipped-gamma distribution model (solid line) is superimposed on the scatterplot.

scatterplots collapse onto a curve implying that the normalized third- and fourth-order concentration moments are determined effectively by a knowledge of the first- and the second-order concentration moments.

Following the method of analysis used in section 4.3.6, the clipped-gamma distribution model of Yee and Chan (1997) (originally developed for a single plume) is implemented here to predict the normalized third- and fourth-order concentration moments for the total plume. The results are demonstrated in figure 5.16 using solid lines. From the figure, it is seen that the clipped-gamma distribution provides very good predictions for the higher-order concentration moments of the total plume in the context of homogeneous isotropic turbulence. This further confirms the universality of the clipped-gamma distribution model of Yee and Chan (1997), which works well for both single and dual plume releases.

5.4 Chapter Summary

The dispersion and mixing of plumes released from two line sources into homogeneous isotropic turbulent flow are studied using DNS. Specifically, the research focuses on the characteristics of the dispersion and mixing in the turbulent convective regime where the meandering of the instantaneous plumes provides the primary contribution to the mean plume dispersion and concentration fluctuations. Five test cases with various source separation distances are considered. In order to provide a deeper insight into the physics of the interaction of two plumes, the concentration cross correlation coefficient, the concentration co-spectrum and coherency spectrum, the concentration PDF and EDF and the higher-order concentration moments have been studied.

Similar to the observation in chapters 3 and 4 in the context of a neutrally-stratified wall-bounded shear flow, the streamwise evolution of the cross correlation ($\rho^{[1|1]}$) of the concentration from the two sources exhibited four stages of development: (1) the zero interference stage where $\rho^{[1|1]} = 0$, (2) the destructive interference stage where $\rho^{[1|1]} < 0$, (3) the constructive interference stage where $\rho^{[1|1]} \geq 0$, and (4) the complete mixing state where $\rho^{[1|1]} \to 1$. A smaller source separation is associated with a more rapid streamwise evolution of the cross correlation coefficient (viz., with a more rapid transition of $\rho^{[1|1]}$ through the four stages of development).

The four stages in the evolution of the cross correlation are also observed in the streamwise development of the pre-multiplied co-spectrum and the coherency spectrum. The peak of the pre-multiplied co-spectrum is located at low wavenumbers (corresponding to large scales), indicating that the large-scale turbulent eddies play a major contribution in the interaction of the two plumes. Furthermore, the coherency spectrum is found to evolve faster over a range of low wavenumbers that are associated with the 'leading scales' (the interaction of the two plume occurs first for these scales). Results of the pre-multiplied co-spectrum and the coherency spectrum suggest that the interaction between the two plumes is strongest and fastest at the large scales for the turbulent convective regime of development.

A comparison between the concentration EDF for two sources and a single source showed that the probability of exceeding a high concentration level is smaller for two sources than for a single source. In order to quantify the reduction in the exceedance probability of a high concentration level in the total plume compared to that in the single plume, a reduction factor (RF) is defined. Scatterplots of RF against $\rho^{[1|1]}$ clearly revealed that a negative value for the cross correlation (destructive interference) is associated with large values for RF. In contrast, as the cross correlation coefficient becomes increasingly positively valued (constructive interference), the RF is reduced in value towards unity (approaching unity exactly as $\rho^{[1|1]} \to 1$). This implies that the occurrence of high concentration level for the total plume is as frequent as that for a single plume.

Similar to the observation for the plume dispersion in a wall-bounded shear flow in chapter 4, the scatterplots of the normalized third- and fourth-order concentration moments against the normalized second-order concentration moment for the total plume, collapse onto a single curve. Furthermore, it is observed that the relationships between the various higher-order normalized concentration moments for the total plume can be adequately modeled using a clipped-gamma distribution. This implies that a knowledge of the first- and second-order concentration moments for each plume along with the cross correlation is sufficient for the prediction of all the higher-order moments of the total concentration.

Chapter 6

Conclusions and Future Work

6.1 Conclusions

In this section, the major conclusions of this research are summarized, which include development of two computer codes, summary of the testing parameters and numerical simulations, characteristics of a single plume dispersion and major findings of dual plume dispersion and mixing.

6.1.1 Computer Codes

Two different in-house codes implemented in FORTRAN 90/95 programming language and fully-parallelized using the message passing interface library have been modified, validated and optimized for this research.

In the first code, a fully conservative and fully implicit finite difference discretization scheme that utilizes a staggered grid arrangement is used for DNS of plumes dispersion and mixing in the turbulent open-channel flow. In this code, which is an extended version of a computer code developed by LePoudre (2003), the second-order energy-conserving finite difference scheme of Ham et al. (2002) is employed for discretizing the continuity and momentum transport equations. The four-step fractional step method of Choi and Moin (1994) coupled with the second-order Crank-Nicolson scheme is used to advance the velocity field over a single time step. A Crank-Nicolson scheme and a central-differencing scheme are used for the time advancement and spatial discretization of the diffusion term in the advection-diffusion equation, respectively.

During this research, it is found that the instantaneous concentration field is sensitive to the discretization scheme of the convective term, and negatively-valued concentration may occur if a second-order central differencing scheme is used for the discretization of the convective term in the advection-diffusion equation. In order to avoid non-physical oscillations in the solution of the concentration field, the original code of LePoudre (2003) is updated to incorporate a total variation diminishing (TVD) scheme with the Sharp and Monotonic Algorithm for Realistic Transport (SMART) limiter function of Gaskell and Lau (1988) for the discretization of the convective term.

Prior to the simulation of the passive scalar dispersion problem, it is important to ensure that the velocity field has been correctly predicted. It has been demonstrated that there is a good agreement between the flow statistics (mean velocity, RMS velocities and Reynolds shear stress) obtained from the open-channel code and those reported in the literature.

In the second code, a pseudo-spectral method described by Orszag and Patterson (1972) and Eswaran and Pope (1988) is used for DNS of plumes dispersion and mixing in homogeneous isotropic turbulent flow. In this code, the velocity and pressure fluctuations are expanded into Fourier series in all three coordinate directions. The convection terms in the momentum transport equation are calculated in physical space, and the aliasing error has been removed using the 3/2 rule. In order to generate a mean advection of the passive scalar, a constant mean streamwise velocity is superimposed on the velocity fluctuations obtained from the solution of the continuity and momentum equations. A similar algorithm to that used in the open-channel code is employed for the solution of advection-diffusion equation with a difference that the time advancement for both the velocity and scalar fields in homogeneous isotropic turbulence code has been achieved using the explicit fourth-order Runge-Kutta scheme. Through the validations, it has been confirmed that isotropic turbulence field can be well reproduced by this computer code, as the predicted energy spectrum is in good agreement with that reported in the literature.

6.1.2 Testing Parameters and Numerical Simulations

For the open-channel flow configuration, the source separation distance is varied from 5% to 50% of the channel height. Two Reynolds numbers of 180 and 395 based on the friction velocity are considered. In order to study the effect of wall shear on the dispersion and mixing of plumes, the sources are located at two different elevations. They are either located in the viscous sublayer or in the log-law region from the solid wall, corresponding to a pair of near ground-level or elevated sources, respectively.

For the homogeneous isotropic turbulence, five test cases with different source separation distance are considered, which are varied from 2% to 20% of the integral length scale of the flow. The Reynolds number based on the Taylor microscale of the flow is set to 150.

All numerical simulations have been conducted using the WestGrid high performance computing facilities. The simulations are executed until statistically stationary conditions are attained for both the velocity and scalar fields, after which various statistics of the instantaneous velocity and scalar fields are computed. This includes the calculations of the mean concentration, the concentration variance, the concentration co-spectrum and coherency spectrum, the concentration probability density function (PDF) and exceedance distribution function (EDF) and the higher-order concentration moments. The total computing time spent on solving the flow and scalar fields and on collecting the statistics is over 160,000 and 50,000 CPU hours for open-channel and homogeneous isotropic turbulent flows, respectively.

6.1.3 Single Plume Dispersion Characteristics

As one of the objectives of this research, the results for a single plume release are analyzed. It is found that for a plume released from a ground-level point source into an open-channel flow, the plume is in the turbulent diffusive regime of its development at all downwind locations. This is because for a ground-level source the width of the instantaneous plume is larger than the size of the most energetic turbulent eddies and the dispersion of the plume in this regime of development resembles the Brownian movements of diffusing particles.

In contrast to the ground-level single source release case, a plume released from an elevated point source, is in the turbulent convective regime at downwind locations close to the source. This is because at far vertical locations from the solid wall, the size of the most energetic eddies of the flow are initially larger than that of the instantaneous plume. However, at far downwind locations from the source, the size of the instantaneous plume reaches to that of the most energetic turbulent eddies and the development of the instantaneous plume transitions into the turbulent diffusive regime. Recalling that in the turbulent diffusive regime, the internal concentration fluctuations (in-plume mixing processes) provide the major contribution to the scalar fluctuations. However, in the turbulent convective regime, the bulk meandering of the instantaneous plume provides the primary contribution to scalar fluctuations.

For the release of material from a line source into homogeneous isotropic turbulence flow, it is seen that the plume is in the turbulent convective regime over the downwind fetches available in DNS data. The turbulent diffusive regime would have been observed for this case, if the simulations were performed either over a much larger isotropic box or with a much smaller source size.

In the following paragraph, some of the most interesting single plume dispersion characteristics are summarized. These characteristics are common in both turbulent flows. This indicates that the single plume dispersion characteristics only depend on the plume development regime, rather than on the type of the turbulent flow (turbulent open-channel flow or homogeneous isotropic turbulence flow).

It is found that in the turbulent convective regime, the concentration variance profiles are single peaked, because the strong meandering motion in this regime obliteration the off-centerline peaks in the concentration variance profiles. However, in the turbulent diffusive regime, where the meandering motions are small, the concentration variance profiles show the off-centerline peaks. The peaks locations coincide with the locations of the maximum mean concentration gradient. Furthermore, the strong meandering motions in the turbulent convective regime cause the concentration PDF along the plume centerline to exhibit an exponential-like form with a prominent peak at zero concentration. As the meandering reduces and the plume enters into the turbulent diffusive regime, the profile of the concentration PDF along the plume centerline approaches a Gaussian-like form.

6.1.4 Dual Plume Dispersion and Mixing

In the following, the major conclusions of the dual plume dispersion and mixing, which are common in both turbulent open-channel flow and homogeneous isotropic turbulent flow, are summarized.

In order to determine the nonlinear relationship between the variance of concentration fluctuations of the total plume and those produced by each of the two plumes, the covariance of the two concentration fields is studied in both physical and spectral spaces. The results show that at the source height, the streamwise evolution of the cross correlation between the fluctuating components of the two concentration fields can be classified into four stages.

In the first stage $\rho^{[1|1]} = 0$, because there is little or no interaction between the two plumes. The downwind location corresponding to this stage increases as source separation distance increases. In the second stage, which is also known as destructive interference stage, $\rho^{[1|1]} < 0$. During this stage, the instantaneous concentrations from the two sources are anti-correlated (viz., 'out of phase') in the following sense: while the concentration from one plume decreases as it meanders off the receptor location, that from the other plume increases as it meanders onto the receptor location. The downwind location corresponding to the absolute minimum in $\rho^{[1|1]}$ increases as the source separation d increases. This is simply because the larger the source separation, the greater the downwind fetch at which the pair of plumes start to overlap and interact with each other. In the third stage, which is also known as constructive interference stage, $\rho^{[1|1]} \geq 0$. In this stage, the instantaneous plumes from the two sources overlap to a greater and greater extent as the downwind distance increases. As a result, the two plumes tend to meander together over the receptor location midway between the two sources. This results in a positive correlation, which increases in the downwind direction owing to the increasing internal mixing within the region where the pair of plumes have overlapped. As the source separation distance decreases, the interaction between the two instantaneous plumes occurs closer to the two sources (viz., at a smaller downwind fetch), causing $\rho^{[1|1]}$ to increase faster for smaller d. In the fourth stage $\rho^{[1|1]} \to 1$ and the two plumes appear to be completely mixed. In this stage, the total plume behaves as if it is emitted from a single source. Cases with a smaller source separation tend to reach this complete mixing state earlier than the cases with a larger source separation.

The characteristics of these four stages of plume mixing are further confirmed through an analysis of the pre-multiplied co-spectra and coherency spectra. From the coherency spectrum, it is observed that there exists a range of ‘leading scales’ in which the mixing of two plumes is the fastest and the coherency spectrum can quickly approach its asymptotic value of unity. It is shown that for a plume in the turbulent convective regime (meander dominant regime), the size of the leading scales are typically large, due to the fact that the meandering motion is a large scale phenomena. However, for a plume in the turbulent diffusive regime (internal fluctuations dominant regime), the size of the leading scales are relatively small which is due to the fact that the internal turbulent mixing is a small scale phenomena.

A comparison between the concentration EDF for two sources and a single source shows that the probability of finding a high concentration level for the total plume is smaller than that for a single plume in both turbulent flow configurations. In order to quantify this reduction in the probability of high concentration level, a reduction factor (RF) is defined. It is found that there is a relationship between RF and the cross correlation coefficient ($\rho^{[1|1]}$). Scatterplots of RF against the cross correlation clearly revealed that a negative value for the cross correlation (destructive interference) is associated with large values for RF. However, for a positively valued cross correlation (constructive interference) RF assigns values that are comparable to unity.

The only major difference observed between the mixing of plumes in the turbulent open-channel flow and homogeneous isotropic turbulent flow is the rate of the mixing of plumes. The comparison between the concentration EDF in both flow configurations reveals that for a given regime of a plume development, the mixing rate of plumes in the turbulent open-channel flow is faster and more efficient than that in homogeneous isotropic turbulent flow. This is attributed to the presence of the mean shear stresses in the turbulent open-channel flow.

Finally, a remarkably robust feature for all test cases considered in this research is the observed collapse of the normalized third- and fourth-order concentration moments on the normalized second-order concentration moment. This observation implies that the higher-order concentration statistics for the total plume can be predicted either by the first- and second-order concentration statistics for the total plume or the first- and second-order concentration statistics for each single plumes and of the cross correlation. This observation further confirms that the clipped-gamma distribution provides very good predictions for the higher-order concentration moments of the total plume obtained from the dual source release.

6.2 Future Work

In this research, the dispersion and mixing of passive plumes released from a single and dual concentrated sources into turbulent open-channel and homogeneous isotropic turbulent flows are studied using DNS. To continue the current research, the following research topics are suggested.

- The current research is based on an Eulerian approach. The rich physics of dual plume interference can also be studied using a Lagrangian approach in the future. The results of the present research can be used to validate and improve the available theoretical models described in both Eulerian and Lagrangian approaches. Since the results of this research are obtained from DNS, they provide the most accurate benchmark to evaluate the predictive accuracy of different turbulence closure models for the scalar transport equation.

- A major limitation of this study is the simplicity of the domain geometry (open channel or isotropic box). In future studies, the dispersion and mixing of multiple plumes in a more complex domain can be considered. For instance, as a start, an array of wall-mounted obstacles can be used for emulating an idealized urban environment. Further extension of the research to the numerical simulation of pollutant plume interference in the atmospheric boundary layer represents a challenging and practical subject.

- In the present research, the dispersion and mixing of plumes are studied in the context of fully-developed turbulent flows (either in an open channel or in a cubic box). Further investigation of the problem may include use of developing turbulent flows, e.g. the release of material inside a developing turbulent jet. In this case, the scales of turbulent flows are developing as well as plume scales. The physics of dispersion and mixing become much more complicated due to the fact that in the interference of two jets, even the first-order moments of the flow field are not linearly superposable.

- In the current study, the Schmidt number is set to 1 in all test cases. The conclusions of this research is directly applicable to problems involving dispersion and mixing of passive thermal plumes and gases (e.g., CO_2, CH_4, SO_2, methanol, etc.) in the air, in which cases the Schmidt number is approximately equal to 1. However, in some engineering applications, the dispersion and mixing of heavy gases is of a primary interest. In view of this, it is important to examine the Schmidt number effects in future studies.
- The focus of this study is on passive plumes. It would be interesting to extend the current research findings to reactive and buoyant plumes, which have vast applications in combustion, chemical engineering, and natural environments.

Appendix A

Discretization Scheme used in Open-Channel Code

In this appendix, the discretization schemes for the momentum, continuity and advection-diffusion equations used in the open-channel code are summarized.

A.1 Continuity and Momentum Equations

For the open-channel flow code, the continuity and momentum transport equations are discretized using the fully conservative second-order finite difference scheme of Ham et al. (2002) with the fully implicit fractional step method of Choi and Moin (1994) for the solution of the continuity and momentum equations. The fully implicit fractional step method has the following steps

$$\frac{u_i^* - u_i^n}{\Delta t} + \frac{1}{4}\frac{\partial (u_j^n + u_j^*)(u_i^n + u_i^*)}{\partial x_j} = -\frac{1}{\rho}\frac{\partial p^n}{\partial x_i} + \frac{\nu}{2}\frac{\partial^2 (u_i^n + u_i^*)}{\partial x_j \partial x_j} \quad , \tag{A.1}$$

$$\frac{(u_i^{**} - u_i^*)}{\Delta t} = \frac{1}{2\rho}\frac{\partial p^n}{\partial x_i} \quad , \tag{A.2}$$

$$\frac{\partial^2 p^{n+1}}{\partial x_i \partial x_i} = \frac{2\rho}{\Delta t}\frac{\partial u_i^{**}}{\partial x_i} \quad , \tag{A.3}$$

$$\frac{(u_i^{n+1} - u_i^{**})}{\Delta t} = \frac{-1}{2\rho}\frac{\partial p^{n+1}}{\partial x_i} \quad . \tag{A.4}$$

Here, u_i^n and u_i^{n+1} are the velocities at the previous and current time steps, respectively, u_i^* and u_i^{**} are two intermediate velocity components, and p^n and p^{n+1} are the old and new pressures, respectively. In the first step, an intermediate velocity based on the pressure of the previous time step is calculated using an alternative directional implicit (ADI) solver; and then in the second step, it is further modified to a second intermediate velocity by removing half of the old pressure gradient. In the third step, the Poisson equation is solved using a multigrid solver to obtain the new pressure field. Finally, half of the new pressure gradient is used to update the velocity field.

Figure A.1(a) shows the schematic of a 3-D computational node and its neighbors for a Cartesian coordinate system. In this figure the computational node is represented by P (point), and the neighboring nodes are denoted by W (west), E (east), S (south), N (north), B (bottom) ans T (top). Lower case letters w, e, s, n, b and t are used for the faces of the computational in same directions. In order to demonstrate the spacing and indices of the computational cell more clearly, figure A.1(b) shows the computational nodes, cell, faces and their indices in a 2-D configuration. In the following, the discretization of the continuity and momentum equations in a compact and the expanded form which are respectively described by LePoudre (2003) and Saeedi (2014) will be presented.

A.1.1 Compact Form

The compact discretized form of the continuity and momentum equations can be written as

$$\frac{\delta_1 u_i}{\delta_1 x_i} = 0 \quad , \tag{A.5}$$

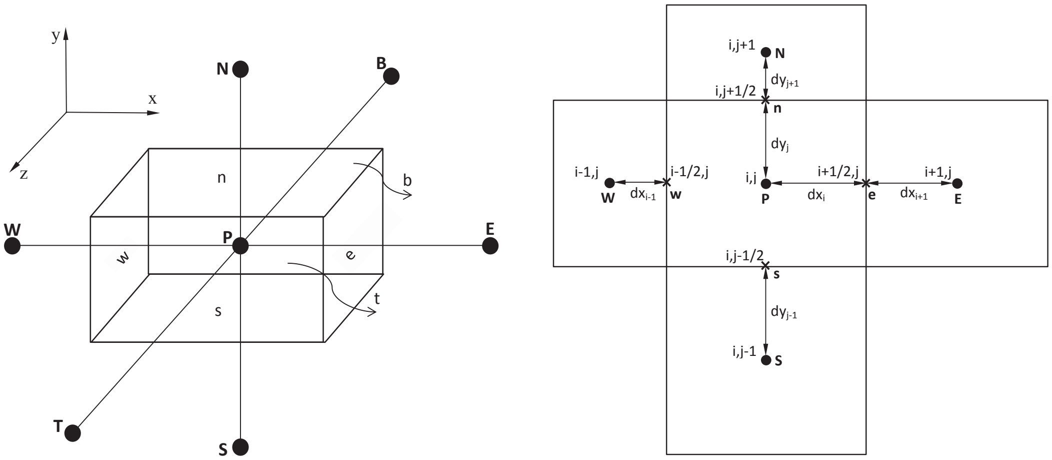

(a) 3-D configuration (b) 2-D configuration

Figure A.1: Schematic of a typical computational cell, its node, faces, indices and neighbors in 2-D and 3-D configurations for the base grid. Note that in a staggered grid arrangement, the grids for storing velocity components (u, v and w) are half-cell shifted in x, y and z directions, respectively.

$$\frac{\delta_1 u_i}{\delta_1 t} + \frac{\delta_1 \overline{\overline{u_j}^{1t}}^{1\check{x}_i} \overline{\overline{u_i}^{1t}}^{1x_j}}{\delta_1 x_j} = -\frac{1}{\rho}\frac{\delta_1 \overline{p}^{1t}}{\delta_1 x_i} + \nu \frac{\delta_1}{\delta_1 x_j}\left(\frac{\delta_1 \overline{u_i}^{1t}}{\delta_1 x_j}\right) \quad . \tag{A.6}$$

Note that the superscript x_i does not follow the summation convention. Here the one-delta (δ_1) is the second-order central-difference operator which is spatially defined in the x direction as

$$\left.\frac{\delta_1 \psi}{\delta_1 x}\right|_{i,j,k} = \frac{\psi_{i+\frac{1}{2},j,k} - \psi_{i-\frac{1}{2},j,k}}{x_{i+\frac{1}{2},j,k} - x_{i-\frac{1}{2},j,k}} \quad , \tag{A.7}$$

where ψ is a generic variable stored at cell faces, i, j, k represents the nodal location and $i+1/2$ and $i-1/2$ are the corresponding east and west faces, respectively. Similar definition can be presented for the one-delta (δ_1) operator in time. The simple average operator in the time $\overline{\psi}^{1t}$ represents a Crank-Nicolson temporal discretization. The simple averaging is defined as

$$\left.\overline{\psi}^{1x}\right|_{i,j,k,n} = \frac{\psi^n_{i+\frac{1}{2},j,k} + \psi^n_{i-\frac{1}{2},j,k}}{2} \quad , \tag{A.8}$$

in which superscript $1x$ represents one delta operator in the x direction. The volume averaging is defined as

$$\left.\overline{\psi}^{1\check{x}}\right|_{i,j,k,n} = \frac{(x_{i+\frac{1}{2}} - x_i)\psi^n_{i+\frac{1}{2},j,k} + (x_i - x_{i-\frac{1}{2}})\psi^n_{i-\frac{1}{2},j,k}}{x_{i+\frac{1}{2}} - x_{i-\frac{1}{2}}} \quad . \tag{A.9}$$

A.1.2 Expanded Form

In order to have a better understanding of the discretization of the governing equations, in the following the expanded version of equations A.5 and A.6 will be presented for the x-component (corresponding to $i = 1$ in equation A.6).

The Poisson equation (equation A.3), which also represent the continuity equation, is expanded to

$$\frac{\partial^2 p^{n+1}}{\partial x \partial x} + \frac{\partial^2 p^{n+1}}{\partial x \partial x} + \frac{\partial^2 p^{n+1}}{\partial x \partial x} = \frac{2\rho}{\Delta t}\left(\frac{\partial u^{**}}{\partial x} + \frac{\partial v^{**}}{\partial y} + \frac{\partial w^{**}}{\partial z}\right) \quad . \tag{A.10}$$

Applying the discretization for the first and second derivatives, a final algebraic equation of the following form will be obtained

$$A_p p_p^{n+1} = A_E p_E^{n+1} + A_W p_W^{n+1} + A_N p_N^{n+1} + A_S p_S^{n+1} + A_T p_T^{n+1} + A_B p_B^{n+1} + B_p \quad , \tag{A.11}$$

where the neighbor coefficients are

$$\begin{aligned}
A_E &= \frac{1}{(dx_i + dx_{i+1})(dx_i + dx_i)} \quad ,\\
A_W &= \frac{1}{(dx_{i-1} + dx_i)(dx_i + dx_i)} \quad ,\\
A_N &= \frac{1}{(dy_j + dy_{j+1})(dy_j + dy_j)} \quad ,\\
A_S &= \frac{1}{(dy_{j-1} + dy_j)(dy_j + dy_j)} \quad ,\\
A_T &= \frac{1}{(dz_k + dz_{k+1})(dz_k + dz_k)} \quad ,\\
A_B &= \frac{1}{(dz_{k-1} + dz_k)(dz_k + dz_k)} \quad ,
\end{aligned} \tag{A.12}$$

and the central coefficient is

$$\begin{aligned}A_P = &\frac{1}{(dx_i + dx_{i+1})(dx_i + dx_i)}\\&+\frac{1}{(dx_{i-1} + dx_i)(dx_i + dx_i)}\\&+\frac{1}{(dy_j + dy_{j+1})(dy_j + dy_j)}\\&+\frac{1}{(dy_{j-1} + dy_j)(dy_j + dy_j)}\\&+\frac{1}{(dz_k + dz_{k+1})(dz_k + dz_k)}\\&+\frac{1}{(dz_{k-1} + dz_k)(dz_k + dz_k)}\quad ,\end{aligned} \tag{A.13}$$

and the source term takes the following form

$$B_p = \frac{-2\rho}{\Delta t}\left[\frac{u^{**}_{i,j,k} - u^{**}_{i-1,j,k}}{(dx_i + dx_i)} + \frac{u^{**}_{i,j,k} - u^{**}_{i,j-1,k}}{(dy_j + dy_j)} + \frac{u^{**}_{i,j,k} - u^{**}_{i,j,k-1}}{(dz_k + dz_k)}\right] \quad . \tag{A.14}$$

For the momentum transport equation, the convective terms are discretized as

$$\frac{1}{4}\left[\frac{\partial(u^n + u^*)(u^n + u^*)}{\partial x}\right]_p = \frac{u_{fe}\dfrac{\dfrac{u^n_{i,j,k} + u^*_{i,j,k}}{2} + \dfrac{u^n_{i+1,j,k} + u^*_{i+1,j,k}}{2}}{2} - u_{fw}\dfrac{\dfrac{u^n_{i,j,k} + u^*_{i,j,k}}{2} + \dfrac{u^n_{i-1,j,k} + u^*_{i-1,j,k}}{2}}{2}}{dx_i + dx_{i+1}} \quad , \tag{A.15}$$

$$\frac{1}{4}\left[\frac{\partial(v^n + v^*)(u^n + u^*)}{\partial y}\right]_p = \frac{v_{fn}\dfrac{\dfrac{u^n_{i,j,k} + u^*_{i,j,k}}{2} + \dfrac{u^n_{i,j+1,k} + u^*_{i,j+1,k}}{2}}{2} - v_{fs}\dfrac{\dfrac{u^n_{i,j,k} + u^*_{i,j,k}}{2} + \dfrac{u^n_{i,j-1,k} + u^*_{i,j-1,k}}{2}}{2}}{dy_j + dy_j} \quad , \tag{A.16}$$

$$\frac{1}{4}\left[\frac{\partial(w^n+w^*)(u^n+u^*)}{\partial z}\right]_p = \frac{w_{ft}\dfrac{\dfrac{u^n_{i,j,k}+u^*_{i,j,k}}{2}+\dfrac{u^n_{i,j,k+1}+u^*_{i,j,k+1}}{2}}{2} - w_{fb}\dfrac{\dfrac{u^n_{i,j,k}+u^*_{i,j,k}}{2}+\dfrac{u^n_{i,j,k-1}+u^*_{i,j,k-1}}{2}}{2}}{dz_k+dz_k} , \tag{A.17}$$

in which

$$u_{fe} = \frac{dx_{i+1}\dfrac{u^n_{i+1,j,k}+u^*_{i+1,j,k}}{2} + dx_{i+1}\dfrac{u^n_{i,j,k}+u^*_{i,j,k}}{2}}{dx_{i+1}+dx_{i+1}} , \tag{A.18}$$

$$u_{fw} = \frac{dx_{i}\dfrac{u^n_{i,j,k}+u^*_{i,j,k}}{2} + dx_{i}\dfrac{u^n_{i-1,j,k}+u^*_{i-1,j,k}}{2}}{dx_{i}+dx_{i}} , \tag{A.19}$$

$$v_{fn} = \frac{dx_{i+1}\dfrac{v^n_{i+1,j+1,k}+v^*_{i+1,j+1,k}}{2} + dx_{i}\dfrac{v^n_{i,j+1,k}+v^*_{i,j+1,k}}{2}}{dx_{i}+dx_{i+1}} , \tag{A.20}$$

$$v_{fs} = \frac{dx_{i+1}\dfrac{v^n_{i+1,j-1,k}+v^*_{i+1,j-1,k}}{2} + dx_{i}\dfrac{v^n_{i,j-1,k}+v^*_{i,j-1,k}}{2}}{dx_{i}+dx_{i+1}} , \tag{A.21}$$

$$w_{ft} = \frac{dx_{i+1}\dfrac{w^n_{i+1,j,k+1}+w^*_{i+1,j,k+1}}{2} + dx_{i}\dfrac{w^n_{i,j,k+1}+w^*_{i,j,k+1}}{2}}{dx_{i}+dx_{i+1}} , \tag{A.22}$$

$$w_{fb} = \frac{dx_{i+1}\dfrac{w^n_{i+1,j,k-1}+w^*_{i+1,j,k-1}}{2} + dx_{i}\dfrac{w^n_{i,j,k-1}+w^*_{i,j,k-1}}{2}}{dx_{i}+dx_{i+1}} . \tag{A.23}$$

The discretization of diffusion terms will be

$$\frac{\nu}{2}\frac{\partial^2(u^n+u^*)}{\partial x\partial x} = \nu\frac{(\frac{du}{dx})_e-(\frac{du}{dx})_w}{dx_i+dx_{i+1}} , \tag{A.24}$$

$$\frac{\nu}{2}\frac{\partial^2(u^n+u^*)}{\partial y\partial y} = \nu\frac{(\frac{du}{dy})_n-(\frac{du}{dy})_s}{dy_j+dy_j} , \tag{A.25}$$

$$\frac{\nu}{2}\frac{\partial^2(u^n+u^*)}{\partial z\partial z}=\nu\frac{(\frac{du}{dz})_t-(\frac{du}{dz})_b}{dz_k+dz_k} \quad , \tag{A.26}$$

in which

$$\left(\frac{du}{dx}\right)_e=\frac{\frac{u^n_{i+1,j,k}+u^*_{i+1,j,k}}{2}-\frac{u^n_{i,j,k}+u^*_{i,j,k}}{2}}{dx_{i+1}+dx_{i+1}} \quad , \tag{A.27}$$

$$\left(\frac{du}{dx}\right)_w=\frac{\frac{u^n_{i,j,k}+u^*_{i,j,k}}{2}-\frac{u^n_{i-1,j,k}+u^*_{i-1,j,k}}{2}}{dx_i+dx_i} \quad , \tag{A.28}$$

$$\left(\frac{du}{dy}\right)_n=\frac{\frac{u^n_{i,j+1,k}+u^*_{i,j+1,k}}{2}-\frac{u^n_{i,j,k}+u^*_{i,j,k}}{2}}{dy_{j+1}+dy_j} \quad , \tag{A.29}$$

$$\left(\frac{du}{dy}\right)_s=\frac{\frac{u^n_{i,j,k}+u^*_{i,j,k}}{2}-\frac{u^n_{i,j-1,k}+u^*_{i,j-1,k}}{2}}{dy_j+dy_{j-1}} \quad , \tag{A.30}$$

$$\left(\frac{du}{dz}\right)_t=\frac{\frac{u^n_{i,j,k+1}+u^*_{i,j,k+1}}{2}-\frac{u^n_{i,j,k}+u^*_{i,j,k}}{2}}{dz_{k+1}+dz_k} \quad , \tag{A.31}$$

$$\left(\frac{du}{dz}\right)_b=\frac{\frac{u^n_{i,j,k}+u^*_{i,j,k}}{2}-\frac{u^n_{i,j,k-1}+u^*_{i,j,k-1}}{2}}{dz_k+dz_{k-1}} \quad , \tag{A.32}$$

and the source term is discretized as

$$-\frac{1}{\rho}\frac{\partial p^n}{\partial x}=-\frac{\frac{p^n_{i+1,j,k}+p^*_{i+1,j,k}}{2}-\frac{p^n_{i,j,k}+p^*_{i,j,k}}{2}}{dx_i+dx_{i+1}} \quad . \tag{A.33}$$

The final algebraic form of the u-momentum equation takes the following form

$$A_pu^*_p=A_Eu^*_E+A_Wu^*_W+A_Nu^*_N+A_Su^*_S+A_Tu^*_T+A_Bu^*_B+B_p \quad , \tag{A.34}$$

in which the neighbor coefficients are

$$
\begin{aligned}
A_E = {} & -\frac{dx_{i+1}\dfrac{u^n_{i+1,j,k}+u^*_{i+1,j,k}}{2} \quad + \quad dx_{i+1}\dfrac{u^n_{i,j,k}+u^*_{i,j,k}}{2}}{4(dx_i+dx_{i+1})(dx_{i+1}+dx_{i+1})} \\
& + \frac{\nu}{4dx_{i+1}(dx_i+dx_{i+1})} \quad ,
\end{aligned}
$$

$$
\begin{aligned}
A_W = {} & +\frac{dx_{i}\dfrac{u^n_{i,j,k}+u^*_{i,j,k}}{2} \quad + \quad dx_{i}\dfrac{u^n_{i-1,j,k}+u^*_{i-1,j,k}}{2}}{4(dx_i+dx_{i+1})(dx_{i}+dx_{i})} \\
& + \frac{\nu}{4dx_{i}(dx_i+dx_{i+1})} \quad ,
\end{aligned}
$$

$$
\begin{aligned}
A_N = {} & -\frac{dx_{i+1}\dfrac{v^n_{i+1,j+1,k}+v^*_{i+1,j+1,k}}{2} \quad + \quad dx_{i}\dfrac{v^n_{i,j+1,k}+v^*_{i,j+1,k}}{2}}{4(dy_j+dy_j)(dx_i+dx_{i+1})} \\
& + \frac{\nu}{4dy_j(dy_{j+1}+dy_j)} \quad ,
\end{aligned}
$$

$$
\begin{aligned}
A_S = {} & +\frac{dx_{i+1}\dfrac{v^n_{i+1,j-1,k}+v^*_{i+1,j-1,k}}{2} \quad + \quad dx_{i}\dfrac{v^n_{i,j-1,k}+v^*_{i,j-1,k}}{2}}{4(dy_j+dy_j)(dx_i+dx_{i+1})} \\
& + \frac{\nu}{4dy_j(dy_j+dy_{j-1})} \quad ,
\end{aligned}
$$

$$
\begin{aligned}
A_T = {} & -\frac{dx_{i+1}\dfrac{w^n_{i+1,j,k+1}+w^*_{i+1,j,k+1}}{2} \quad + dx_{i}\dfrac{w^n_{i,j,k+1}+w^*_{i,j,k+1}}{2}}{4(dz_k+dzk)(dx_i+dx_{i+1})} \\
& + \frac{\nu}{4dz_k(dz_{k+1}+dz_k)} \quad ,
\end{aligned}
$$

$$
\begin{aligned}
A_B = {} & +\frac{dx_{i+1}\dfrac{w^n_{i+1,j,k-1}+w^*_{i+1,j,k-1}}{2} \quad + \ dx_{i}\dfrac{u^n_{i,j,k-1}+u^*_{i,j,k-1}}{2}}{4(dz_k+dzk)(dx_i+dx_{i+1})} \\
& + \frac{\nu}{4dz_k(dz_k+dz_{k-1})} \quad ,
\end{aligned}
\tag{A.35}
$$

and the central coefficient is

$$\begin{aligned}
A_P = & \frac{1}{\Delta t} \\
& + \frac{dx_{i+1}\dfrac{u^n_{i+1,j,k}+u^*_{i+1,j,k}}{2} \quad + \quad dx_{i+1}\dfrac{u^n_{i,j,k}+u^*_{i,j,k}}{2}}{4(dx_i+dx_{i+1})(dx_{i+1}+dx_{i+1})} + \frac{\nu}{4dx_{i+1}(dx_i+dx_{i+1})} \\
& - \frac{dx_i\dfrac{u^n_{i,j,k}+u^*_{i,j,k}}{2} \quad + \quad dx_i\dfrac{u^n_{i-1,j,k}+u^*_{i-1,j,k}}{2}}{4(dx_i+dx_{i+1})(dx_i+dx_i)} + \frac{\nu}{4dx_i \quad (dx_i+dx_{i+1})} \\
& + \frac{dx_{i+1}\dfrac{v^n_{i+1,j+1,k}+v^*_{i+1,j+1,k}}{2} + dx_i\dfrac{v^n_{i,j+1,k}+v^*_{i,j+1,k}}{2}}{4(dy_j+dy_j)(dx_i+dx_{i+1})} + \frac{\nu}{4dy_j \quad (dy_{j+1}+dy_j)} \\
& - \frac{dx_{i+1}\dfrac{v^n_{i+1,j-1,k}+v^*_{i+1,j-1,k}}{2} + dx_i\dfrac{v^n_{i,j-1,k}+v^*_{i,j-1,k}}{2}}{4(dy_j+dy_j)(dx_i+dx_{i+1})} + \frac{\nu}{4dy_j \quad (dy_j+dy_{j-1})} \\
& + \frac{dx_{i+1}\dfrac{w^n_{i+1,j,k+1}+w^*_{i+1,j,k+1}}{2} + dx_i\dfrac{w^n_{i,j,k+1}+w^*_{i,j,k+1}}{2}}{4(dz_k+dzk)(dx_i+dx_{i+1})} + \frac{\nu}{4dz_k \quad (dz_{k+1}+dz_k)} \\
& - \frac{dx_{i+1}\dfrac{w^n_{i+1,j,k-1}+w^*_{i+1,j,k-1}}{2} + dx_i\dfrac{u^n_{i,j,k-1}+u^*_{i,j,k-1}}{2}}{4(dz_k+dzk)(dx_i+dx_{i+1})} + \frac{\nu}{4dz_k \quad (dz_k+dz_{k-1})} \quad ,
\end{aligned} \tag{A.36}$$

and the source term coefficient takes the following form

$$\begin{aligned}
B_p = & \frac{2u^n_P}{\Delta t} \\
& + A_E u^n_E + A_W u^n_W + A_N u^n_N + A_S u^n_S + A_T u^n_T + A_B u^n_B \\
& - \frac{\dfrac{p^n_{i+1,j,k}+p^*_{i+1,j,k}}{2} - \dfrac{p^n_{i,j,k}+p^*_{i,j,k}}{2}}{dx_i+dx_{i+1}} \quad .
\end{aligned} \tag{A.37}$$

A.1.3 Advection-Diffusion Equation

For the time advancement of the advection-diffusion equation, a Crank-Nicolson scheme was used. For the spatial discretization of the diffusion term, a central-differencing scheme was employed. Owing to the presence of high gradients in the concentration fields, it is critically important to use a proper numerical scheme for the discretization of the convective term in the advection-diffusion equation of the scalar. To this purpose, it is known that if a second-order central differencing or higher-order scheme is used for the discretization of the convective term, non-physical oscillations may occur in the solution for c which can result in unphysical negative concentrations. On the other hand, the use of an upwind scheme for the discretization of the convective term has the tendency to "smear out" the plume concentration field owing to the false diffusion inherent in this scheme. These problems have been identified and discussed previously by Brethouwer et al. (1999), Livescu et al. (2000), Vrieling and Nieuwstadt (2003), Xie et al. (2004) and Boppana et al. (2012). Based on the previous experience of these investigators, a total variation diminishing (TVD) scheme is used for the discretization of the convective term in the advection-diffusion equation. TVD schemes are monotonicity preserving and, as a consequence, do not result in non-physical oscillations for the concentration field. In particular, the instantaneous concentration obtained as a solution of the advection-diffusion equation is non-negative and never exceeds the source concentration (maximum realizable concentration). To this purpose and based on a comparative study of Waterson and Deconinck (2007), the Sharp and Monotonic Algorithm for Realistic Transport (SMART) developed by Gaskell and Lau (1988) is used to discretize the convective term in the advection-diffusion equation for the scalar. The SMART scheme has the following limiter function:

$$\varphi(r) = \max\left[0, \min\left(2r, \frac{3r+1}{4}, 4\right)\right] \quad , \tag{A.38}$$

where $\varphi(r)$ is the limiter function and r is the local ratio of the upstream gradient to downstream gradient in the concentration field. The SMART scheme is essentially third-order accurate, but it reduces to a first-order accurate upwind and a central-differencing scheme for $\varphi(r) = 0$ and 1, respectively.

In the following the discretization of the advection-diffusion equation in a compact and the expanded form will be presented.

A.1.4 Compact Form

The compact discretized form of the advection-diffusion equation can be written as

$$\frac{\delta_1 c}{\delta_1 t} + u_j \frac{\Delta_1 \bar{c}^{1t}}{\Delta_1 x_j} = \alpha \frac{\delta_1}{\delta_1 x_j}(\frac{\delta_1 \bar{c}^{1t}}{\delta_1 x_j}) \quad . \tag{A.39}$$

Equation A.39 is a linear algebraic equations which is solved by an ADI solver. Here the one-Delta (Δ_1) is the TVD operator which is spatially defined in the x direction for a flow in the positive x-direction as

$$\left.\frac{\Delta_1 \psi}{\Delta_1 x}\right|_{i,j,k} = \frac{\psi_{i,j,k} - \psi_{i-1,j,k} + \frac{1}{2}\varphi(r_e)(\psi_{i+1,j,k} - \psi_{i,j,k}) - \frac{1}{2}\varphi(r_w)(\psi_{i,j,k} - \psi_{i-1,j,k})}{x_{i+\frac{1}{2},j,k} - x_{i-\frac{1}{2},j,k}} \quad , \tag{A.40}$$

where $r_e = \frac{\psi_{i,j,k} - \psi_{i-1,j,k}}{\psi_{i+1,j,k} - \psi_{i,j,k}}$ and $r_w = \frac{\psi_{i-1,j,k} - \psi_{i-2,j,k}}{\psi_{i,j,k} - \psi_{i-1,j,k}}$.

A.1.5 Expanded Form

The convective terms are discretized as

$$\frac{\partial uc}{\partial x} = f_e \frac{c_e^n + c_e^{n+1}}{2} - f_w \frac{c_w^n + c_w^{n+1}}{2} \quad , \tag{A.41}$$

$$\frac{\partial vc}{\partial x} = f_n \frac{c_n^n + c_n^{n+1}}{2} - f_s \frac{c_s^n + c_s^{n+1}}{2} \quad , \tag{A.42}$$

$$\frac{\partial wc}{\partial x} = f_t \frac{c_t^n + c_t^{n+1}}{2} - f_b \frac{c_b^n + c_b^{n+1}}{2} \quad . \tag{A.43}$$

The convective fluxes are

$$f_e = \frac{\frac{u^n_{i,j,k} + u^{n+1}_{i,j,k}}{2}}{2dx_i} \quad , \quad f_w = \frac{\frac{u^n_{i-1,j,k} + u^{n+1}_{i-1,j,k}}{2}}{2dx_i} \quad , \tag{A.44}$$

$$f_n = \frac{\frac{v^n_{i,j,k} + v^{n+1}_{i,j,k}}{2}}{2dy_j} \quad , \quad f_s = \frac{\frac{v^n_{i,j-1,k} + v^{n+1}_{i,j-1,k}}{2}}{2dy_j} \quad , \tag{A.45}$$

$$f_t = \frac{\frac{w^n_{i,j,k} + w^{n+1}_{i,j,k}}{2}}{2dz_k} \quad , \quad f_b = \frac{\frac{w^n_{i,j,k-1} + w^{n+1}_{i,j,k-1}}{2}}{2dz_k} \quad , \tag{A.46}$$

Table A.1: Values of the α coefficients for different flow directions

$\alpha_e = 1$	for	$f_e > 0$	and	$\alpha_e = 0$	for	$f_e < 0$
$\alpha_w = 1$	for	$f_w > 0$	and	$\alpha_w = 0$	for	$f_w < 0$
$\alpha_n = 1$	for	$f_n > 0$	and	$\alpha_n = 0$	for	$f_n < 0$
$\alpha_s = 1$	for	$f_s > 0$	and	$\alpha_s = 0$	for	$f_s < 0$
$\alpha_t = 1$	for	$f_t > 0$	and	$\alpha_t = 0$	for	$f_t < 0$
$\alpha_b = 1$	for	$f_b > 0$	and	$\alpha_b = 0$	for	$f_b < 0$

and the value of the scalar field at cell faces are evaluated as

$$c_e = \alpha_e \left[c_P + \frac{1}{2}\varphi(r_e^+)(c_E - c_P) \right] \quad + \quad (1-\alpha_e) \left[c_E + \frac{1}{2}\varphi(r_e^-)(c_P - c_E) \right] \quad , \tag{A.47}$$

$$c_w = \alpha_w \left[c_W + \frac{1}{2}\varphi(r_w^+)(c_P - c_W) \right] + (1-\alpha_w) \left[c_P + \frac{1}{2}\varphi(r_w^-)(c_W - c_P) \right] \quad , \tag{A.48}$$

$$c_n = \alpha_n \left[c_P + \frac{1}{2}\varphi(r_n^+)(c_N - c_P) \right] + \ (1-\alpha_n) \left[c_N + \frac{1}{2}\varphi(r_n^-)(c_P - c_N) \right] \quad , \tag{A.49}$$

$$c_s = \alpha_s \left[c_S + \frac{1}{2}\varphi(r_s^+)(c_P - c_S) \right] \quad + \quad (1-\alpha_s) \left[c_P + \frac{1}{2}\varphi(r_s^-)(c_S - c_P) \right] \quad , \tag{A.50}$$

$$c_t = \alpha_t \left[c_P + \frac{1}{2}\varphi(r_t^+)(c_T - c_P) \right] \quad + \quad (1-\alpha_n) \left[c_T + \frac{1}{2}\varphi(r_t^-)(c_P - c_T) \right] \quad , \tag{A.51}$$

$$c_b = \alpha_b \left[c_B + \frac{1}{2}\varphi(r_b^+)(c_P - c_B) \right] \quad + \quad (1-\alpha_b) \left[c_P + \frac{1}{2}\varphi(r_b^-)(c_B - c_P) \right] \quad , \tag{A.52}$$

in which $\alpha_{e,w,\ldots}$ shows the flow directions, r is the ratio of the upstream to downstream gradients and φ is the flux limiter function. The values of α coefficients and the relationships for gradient ratios have been specified in tables A.1 and A.2, respectively.

The diffusion terms are discretized as

$$\alpha \frac{\partial^2 c}{\partial x \partial x} = \alpha \frac{\left(\frac{dc}{dx}\right)_e - \left(\frac{dc}{dx}\right)_w}{2dx_i} = \alpha \frac{\frac{\frac{c_E^n + c_E^{n+1}}{2} - \frac{c_P^n + c_P^{n+1}}{2}}{dx_i + dx_{i+1}} - \frac{\frac{c_P^n + c_P^{n+1}}{2} - \frac{c_W^n + c_w^{n+1}}{2}}{dx_i + dx_{i-1}}}{2dx_i} \quad , \tag{A.53}$$

Table A.2: The ratio of gradients for different flow directions and cell faces

x direction	$r_e^+ = \frac{c_P - c_W}{c_E - c_P}$	$r_e^- = \frac{c_{EE} - c_E}{c_E - c_P}$	$r_w^+ = \frac{c_W - c_{WW}}{c_P - c_W}$	$r_w^- = \frac{c_E - c_P}{c_P - c_W}$
y direction	$r_n^+ = \frac{c_P - c_S}{c_N - c_P}$	$r_n^- = \frac{c_{NN} - c_N}{c_N - c_P}$	$r_s^+ = \frac{c_S - c_{SS}}{c_P - c_S}$	$r_s^- = \frac{c_N - c_P}{c_P - c_S}$
z direction	$r_t^+ = \frac{c_P - c_B}{c_T - c_P}$	$r_t^- = \frac{c_{TT} - c_T}{c_T - c_P}$	$r_b^+ = \frac{c_B - c_{BB}}{c_P - c_B}$	$r_b^- = \frac{c_T - c_P}{c_P - c_B}$

$$\alpha \frac{\partial^2 c}{\partial y \partial y} = \alpha \frac{\left(\frac{dc}{dy}\right)_n - \left(\frac{dc}{dy}\right)_s}{2dy_j} = \alpha \frac{\frac{\frac{c_N^n + c_N^{n+1}}{2} - \frac{c_P^n + c_P^{n+1}}{2}}{dy_j + dy_{j+1}} - \frac{\frac{c_P^n + c_P^{n+1}}{2} - \frac{c_S^n + c_S^{n+1}}{2}}{dy_j + dy_{j-1}}}{2dy_j} \quad , \tag{A.54}$$

$$\alpha \frac{\partial^2 c}{\partial z \partial z} = \alpha \frac{\left(\frac{dc}{dz}\right)_t - \left(\frac{dc}{dz}\right)_b}{2dz_k} = \alpha \frac{\frac{\frac{c_T^n + c_T^{n+1}}{2} - \frac{c_P^n + c_P^{n+1}}{2}}{dz_k + dz_{k+1}} - \frac{\frac{c_P^n + c_P^{n+1}}{2} - \frac{c_B^n + c_B^{n+1}}{2}}{dz_k + dz_{k-1}}}{2dz_k} \quad . \tag{A.55}$$

Applying the above discretization to the scalar transport equation, the following algebraic equation will be obtained

$$A_p c_p^{n+1} = A_E c_E^{n+1} + A_W c_W^{n+1} + A_N c_N^{n+1} + A_S c_S^{n+1} + A_T c_T^{n+1} + A_B c_B^{n+1} + B_p \quad , \tag{A.56}$$

in which the neighbor coefficients are

$$\begin{aligned}
A_E &= max(-f_e, 0) + \frac{\alpha}{4dx_i(dx_i + dx_{i+1})} \quad , \\
A_W &= max(\ \ f_w, 0) + \frac{\alpha}{4dx_i(dx_{i-1} + dx_i)} \quad , \\
A_N &= max(-f_n, 0) + \frac{\alpha}{4dy_j(dy_j + dy_{j+1})} \quad , \\
A_S &= max(\ \ f_s, 0) + \frac{\alpha}{4dy_j(dy_{j-1} + dy_j)} \quad , \\
A_T &= max(-f_t, 0) + \frac{\alpha}{4dz_k(dz_k + dz_{k+1})} \quad , \\
A_B &= max(\ \ f_b, 0) + \frac{\alpha}{4dz_k(dz_{k-1} + dz_k)} \quad ,
\end{aligned} \tag{A.57}$$

and the central coefficient is

$$
\begin{aligned}
A_P = & \frac{1}{\Delta t} \\
& + A_E + A_W + A_N + A_S + A_T + A_B \\
& + (f_e - f_w) + (f_n - f_s) + (f_t - f_b) \quad ,
\end{aligned}
\tag{A.58}
$$

and the source term is

$$
\begin{aligned}
B_P = & (\frac{2}{\Delta t} - A_P) c_P^n \\
& + A_E c_E^n + A_W c_W^n + A_N c_N^n + A_S c_S^n + A_T c_T^n + A_B c_B^n \\
& + \frac{1}{2} f_e \left[(1-\alpha_e)\varphi(r_e^-) - \alpha_e \varphi(r_e^+) \right] \quad (c_E^n - c_P^n) \\
& + \frac{1}{2} f_w \left[\alpha_w \varphi(r_w^+) - (1-\alpha_w)\varphi(r_w^-) \right] (c_P^n - c_W^n) \\
& + \frac{1}{2} f_n \left[(1-\alpha_n)\varphi(r_n^-) - \alpha_n \varphi(r_n^+) \right] \ (c_N^n - c_P^n) \\
& + \frac{1}{2} f_s \left[\alpha_s \varphi(r_s^+) - (1-\alpha_s)\varphi(r_s^-) \right] \quad (c_P^n - c_S^n) \\
& + \frac{1}{2} f_t \left[(1-\alpha_t)\varphi(r_t^-) - \alpha_t \varphi(r_t^+) \right] \quad (c_T^n - c_P^n) \\
& + \frac{1}{2} f_b \left[\alpha_b \varphi(r_b^+) - (1-\alpha_b)\varphi(r_b^-) \right] \quad (c_P^n - c_B^n) \quad .
\end{aligned}
\tag{A.59}
$$

A.2 Grid Resolution

The number of grid nodes and the spatial resolution (based on wall units) used for performing DNS are summarized in table A.3. The grid is uniform in the streamwise and spanwise directions. However, in order to resolve the wall shear layer, the grid spacing is gently stretched in the wall-normal direction using a hyperbolic tangent function. As shown in the table, the minimum and maximum grid resolutions in the wall-normal direction are $\Delta y^+_{min} = 0.03$ and $\Delta y^+_{max} = 4.6$ for $Re_\tau = 180$, and $\Delta y^+_{min} = 0.03$ and $\Delta y^+_{max} = 2.4$ for $Re_\tau = 395$. In general, the grid resolutions which are used here for conducting DNS at the two Reynolds numbers are much finer than those used in the DNS studies of Handler et al. (1999) and Moser et al. (1999) at

Table A.3: Summary of grid resolutions. Nx, Ny and Nz represent the number of grid nodes in the x-, y-, and z-directions, respectively. Δy^+_{min} and Δy^+_{max} are the minimum and maximum grid resolutions in the wall-normal direction.

Re_τ	$Nx \times Ny \times Nz$	Δx^+	Δz^+	Δy^+_{min}	Δy^+_{max}
180	$256 \times 128 \times 192$	8.8	3.9	0.03	4.6
395	$512 \times 256 \times 384$	4.8	3.2	0.03	2.4

comparable Reynolds numbers. In their study, they used a spectral method which requires much coarser grids to resolve the turbulent scales as compared to the finite volume or finite difference methods used herein.

Appendix B

Discretization Scheme Used in Isotropic Turbulence Code

In this appendix, the discretization schemes for the momentum, continuity and advection-diffusion equations used in the homogeneous isotropic turbulence code are summarized.

B.1 Continuity and Momentum Equations

The algorithm for the homogeneous isotropic turbulent flow code is based on a pseudo-spectral method described by Orszag and Patterson (1972) and Eswaran and Pope (1988). In order to use the pseudo-spectral method, as described by Yang and Wang (2016) a variable $\psi(\boldsymbol{x}, t)$ in physical space needs to be expanded into discrete Fourier series

$$\breve{\psi}(\boldsymbol{k}, t) = \frac{1}{N^3} \sum_{l_1} \sum_{l_2} \sum_{l_3} e^{-\mathrm{i}\boldsymbol{k}\cdot\boldsymbol{x}} \psi(\boldsymbol{x}, t) \quad , \tag{B.1}$$

where the summation is over all grid points, $\mathrm{i} = \sqrt{-1}$ is the imaginary unit, variable $\breve{\psi}$ represents the spectral coefficients of ψ, and $\boldsymbol{k} = [k_1, k_2, k_3]^T = [m_1 k_0, m_2 k_0, m_3 k_0]^T$ is the wavenumber vector, with m_1, m_2 and m_3 all being integers between $-N/2$ and

$N/2-1$, inclusive. Here, $k_0 = 2\pi/L$ represents the lowest positive wavenumber. Inversely, the physical variable can be obtained as

$$\psi(\boldsymbol{x},t) = \sum_{\boldsymbol{m}_1}\sum_{\boldsymbol{m}_2}\sum_{\boldsymbol{m}_3} e^{\imath\boldsymbol{k}\cdot\boldsymbol{x}}\breve{\psi}(\boldsymbol{k},t) \quad , \tag{B.2}$$

where the summation is over all wavenumbers in spectral space. All the Fourier and inversed Fourier transforms are conducted using FFTW[1] library. The mean velocity for the solution of the continuity and momentum equations is fixed to zero, from which it follows that $\breve{u}_i(0,t) \equiv 0$. However, in order to generate a mean advection of the passive scalar, a constant mean velocity is superimposed on the velocity fluctuations obtained from the solution of the continuity and momentum equations. Then the superimposed velocity field is implemented for the solution of the advection-diffusion equation.

Once the velocity and pressure fields are expanded into Fourier series, equations 2.1 and 2.2 can be written in spectral space as

$$k_i\breve{u}_i = 0 \quad , \tag{B.3}$$

and

$$\frac{\partial \breve{u}_i}{\partial t} = \breve{G}_i - \frac{\imath k_i \breve{p}}{\rho} - \nu k^2 \breve{u}_i \quad , \tag{B.4}$$

respectively. Here, $k = (k_1^2+k_2^2+k_3^2)^{0.5}$ represents the norm of the wavenumber vector $\boldsymbol{k}$, and $\breve{G}_i$ represents the spectral coefficients of the combined convection and body force terms, i.e.

$$-u_j\frac{\partial u_i}{\partial x_j} + F_i = \sum_{\boldsymbol{m}_1}\sum_{\boldsymbol{m}_2}\sum_{\boldsymbol{m}_3} e^{\imath\boldsymbol{k}\cdot\boldsymbol{x}}\breve{G}_i(\boldsymbol{k},t) \quad . \tag{B.5}$$

The convection term in the above equation are computed in physical space and the 3/2 rule is applied to eliminate aliasing errors. Multiplying k_i on both sides of equation B.4 and absorbing equation B.3 into the resultant equation yields the formulation of the spectral coefficient of the pressure, viz.

$$\frac{\breve{p}}{\rho} = -\frac{\imath k_i \breve{G}_i}{k^2} \quad . \tag{B.6}$$

---

[1] www.fftw.org

On substituting equation B.6 into equation B.4, the momentum equation finally becomes

$$\frac{\partial \breve{u}_i}{\partial t} = P_{ij}\breve{G}_j - \nu k^2 \breve{u}_i \quad , \tag{B.7}$$

where

$$P_{ij} = \delta_{ij} - \frac{k_i k_j}{k^2} \quad , \tag{B.8}$$

is the projection tensor. Equation B.7 is then integrated to march the velocity field in time.

In order to sustain the turbulent kinetic energy (TKE) at a statistically stationary level, the artificial body force F_i proposed by Carati et al. (1995) is included in equation 2.2, which reads

$$\breve{\boldsymbol{F}}(\boldsymbol{k},t) = \frac{\epsilon_F}{N_F} \frac{\breve{\boldsymbol{u}}(\boldsymbol{k},t)}{\breve{\boldsymbol{u}}(\boldsymbol{k},t) \cdot \breve{\boldsymbol{u}}^\star(\boldsymbol{k},t)} \quad \text{for } k_0 \le k \le k_F \quad . \tag{B.9}$$

Here, $(\cdot)^\star$ represents the conjugate of a complex number. The forcing is enforced inside the shell for $k_0 \le k \le k_F$. As indicated by Eswaran and Pope (1988), because F_i is an artificial force, it introduces non-physical information into the flow field. In order to keep the $-5/3$ power-law of the energy spectrum unaltered by this artificial force, the shell radius k_F must be kept significantly smaller than the wavenumbers that characterize the inertial subrange. Following Eswaran and Pope (1988), we use $k_F/k_0 = \sqrt{2}$ in the present simulations. Integer N_F in equation B.9 represents the number of modes inside the shell, which is determined automatically by the shell radius k_F. Based on the specified shell radius $k_F/k_0 = \sqrt{2}$, the value of N_F is 18 in current simulations. The forcing intensity is controlled by the energy injection rate ϵ_F, which is set to a constant value 4.706×10^{-5} to balance the overall dissipation rate.

B.2 Advection-Diffusion Equation

The DNS data for the scalar field is obtained using the similar method described for the open-channel flow with a difference that the time advancement for both the velocity and scalar fields is achieved using the following explicit fourth-order Runge-Kutta scheme, i.e.,

$$c^{n+1} = c^n + \frac{1}{6}\left(K_1 + 2K_2 + 2K_3 + K_4\right) \quad . \tag{B.10}$$

Here, K_1, K_2, K_3 and K_4 are defined as

$$K_1 = \Delta t \left[-u_j \frac{\Delta_1 c^n}{\Delta_1 x_j} + \alpha \frac{\delta_1}{\delta_1 x_j}\left(\frac{\delta_1 c^n}{\delta_1 x_j}\right) \right] \quad , \tag{B.11}$$

$$K_2 = \Delta t \left[-u_j \frac{\Delta_1 (c^n + \frac{1}{2}K_1)}{\Delta_1 x_j} + \alpha \frac{\delta_1}{\delta_1 x_j}\left(\frac{\delta_1 (c^n + \frac{1}{2}K_1)}{\delta_1 x_j}\right) \right] \quad , \tag{B.12}$$

$$K_3 = \Delta t \left[-u_j \frac{\Delta_1 (c^n + \frac{1}{2}K_2)}{\Delta_1 x_j} + \alpha \frac{\delta_1}{\delta_1 x_j}\left(\frac{\delta_1 (c^n + \frac{1}{2}K_2)}{\delta_1 x_j}\right) \right] \quad , \tag{B.13}$$

$$K_4 = \Delta t \left[-u_j \frac{\Delta_1 (c^n + K_3)}{\Delta_1 x_j} + \alpha \frac{\delta_1}{\delta_1 x_j}\left(\frac{\delta_1 (c^n + K_3)}{\delta_1 x_j}\right) \right] \quad . \tag{B.14}$$

B.3 Grid Resolution

Table B.1 summarizes input parameters for controlling DNS and important output quantities. As indicated by Eswaran and Pope (1988), the flow is essentially controlled by three non-dimensional parameters: N, $Re_F = \epsilon_F^{1/3} k_0^{-4/3}/\nu$ and k_F/k_0. Here, Re_F is the forcing Reynolds number, whose value is 372.9. As shown in the table, the number of grid nodes used for the DNS is 256^3. The grid is uniform in all three coordinate directions. Based on this grid resolution, $k_{max}\eta = 1.42$ where $k_{max} = \sqrt{2}Nk_0/3$ is the maximum significant wavenumber resolved by the grid system, η is the Kolmogorov length scale defined as $\eta = (\nu^3/\epsilon)^{1/4}$ and ϵ is the mean rate of energy dissipation

Table B.1: Key input parameters and output quantities from DNS of homogeneous isotropic turbulence.

Input parameters					Output quantities				
N^3	$10^5\nu$	$10^5\epsilon_F$	Re_F	k_F/k_0	Re_λ	$k_0\eta$	$k_{\max}\eta$	l	$\hat{u}$
256^3	9.682	4.706	372.9	$\sqrt{2}$	150	1.178×10^{-2}	1.42	1.2	0.052

per unit mass. This value of $k_{max}\eta$ well satisfies the criterion suggested by Eswaran and Pope (1988) for the grid resolution required for conducting a 'good' DNS (viz., $k_{max}\eta > 1$).

As an output parameter of DNS, the Taylor-microscale Reynolds number is an important characteristic of homogeneous isotropic turbulence. It is defined as

$$Re_\lambda = \hat{u}\lambda/\nu \quad , \tag{B.15}$$

where $\lambda = (15\nu\hat{u}^2/\epsilon)^{1/2}$ represents the Taylor microscale and the fluctuating velocity scale $\hat{u}$ is determined from the TKE k_u as $\hat{u}^2 = 2k_u/3$. The Reynolds number calculated by DNS is $Re_\lambda = 150$. In table B.1, l is the integral length scale of the flow field defined as

$$l = \frac{\pi}{2\hat{u}^2} \int_0^{k_{max}} \frac{E(k)}{k} dk \quad . \tag{B.16}$$

Following the conventional approach for simulating homogeneous isotropic turbulence the units of the parameters shown in this table are not explicitly specified, with the implicit understanding that they are consistent by default in any chosen unit system.

Bibliography

Anand, M. S. and Pope, S. B. (1985). Diffusion behind a line source in grid turbulence. *Turbulent Shear Flows 4*. Eds. Bradbury, L. J. S., Durst, F., Launder, B. E., Schmidt, F. W. and Whitelaw J. H., pages 46–52.

Bernard, P. S. and Rovelstad, A. L. (1994). On the physical accuracy of scalar transport modelling in inhomogeneous turbulence. *Phys. Fluids*, 6:3093–3108.

Boppana, V. B. L., Xie, Z.-T., and Castro, I. P. (2012). Large-eddy simulation of dispersion from line sources in a turbulent channel flow. *Flow, Turb. Combust.*, 88:311–342.

Brethouwer, G., Boersma, B. J., Pourquie, M. B. J. M., and Nieuwstadt, F. T. M. (1999). Direct numerical simulation of turbulent mixing of a passive scalar in pipe flow. *Eur. J. Mech. B/Fluids*, 18:739–756.

Carati, D., Ghosal, S., and Moin, P. (1995). On the representation of backscatter in dynamic localization models. *Phys. Fluids*, 7:606–616.

Choi, H. and Moin, P. (1994). Effects of the computational time step on numerical solutions of turbulent flow. *J. Comp. Phys.*, 113:1–4.

Costa-Patry, E. and Mydlarski, L. (2008). Mixing of two thermal fields emitted from line sources in turbulent channel flow. *J. Fluid Mech.*, 609:349–375.

Davis, B. M., Jones, C. D., Manning, A. J., and Thomson, D. J. (2000). Some field experiments on the interaction of plumes from two sources. *Quart. J. R. Meteorol. Soc.*, 126:1343–1366.

Eswaran, V. and Pope, S. B. (1988). An examination of forcing in direct numerical simulations of turbulence. *Comput. Fluids*, 16:257–278.

Fackrell, J. E. and Robins, A. G. (1982). Concentration fluctuations and fluxes in plumes from point sources in a turbulent boundary layer. *J. Fluid Mech.*, 117:1–26.

Gaskell, P. H. and Lau, A. K. C. (1988). Curvature-compensated convective transport: SMART, a new boundedness-preserving transport algorithm. *Int. J. Numer. Meth. Fluids*, 8:617–641.

Gifford, F. (1959). Statistical properties of a fluctuating plume dispersion model. *Adv. Geophys.*, 6:117–137.

Ham, F. E., Lien, F. S., and Strong, A. B. (2002). A fully conservative second-order finite difference scheme for incompressible flow on nonuniform grids. *J. Comp. Phys.*, 177:117–133.

Handler, R., Saylor, J., Leighton, R., and Rovelstad, A. (1999). Transport of a passive scalar at a shear-free boundary in fully developed turbulent open channel flow. *Phys. Fluids*, 11:2607–2625.

Kaplan, H. and Dinar, N. (1989). The interference of two passive scalars in a homogeneous isotropic turbulent field. *J. Fluid Mech.*, 203:273–287.

Karnik, U. and Tavoularis, S. (1989). Measurements of heat diffusion from a continuous line sourcein a uniformly sheared turbulent flow. *J. Fluid Mech.*, 202:233–261.

Lavertu, R. A. and Mydlarski, L. (2005). Thermal dispersion from a line source in the shearless turbulence mixing layer. *J. Fluid Mech.*, 528:135–172.

LePoudre, P. P. (2003). Parallel unsteady Navier-Stokes solver using a fully conservative discretization and an implicit fractional step method. Master's thesis, University of Saskatchewan.

Livescu, D., Jaberi, F. A., and Madnia, C. K. (2000). Passive-scalar wake behind a line source in grid turbulence. *J. Fluid Mech.*, 416:117–149.

Lumley, J. L. (1962). The mathematical nature of the problem of relating Lagrangian and Eulerian statistical function in turbulence. *The Mechanics of Turbulence*, pages 17–26.

Moser, R. D., Kim, J., and Mansour, N. N. (1999). Direct numerical simulation of turbulent channel flow up to $Re_\tau = 590$. *Phys. Fluids*, 11:943–945.

Orlandi, P. and Leonardi, S. (2004). Passive scalar in a turbulent channel flow with wall velocity disturbances. *Flow, Turb. Combust.*, 72:181–197.

Orszag, S. A. and Patterson, G. S. J. (1972). Numerical simulation of three-dimensional homogeneous isotropic turbulence. *Phys. Rev. Let.*, 28:76–79.

Pasquill, F. and Smith, F. B. (1983). *Atmospheric Diffusion*. Ellis Horwood.

Saeedi, M. (2014). *Large-eddy simulation of turbulent flow and dispersion within modeled urban environments*. PhD thesis, University of Manitoba.

Sawford, B. L., Frost, C. C., and Allan, T. C. (1985). Atmospheric boundary-layer measurements of concentration statistics from isolated and multiple sources. *J. Boundary-Layer Meteorol.*, 31:249–268.

Sawford, B. L. and Hunt, J. C. R. (1986). Effects of turbulence structure, molecular diffusion and source size on scalar fluctuations in homogeneous turbulence. *J. Fluid Mech.*, 165:373–400.

Stapountzis, H. (1988). Covariance and mixing of temperature fluctuations from line sources in grid turbulence. *Transport Phenomena in Turbulent Flows.* Eds. M. Hirata and N. Kasagi, pages 419–431.

Stapountzis, H., Sawford, B. L., Hunt, J. C. R., and Britter, R. E. (1986). Structure of the temperature field downwind of a line source in grid turbulence. *J. Fluid Mech.*, 165:401–424.

Sykes, R. I. and Henn, D. S. (1992). Large eddy simulation of concentration fluctuations in a dispersing plume. *Atmos. Environ.*, 26(A):3127–3144.

Taylor, G. I. (1935). Statistical theory of turbulence, IV—Diffusion in a turbulent air stream. *Proc. R. Soc. Lond. A*, 151:465–478.

Tong, C. and Warhaft, Z. (1995). Passive scalar dispersion and mixing in a turbulent jet. *J. Fluid Mech.*, 292:1–38.

Townsend, A. A. (1954). The diffusion behind a line source in homogeneous turbulence. *Proc. R. Soc. Lond. A*, 224:487–512.

Uberoi, M. S. and Corrsin, S. (1953). Diffusion from a line source in isotropic turbulence. Technical Report TN 2710.

Vrieling, A. J. and Nieuwstadt, F. T. M. (2003). Turbulent dispersion from nearby point sources–interference of the concentration statistics. *Atmos. Environ.*, 37:4493–4506.

Wang, B.-C., Yee, E., and Lien, F.-S. (2009). Numerical study of dispersing pollutant clouds in a built-up environment. *Int. J. Heat Fluid Flow*, 30:3–19.

Warhaft, Z. (1981). The use of dual heat injection to infer scalar covariance decay in grid turbulence. *J. Fluid Mech.*, 104:93–109.

Warhaft, Z. (1984). The interference of thermal fields from line sources in grid turbulence. *J. Fluid Mech.*, 144:363–387.

Waterson, N. P. and Deconinck, H. (2007). Design principles for bounded higher-order convection schemes–a unified approach. *J. Comp. Phys.*, 224:182–207.

Xie, Z., Hayden, P., Voke, P. R., and Robins, A. G. (2004). Large-eddy simulation of dispersion: comparison between elevated and ground-level sources. *J. Turbul.*, 5:1–16.

Yang, Z. and Wang, B.-C. (2016). On attitude dynamics of the subgrid-scale stress tensor. Under consideration for publication in J. Fluid Mech.

Yee, E. (2009). Probability law of concentration in plumes dispersing in an urban area. *Environ. Fluid Mech.*, 9:389–407.

Yee, E. and Chan, R. (1997). A simple model for the probability density function of concentration fluctuations in atmospheric plumes. *Atmos. Environ.*, 31:991–1002.

Yee, E., Gailis, R. M., and Wilson, D. J. (2003). The interference of higher-order statistics of the concentration field produced by two point sources according to a generalized fluctuating plume model. *J. Boundary-Layer Meteorol.*, 106:297–348.

Yee, E., Kosteniuk, P. R., Chandler, G. M., Biltoft, C. A., and Bowers, J. F. (1993a). Recurrence statistics of concentration fluctuations in plumes within a near-neutral atmospheric surface layer. *J. Boundary-Layer Meteorol.*, 66:127–153.

Yee, E., Kosteniuk, P. R., Chandler, G. M., Biltoft, C. A., and Bowers, J. F. (1993b). Statistical characteristics of concentration fluctuations in dispersing plumes in the atmospheric surface layer. *J. Boundary-Layer Meteorol.*, 65:69–109.

Yee, E., Kosteniuk, P. R., Chandler, G. M., Biltoft, C. A., and Bowers, J. F. (1994a). Experimental measurements of concentration fluctuations and scales in a dispersing plume in the atmospheric surface layer obtained using a very fast-response concentration detector. *J. Appl. Meteorol.*, 33:996–1016.

Yee, E., Kosteniuk, P. R., Chandler, G. M., Biltoft, C. A., and Bowers, J. F. (1994b). Measurements of level-crossing statistics of concentration fluctuations in plumes dispersing in the atmospheric surface layer. *J. Boundary-Layer Meteorol.*, 73:53–90.

Yee, E. and Wilson, D. J. (2000). A comparison of the detailed structure in dispersing tracer plumes measured in grid-generated turbulence with a meandering plume model incorporating internal fluctuations. *J. Boundary-Layer Meteorol.*, 94:253–296.

Yeung, P. K. and Zhou, Y. (1997). Universality of the Kolmogorov constant in numerical simulations of turbulence. *Physical Review E*, 56:1746–1752.